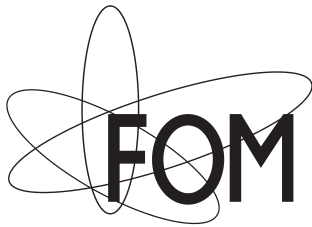


**Ellipsometric studies of
anisotropic nanoscaled media**

Ferrofluids in magnetic fields and anodized aluminium

Aurelian Cătălin Gâlcă



This work is part of the research program of the Stichting voor Fundamenteel Onderzoek der Materie (FOM), financially supported by the Nederlandse Organisatie voor Wetenschappelijk Onderzoek (NWO).

A. C. Gâlcă
Ellipsometric studies of anisotropic nanoscaled media:
Ferrofluids in magnetic fields and anodized aluminium
ISBN 90-365-2348-6

Published by the Solid State Physics group, University of Twente, Enschede,
The Netherlands

Printed by Wöhrmann Print Service, Zutphen, The Netherlands

ELLIPSOMETRIC STUDIES OF
ANISOTROPIC NANOSCALED MEDIA
FERROFLUIDS IN MAGNETIC FIELDS AND
ANODIZED ALUMINIUM

PROEFSCHRIFT

ter verkrijging van
de graad van doctor aan de Universiteit Twente,
op gezag van de rector magnificus,
prof. dr. W.H.M. Zijm,
volgens besluit van het College van Promoties
in het openbaar te verdedigen
op woensdag 12 juli 2006 om 13.15 uur

door

Aurelian Cătălin Gâlcă
geboren op 26 november 1977
te Buzău, Roemenië

Dit proefschrift is goedgekeurd door de promotor:
prof. dr. ir. Bene Poelsema

en door de assistent-promotor:
dr. E. Stefan Kooij

Contents

1	Introduction	9
1.1	Controlling nanoscale assemblies	10
1.2	Tunable interactions in nanocolloidal systems	11
1.2.1	Colloidal stability	11
	Brownian motion	11
	Van der Waals forces	12
	Electrostatic interaction	13
	Steric interaction	14
	Magnetic dipole-dipole interaction	15
	Overall interaction energy: Stability conditions	15
1.2.2	Ferrofluids in external magnetic fields	17
	Particle alignment in homogeneous magnetic field	17
	Deposition in homogeneous magnetic fields	18
	Magnetophoretic deposition	19
1.3	Outline of this thesis	20
	References	21
2	Anisotropy in nanoporous anodic aluminium oxide	25
2.1	Introduction	26
2.2	Experimental details	27
2.2.1	Sample fabrication	27
2.2.2	Anodization and chemical etching	28
2.2.3	Characterization techniques	28
	Scanning electron microscopy	28
	X-ray diffraction	29
	Rutherford backscattering	29
	Spectroscopic ellipsometry	29
2.3	Structural characterization	29
2.3.1	SEM	30

2.3.2	X-ray diffraction	31
2.3.3	RBS	32
2.4	Optical characterization	33
2.4.1	Anisotropic model for porous anodic aluminium oxide	35
2.4.2	Ellipsometry spectra of as-anodized aluminium oxide .	37
2.4.3	Tunable pore sizes by chemical etching	38
2.5	Conclusions	41
	Appendix: Alternative Bruggeman EMA	43
	References	45
3	Linear magneto-optical properties of ferrofluids	49
3.1	Introduction	50
3.2	Ferrofluid synthesis and characterization	51
3.2.1	Synthesis	51
3.2.2	Characterization	52
3.3	Linear magneto-optics	53
3.3.1	Transmission ellipsometry setup	53
3.3.2	Linear birefringence and dichroism	55
3.3.3	Experimental results	57
3.3.4	Comparison with other work and established theories	60
	Spectral dependence	60
	Field strength dependence	61
3.4	Conclusions	65
	References	66
4	Finite element analysis of magnetic configurations	69
4.1	Introduction	70
4.2	Finite element calculations	72
4.3	Homogeneous magnetic fields	73
4.4	Inhomogeneous magnetic fields	75
4.4.1	Single permanent magnet	75
4.4.2	Conically modified pole shape	76
4.4.3	Truncated cone modified pole shape	77
4.4.4	Single electromagnet pole	78
4.5	Conclusions	79
	References	80
5	In situ study of ferrofluids in external magnetic fields	83
5.1	Introduction	84
5.2	Visualization and kinetics of ferrofluid phase-separation . . .	85

5.2.1	Experimental observations	85
5.2.2	Quantitative analysis	87
5.3	In situ study of magnetophoretic deposition	89
5.3.1	Experimental configuration	89
5.3.2	Spectroscopic ellipsometry	90
5.3.3	Results	94
5.3.4	Discussion	97
5.4	Conclusions	101
	References	101
	Summary	103
	Samenvatting	107
	Acknowledgements	111
	Curriculum Vitae	113

Chapter 1

Introduction

Abstract

In this chapter an introduction is given to nanocolloid science. The interactions, which play a role in nanocolloidal suspensions, and the stabilization of the nanoparticles in solution are briefly described. Also the influence of external fields is discussed. The main focus will be on ferrofluids and the self-assembly of nanoscale systems. The chapter ends with an outline of the subjects considered in this thesis.

1.1 Controlling nanoscale assemblies

The processes of making structured materials can be divided in two sub-classes: ‘top-down’ and ‘bottom-up’ fabrication. The top-down approach involves molding or etching of bulk-like materials into smaller components. The bottom-up method is based on assembly of (nano)structured materials starting with small entities such as atoms, molecules or other nanoscale building blocks. The latter seems to be more favorable to obtain the smallest nanostructures. The big advantage is that ‘when we have some control of the arrangement of things on a small scale we will get an enormously greater range of possible properties that substances can have, and of different things that we can do’ [1]. The practical challenge originates from the fact that the bottom-up approach requires control over self-assembly processes at length scales in the low-nanometer range.

Fabrication of colloidal suspensions can, in general, also be achieved as described above. Top-down colloid manufacture is done by mechanical attrition. The resulting particles are generally nanocrystalline, consisting of small crystal domains, or they can even be completely amorphous. In all cases the dislocation density is high. Alternatively, bottom-up colloids, obtained by chemical precipitation or reduction methods are often single crystals or they have distinct nanocrystal domains with sharp boundaries of typically only one atom thick. Contrary to top-down colloids, whose properties are mainly determined by the size and density of dislocations, i.e. the degree of crystallinity, the bottom-up ones have the big advantage that the colloid size and resulting surface area dominate the physical properties of the (nano)particles.

Ferrofluids are two-phase systems, consisting of small ferro- or ferrimagnetic particles dispersed in a liquid. Because the size of the particles is in the nanometer range, i.e. between about 1 and 100nm, those suspensions are often referred to as magnetic nanocolloids. The research on magnetic colloids started halfway the twentieth century and has attracted considerable attention owing to their interesting physical properties and the wide variety of possible applications.

From a magnetic point of view, due to their small size, each particle is a single magnetic domain with a (permanent) magnetic moment proportional to its volume. The material of those particles can be pure metal, such as Co [2–9], Fe [9, 10] and Ni [9, 11], bimetals [9, 12–14], or oxides, such as ferrites [15–22]. Also, magnetic core shell particles [23–25] attract interest due to the independent tunability of magnetic properties and surface functionality. Since the colloidal systems exhibit behavior characteristic of a paramagnetic

material, but with considerably larger magnetic moments than conventional paramagnets, the ferrofluids are referred to as superparamagnetic.

Ferrofluids have been applied in the industry since early 1960 when they were used as a method to control fluids in space, more precisely as rotating shaft seals in satellites. Now, for the same purpose, the magnetic suspensions are in a wide variety of devices, such as centrifuges and computer hard disk drives. Also the voice coil gap of loudspeakers contains ferrofluids for damping undesired vibration and for cooling [26]. In magnetic data storage applications, the information density on tapes is inversely proportional to the size of magnetic domains. Current research is presently also focused on patterned self-assembly of magnetic nanoparticles on surfaces, with the ultimate aim to achieve beyond Tbit/inch² data storage densities [27].

In medicine and biology, ferrofluids are used in a number of different applications. Separation, immunoassay, magnetic resonance imaging (MRI), drug delivery, and hypothermia can be optimized by the use of magnetic particles [28]. Magnetite cationic liposomes (MCLs), one of the group of cationic magnetic particles, can be used as carriers to introduce DNA into cells since their positively charged surface associates with the negatively charged DNA. Also a direct binding procedure of several proteins and enzymes to fine magnetic particles was developed [29].

In the following sections we first summarize the interactions, which play a role in colloidal suspension in general and focus especially on magnetic systems. Subsequently, nanoscale assembly with and without using external magnetic fields will be described.

1.2 Tunable interactions in nanocolloidal systems

There are two main categories of interactions in nanocolloidal systems: (i) intrinsic interactions, which determine repulsive and attractive forces between suspended particles, and (ii) interactions induced by applied external fields. The interactions depend on particle composition, shape and size, as well as on properties of the solvent and stabilizing agents.

1.2.1 Colloidal stability

Brownian motion

The colloidal nanoparticles are subject to random displacement due to their bombardment by impulsive forces from the solvent molecules in which they

are dispersed. These stochastic forces are strongly dependent on the temperature. To illustrate the effect of the Brownian motion, the long-time limit of the mean-square displacement that a single colloidal sphere undergoes due to these stochastic forces, is expressed by:

$$\lim_{t \rightarrow \infty} \langle \Delta r^2(t) \rangle = \frac{2k_B T t}{\pi \eta d} \quad (1.1)$$

where $k_B T$ is the thermal energy, η is the solvent viscosity, and d is the particle diameter. Eq. 1.1 does not take into consideration many-body effects, but it is sufficient to see how this motion can be tuned. As expected, Brownian motion is most important for small particles. Also, temperature can, in principle, be used to control the contribution of Brownian motion to the colloidal stability. It is not straightforward to make an estimation of ‘Brownian energy’; for our system and calculations, presented later, we assume the energy of each particle, associated to Brownian motion, to amount to approximately $k_B T$.

Van der Waals forces

The long-range intermolecular forces give rise to long-range attractive forces between macroscopic objects, and account for colloid coagulation phenomena. The total Van der Waals interaction energy between two spherical particles (same material p) of diameters d_1 and d_2 with a surface-surface separation s , and suspended in a medium m , is given by [30]:

$$U_{\text{VdW}} = -\frac{A_{\text{pmp}}}{6} \left[\frac{d_1 d_2}{s(s+d_1+d_2)} + \frac{d_1 d_2}{2(s+d_1)(s+d_2)} + \ln \frac{s(s+d_1+d_2)}{(s+d_1)(s+d_2)} \right] \quad (1.2)$$

where A_{pmp} is the materials specific effective Hamaker constant, which is expressed by:

$$A_{\text{pmp}} = \left(\sqrt{A_{\text{pp}}} - \sqrt{A_{\text{mm}}} \right)^2 \quad (1.3)$$

The Hamaker constants A_{pp} and A_{mm} give the Van der Waals interaction between same media separated by vacuum. The specific values used in this chapter are $9.09k_B T$ for water [31], $13.13k_B T$ for cyclohexane [32] and $46.05k_B T$ for magnetite [32].

Van der Waals forces are dipolar interactions and depend (through the Hamaker constant) on the dielectric functions of the medium and the particles. Owing to the large dielectric contrast, they are much stronger for metallic particles than for dielectric particles. Especially in the latter case,

using solvents with specific dielectric functions enables tuning of the magnitude of the Van der Waals interactions [33].

Electrostatic interaction

When the particles are dispersed in an ionic solution, the dissociation of ionogenic groups on the particle surface and the differential adsorption of the ions into the surface region, will generate a particle surface potential, ψ_p . This potential, also often referred as the zeta potential, can be regarded as due to the charge that develops at the interface between a solid surface and its liquid medium. The net charge at the particle surface affects the ion distribution in the nearby region, increasing the concentration of counter ions close to the surface. Thus, an electrical double layer is formed in the region of the particle-liquid interface. The surface potential can be experimentally determined and, because it reflects the effective charge on the particles and is therefore related to the electrostatic repulsion between them, the zeta potential has proved to be extremely relevant to the practical study and control of colloidal stability and flocculation processes.

Of course, since all particles have the same charge, the particle-particle interaction is repulsive. A mathematical expression for this repulsive interaction is given by [34, 35]:

$$\frac{U_{el}}{k_B T} = B \frac{d_1 + d_2}{d_1 + d_2 + 2s} e^{-\kappa s} \quad (1.4)$$

In this equation, κ is the Debye screening parameter given by:

$$\kappa = q_e \sqrt{\frac{2cN_A}{k_B T \epsilon_w \epsilon_0}} \quad (1.5)$$

where q_e , c and $\epsilon_w \epsilon_0$ are the elementary charge, molar concentration and the dielectric permittivity of the electrolyte. Taking the dimensionless particle potential

$$\gamma_p = \frac{q_e \psi_p}{k_B T} \quad (1.6)$$

the coefficient B is given by:

$$B = \frac{2\pi \epsilon_w \epsilon_0 k_B T \tilde{d}}{q_e^2} \cdot \frac{\gamma_p + 2 \tanh(0.25\gamma_p) \Omega \kappa \tilde{d}}{1 + 0.5\Omega \kappa \tilde{d}} \quad (1.7)$$

where Ω and \tilde{d} are defined by:

$$\Omega = \frac{\gamma_p - 4 \tanh(0.25\gamma_p)}{2 \tanh^3(0.25\gamma_p)} \quad (1.8)$$

$$\tilde{d} = \frac{2d_1d_2}{d_1 + d_2} \quad (1.9)$$

As can be seen from the above equation and from the inset in fig. 1.1(b). the strength of electrostatic interaction is strongly dependent on the concentration of the electrolyte, having a larger value for low concentration when the surface potential is considered to be constant.

Steric interaction

The steric repulsion, also referred to as entropic repulsion, is due to the presence of long chain molecules adsorbed onto the particle surface. In some cases, also an inert inorganic shell, such as SiO_2 , is employed to provide hard-sphere steric repulsion. In the case of a molecular shell, each molecule has two distinctive parts: (i) a polar head, which is chemically associated (irreversible) with the particle surface, and (ii) an apolar tail, which allows suspension of the particles in an apolar solvent. For two particles, which approach each other closely, the adsorbed shell will tend to compress, giving rise to an effective repulsive interaction. Obviously, there will be no steric repulsion mechanism between particles which are separated by more than twice the length of the tails. The steric repulsion energy, in units of $k_B T$, is expressed by [36]:

$$\frac{U_s}{k_B T} = \frac{\pi d_1 d_2 \xi}{2} \left[2 - \frac{2s + d_1 + d_2}{2\sigma} \ln \frac{d_1 + d_2 + 4\sigma}{d_1 + d_2 + 2s} - \frac{s}{\sigma} \right] \cdot \Phi \left(1 - \frac{|s|}{2\sigma} \right) \quad (1.10)$$

where ξ is the surface concentration of adsorbed molecules, typically 10^{18} molecules/m², and σ is the individual length of these molecules, which is in fact the shell thickness of the particle; $\Phi(x)$ is the Heaviside step function, which takes into account that the steric energy is only effective for $s \leq 2\sigma$.

Commonly, in the case of magnetic systems, the molecules used to sterically protect the nanoparticles are fatty acids, i.e. long-chain carboxylic acids. For gold nanocrystals, alkanethiols are often used. The colloid science nomenclature is directly related with the number of containing carbon atoms, as for example C_4 (butyric acid), C_6 (caproic acid), C_8 (caprylic acid), C_{12} (lauric acid). This is due to the fact that the length of each

molecule, which yields the relative strength of the steric interaction, is proportional to the number of carbon atoms. However, if we consider stearic acid (C₁₈), approximately 2nm in length, the molecules lose their 'rigid rod' properties and the aforementioned energy has lower values. In our particularly case, we use oleic acid (also C₁₈) as surfactant, which has a double bond between the ninth and tenth carbon atoms, and therefore is more rigid than stearic acid.

Magnetic dipole-dipole interaction

When the nanoparticles are magnetic (ferro- or ferrimagnetic), each particle is regarded as a source of magnetic field, which induces a magnetic force on its neighbors. A spherical nanocolloidal particle has a magnetic dipole with a magnitude expressed by:

$$m = \frac{\pi M_{sb} \mu_0 d^3}{6} \quad (1.11)$$

where M_{sb} is the bulk saturation magnetization of the material and μ_0 is the vacuum magnetic permeability. The interaction between two such magnetic dipoles is dependent on the mutual orientation of their dipole moments. When the magnetic moments are aligned in a head-to-tail configuration there is an attractive interaction. The energy of the system of two dipole moments is minimal in this configuration and is given by:

$$U_m = -\frac{4m_1 m_2}{\pi \mu_0 (d_1 + d_2 + 2s)^3} \quad (1.12)$$

In the case of oppositely aligned dipole moments, in a head-to-head configuration, the repulsive interaction is largest.

For freely suspended magnetic particles, which have a permanent magnetic moment, in a colloidal solution, the system will minimize its energy. Indeed, chain formation has been observed in suspensions of sufficiently large colloidal particles [37]. In our evaluation of colloidal stability in the next section, eq. 1.12 will be used.

Overall interaction energy: Stability conditions

The overall particle-particle interaction energy, given by the algebraic sum of all aforementioned energies, determines whether the nanoparticle suspension is stable or not. We do not take into account the effect of gravity, which is negligible for the small particles considered in this work. To obtain a

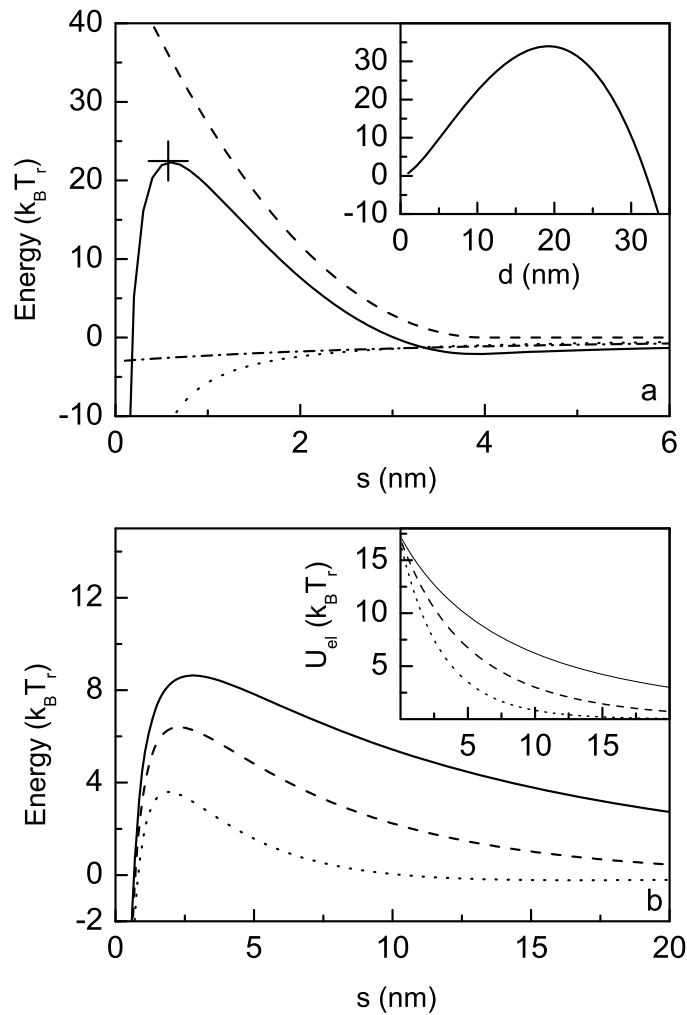


Figure 1.1: (a) Van der Waals energy (dotted line), steric energy (dashed line), magnetic energy (dash-dotted line) and overall energy (solid line) for two magnetite (Fe_3O_4) particles of 10nm diameter, having an oleic acid shell of 2nm thickness, versus surface-to-surface separation s ; in the inset the maximum of the overall energy (the cross in the case of 10nm diameter particles) as a function of particle diameter is shown. (b) The overall energy in the case of a repulsive electrostatic energy, which is shown in the inset, between the 10nm diameter solid particles, for 10^{-3}M (solid line), 10^{-2}M (dashed line), and $5 \times 10^{-2}\text{M}$ (dotted line) perchloric acid concentrations; for all cases a zeta potential of 40mV was used [38].

positive potential energy barrier, and to counteract attractive forces, the stabilization of a colloid can be achieved via (i) electrostatic stabilization by using ionic surfactants, (ii) steric stabilization using chemisorbed organic molecules or (iii) both stabilization processes using polyelectrolytes [36, 39].

In fig. 1.1(a) the overall energy and its constituting elements are plotted as a function of the surface-to-surface separation, for a colloidal system of two interacting magnetite particles (10nm diameter) dispersed in cyclohexane (C_6H_{12}) and stabilized with oleic acid. To obtain a stable suspension and prevent coagulation, the repulsive force due to steric interaction must compete effectively with the attractive Van der Waals and magnetic forces. In the calculations of fig. 1.1(a), a barrier of more than $20k_B T_r$ is present, which is sufficiently large to stabilize the suspension. Generally, the barrier should be high, i.e. a few times $k_B T_r$, in comparison with the Brownian energy of the suspended particles. In the inset in fig. 1.1(a) the height of the energy barrier is plotted as a function of particle diameter. Under the aforementioned conditions, it follows that particles with a diameter in the 5 – 30nm range are stable. For larger particles, the magnetic interaction becomes too large and coagulation leads to destabilization of the suspension.

In fig. 1.1(b) the separation distance dependent overall energy of an aqueous ferrofluid is presented. The plots are made for a 3 – 4 pH range, which seems to be optimal for 10nm magnetite colloids stabilized using perchloric acid ($HClO_4$) as electrolyte. Although the energy barrier is well above the thermal energy $k_B T_r$, the stability of the ferrofluid can be subject to conglomeration processes. Experimentally, the stability of these colloids can be tuned within limits. For example, low electrolyte concentrations give rise to spatially extended double layers and thus effectively stronger repulsive interactions. On the other hand, higher ionic strengths or a lower pH (larger H^+ concentration) lead to more effective screening of the surface charge, thus giving rise to effectively lower repulsive electrostatic forces.

1.2.2 Ferrofluids in external magnetic fields

Particle alignment in homogeneous magnetic field

The magnetite particles used for the experiments described in this thesis are well below the estimated single-domain size for spherical magnetite particles (typically 128nm [40]). Also due to the fact that our measurements are performed at room temperature 296K, much lower than the Curie temperature 520K [41], these particles can be regarded as having a single magnetic dipole moment.

When a magnetic particle is in a homogeneous magnetic field, its magnetic moment vector will attempt to align with the magnetic field. The torque exerted on a moment vector \mathbf{m} , in a uniform magnetic field \mathbf{H} is given by [41]:

$$\mathbf{T} = \mathbf{m} \times \mathbf{H} \quad (1.13)$$

The potential energy, i.e. the work done by the torque (eq. 1.13), is expressed by [41]:

$$U = -\mathbf{m} \cdot \mathbf{H} \quad (1.14)$$

However, the work due to the aforementioned torque is reversible, mainly due to the thermal energy. Under an applied external field, the magnetic moment oscillates around the magnetic field axis in the same way as the paramagnetic spins of a paramagnet. A primary issue is whether this oscillation is intrinsic (i.e. the magnetic moment is able to rotate within the particle frame) or extrinsic (i.e. the magnetic moment is pinned inside the particle and only the particle oscillates). For magnetization measurements on ferrofluids, i.e. Vibrating Sample Magnetometer measurements, the intrinsic or extrinsic mechanisms are both described by the same Langevin behavior.

Despite this similar behavior, the alignment of magnetic particles in a ferrofluid, which are generally prolate ellipsoidal particles, depends strongly on whether they are dominated by intrinsic or extrinsic oscillations. This is of importance for magneto-optical measurements such as those described in chapter 3. To exemplify this, we compare magnetite Fe_3O_4 , having a magneto-crystalline anisotropy constant $K_{\text{mc}} = 1.1 \times 10^4 \text{Jm}^{-3}$ and a bulk saturation magnetization $M_{sb} = 476 \text{kAm}^{-1}$, with cobalt ferrite CoFe_2O_4 , having $K_{\text{mc}} = 20 \times 10^4 \text{Jm}^{-3}$ and $M_{sb} = 400 \text{kAm}^{-1}$ [40]. When we consider prolate ellipsoidal particles with a long axis c and two short axes a , there will be a shape anisotropy, which can be evaluated from [40]:

$$K_s = \frac{1}{2} \mu_0 (N_a - N_c) M_{sb}^2 \quad (1.15)$$

where N_a and N_c are the demagnetization factors [42]. In the case of $c/a = 1.1$, i.e. $N_a - N_c = 0.47$ the shape anisotropy for magnetite is 6 times higher than the crystalline value $K_{\text{mc}} = 1.1 \times 10^4 \text{Jm}^{-3}$. For cobalt ferrite, on the other hand, we find that the shape anisotropy is 5 times smaller than the crystalline anisotropy constant $K_{\text{mc}} = 20 \times 10^4 \text{Jm}^{-3}$. This implies that for magnetite, the shape anisotropy will always lead to an alignment of the particles with the magnetic field. However, in cobalt ferrite, assuming a random orientation of the magneto-crystalline easy axis with respect to the

long axis of ellipsoid, shape anisotropy is negligible and there will not be an alignment of the particle shapes in an externally applied magnetic field.

Deposition in homogeneous magnetic fields

Considerable research effort has been devoted to obtain and characterize two- and three-dimensional nanoparticle lattices on various substrates [5, 44, 45]. The ultimate goal is to achieve control over the position of individual building blocks, which can be obtained by identifying the optimum particle size, composition and substrate and by tuning the interparticle interactions. The self-assembly process may also be altered by using external electric or magnetic fields.

There are a number of techniques to assemble nanocrystals from suspension into layered superstructures, which include: (i) drop casting combined with controlled drying [45, 46], (ii) Langmuir-Blodgett technique [47–49], (iii) layer-by-layer self-assembly [50–52], (iv) functionalised surfaces [53, 54] and (v) electric [54, 55] and/or magnetic [43, 44, 56] field-assisted depositions. In all cases, the particle-substrate interaction plays a major role. For example, with chemically functionalized substrates, the highly attractive interaction gives rise to a ‘hit-and-stick’-like deposition process. Due to the negligible surface mobility a random spatial distribution of the particles is obtained. Improved ordering can be obtained using a ‘saturated’ situation, such as in the case of the Langmuir-Blodgett technique. In the case of a repulsive particle-surface interaction, highly ordered assemblies can be obtained by using capillary forces in controlled drying experiments.

The influence of magnetic fields, applied during the controlled drying of magnetic nanoparticle suspensions, has been demonstrated by several groups [5, 43, 56]. As shown in fig. 1.2, moderate fields already give rise to island-like or elongated deposits, depending on the orientation of the magnetic field with respect to the surface normal [43].

Magnetophoretic deposition

In a homogeneous magnetic field, there is no translational force on nanocolloidal particles. An inhomogeneous magnetic field, on the other hand, gives rise to a magnetic field gradient, and this creates a net translational force on a suspended magnetic particle [41]:

$$F_x = m \frac{\delta H}{\delta x} \quad (1.16)$$

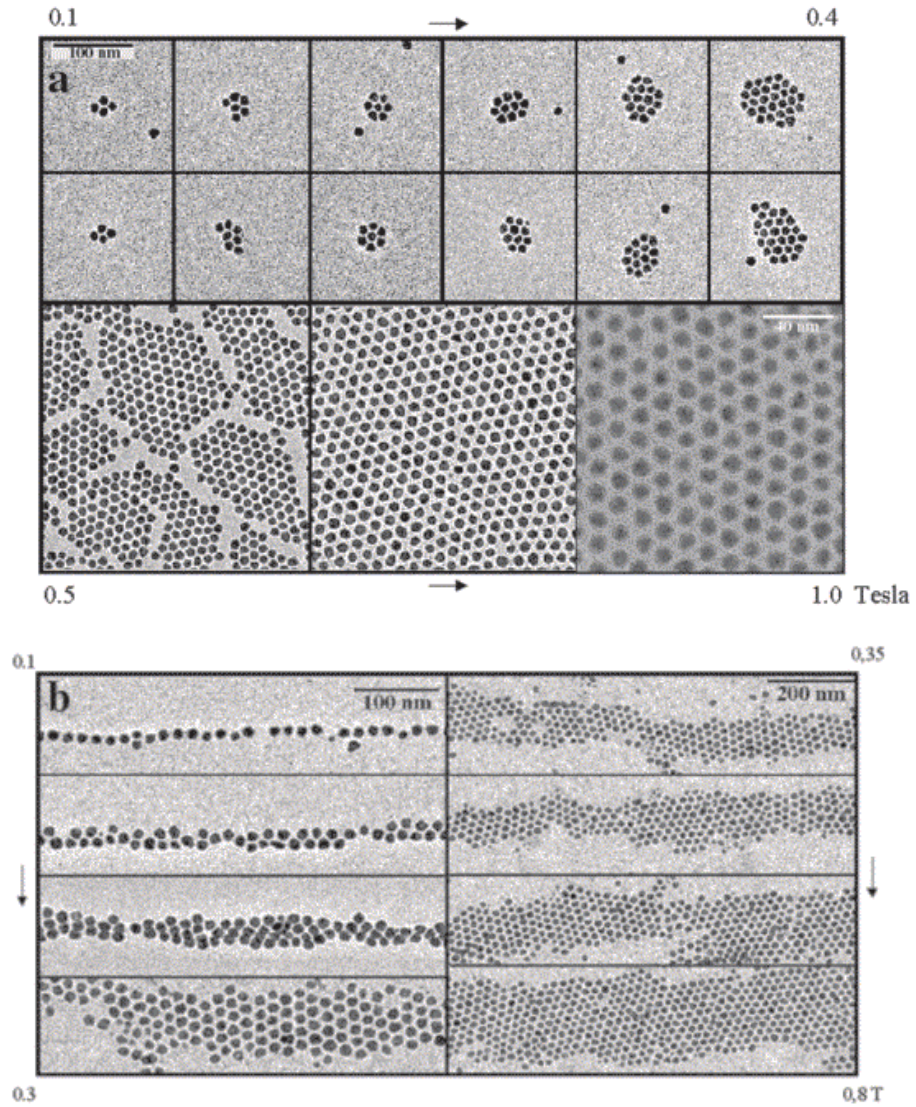


Figure 1.2: TEM images of ordered domains of 12nm diameter Co particles deposited on carbon-coated copper grids using magnetic fields between 0.1 and 1T parallel (a) and perpendicular (b) to the grid plane (from ref. [43]).

The magnetic energy given by this force on a nanocolloidal particle, i.e. the work done in moving a magnetized particle from a low magnetic field H_1 to a higher magnetic field value H_2 , is expressed by [36]:

$$W = \int_{H_2}^{H_1} \left(m \frac{\delta H}{\delta x} \right) \delta x \quad (1.17)$$

The influence of the magnetic field gradient on our magnetite particles will be described in chapter 4.

A few experiments and methods were developed using the concept of magnetophoresis and magnetophoretic deposition. A useful technique for observing the magnetic domains directly under a microscope is the powder-pattern method [41], and consist of placing colloidal ferromagnetic particles onto smooth surface of a ferromagnetic crystal and observing the image of domains outlined by magnetic particles. Lithographically fabricated micro-electromagnet arrays and a ring trap have been demonstrated. These devices produce magnetic field patterns, which enable microscopically precise control and manipulation of magnetic nanoparticles and biological entities [57]. Nanocomposites, manufactured by magnetophoretic deposition, have also been reported [58].

1.3 Outline of this thesis

The research, of which the results are described in this thesis, is primarily focused on studying the behavior of colloidal magnetic nanoparticles in the presence of external magnetic fields.

To enhance the magnetic moments of nanoparticles by employing their shape-anisotropy, we set out to synthesize elongated nanoparticles using porous anodic aluminium oxide templates, by electrochemical deposition inside the pores. The feasibility of this procedure has previously been demonstrated using pores with diameters in the 100nm range. In our case, we require rod-shaped particles with cross-section diameters in the low-nanometer range. Porous aluminium oxide prepared at sufficiently low voltages have pore diameters of typically 10nm. Due to this very small pore size, electrodeposition was unsuccessful. Nevertheless, we performed a detailed study of the optical properties of anodized porous aluminium oxide layers. We present an accurate model, which describes spectroscopic ellipsometry results in terms of physically relevant, geometrical parameters.

To enable accurate assessment of the optical characteristics of our nanocolloidal suspensions, we used spectroscopic ellipsometry in transmission

mode to study linear birefringence and dichroism of magnetite ferrofluids. This technique enables highly accurate, relatively fast characterization of linear magneto-optical phenomena. Simultaneously obtained field-dependent birefringence and dichroism are shown to be in line with previous results. Established models for magneto-optical properties are reviewed in relation to our ellipsometry results. Despite the qualitative agreement, these models fail to quantitatively describe our experimental results.

In chapter 4 we describe theoretical aspects of magnetophoretic deposition. A number of electromagnet configurations are investigated using finite element analysis. This technique enables calculation of the spatial distribution of the magnetic flux density in the vicinity of a permanent magnet or generated by an electromagnet. We show that by optimizing the magnet configuration, field gradients can be generated which are sufficiently large to enable magnetophoretic deposition of nanocolloidal particles onto a substrate.

Experimental results on magnetophoretic deposition are presented in chapter 5. Ex situ experiments show that indeed particles can be accumulated in the regions of high flux density. However, to circumvent drying effects on the morphology of assembled superstructures, we mainly focus on in situ experiments. In a stationary fluid cell, particles are accumulated when a well-defined field gradient is applied. However, a phase separation seems to take place, giving rise to a high-density cluster of magnetic particles.

References

- [1] <http://www.zyvex.com/nanotech/feynman.html> .
- [2] C. Petit, A. Taleb, and M. P. Pileni, *Adv. Mater.* **10**, 259 (1998).
- [3] Z. L. Wang, Z. Dai, and S. Sun, *Adv. Mater.* **12**, 1944 (2000).
- [4] V. F. Puentes, K. M. Krishnan, and P. Alivisatos, *Appl. Phys. Lett.* **78**, 2187 (2001).
- [5] M. Giersig and M. Hilgendorff, *Colloid. Surface. A* **202**, 207 (2002).
- [6] H. Bönnemann, W. Brijoux, R. Brinkmann, N. Matoussevitch, N. Waldöfner, N. Palina, and H. Modrow, *Inorg. Chim. Acta* **350**, 617 (2003).
- [7] C. Pathmamanoharan and A. P. Philipse, *J. Colloid Interf. Sci.* **205**, 340 (1998).
- [8] Y. W. Zhao, R. K. Zheng, X. X. Zhang, and J. Q. Xiao, *IEEE T. Magn.* **39**, 2764 (2003).

- [9] B. Chaudret, C. R. Phys. **6**, 117 (2005).
- [10] N. F. Kushchevskaya and N. A. Mishchuk, Colloid J. **65**, 44 (2003).
- [11] T. O. Ely, C. Amiens, B. Chaudret, E. Snoeck, M. Verelst, M. Respaud, and J. M. Broto, Chem. Mater. **11**, 526 (1999).
- [12] B. Stahl, N. S. Gajbhiye, G. Wilde, D. Kramer, J. Ellrich, M. Ghafari, H. Hahn, H. Gleiter, J. Weißmüller, R. Würschum, and P. Sclossmacher, Adv. Mater. **14**, 24 (2002).
- [13] E. Shevchenko, D. Talapin, A. Kornowski, F. Wiekhorst, J. Kötzler, M. Haase, A. Rogach, and H. Weller, Adv. Mater. **14**, 287 (2002).
- [14] H. Gu, B. Xu, J. Rao, R. K. Zheng, X. X. Zhang, K. K. Fung, and C. Y. C. Wong, J. Appl. Phys. **93**, 7589 (2003).
- [15] R. Massart, E. Dubois, V. Cabuil, and E. Hasmonay, J. Magn. Magn. Mater. **149**, 1 (1995).
- [16] A. T. Ngo and M. P. Pileni, Adv. Mater. **12**, 276 (2000).
- [17] T. Fried, G. Shemer, and G. Markovich, Adv. Mater. **13**, 1158 (2001).
- [18] S. Sun and H. Zeng, J. Am. Chem. Soc. **124**, 8204 (2002).
- [19] E. Hasmonay, J. Depeyrot, M. Sousa, F. Tourinho, J. Bacri, R. Perzynski, Y. Raikher, and I. Rosenman, J. Appl. Phys. **88**, 6628 (2000).
- [20] G. A. van Ewijk, G. J. Vroege, and A. P. Philipse, J. Magn. Magn. Mater. **201**, 31 (1999).
- [21] Y. I. Kim, D. Kim, and C. S. Lee, Physica B. **337**, 42 (2003).
- [22] D. Bica, L. Vékás, and M. Raşa, J. Magn. Magn. Mat. **252**, 10 (2002).
- [23] J. J. Schneider, Adv. Mater. **13**, 529 (2001).
- [24] M. Spasova, U. Wiedwald, M. Farle, T. Radetic, U. Dahmen, M. Hilgendorff, and M. Giersig, J. Magn. Magn. Mater. **272–276**, 1508 (2004).
- [25] Y. Kobayashi, M. Horie, M. Konno, B. Rodríguez-González, and L. M. Liz-Marzán, J. Phys. Chem. B **107**, 7420 (2003).
- [26] P. Berger, N. B. Adelman, K. J. Beckman, D. J. Campbell, A. B. Ellis, and G. C. Lisensky, J. Chem. Educ. **76**, 943 (1999).
- [27] T. Thomson, M. F. Toney, S. Raoux, S. L. Lee, S. Sun, C. B. Murray, and B. D. Terris, J. Appl. Phys. **96**, 1197 (2004).
- [28] M. Shinkai, J. Biosci. Bioeng. **94**, 606 (2002).
- [29] M. Koneracká, P. Kopcanský, M. Timko, C. Ramchand, A. de Sequeira, and M. Trevan, J. Mol. Catal. B-Enzym. **18**, 13 (2002).
- [30] R. J. Hunter, *Foundations of colloid science*, Oxford University Press Inc., New York, 2001.
- [31] J. Lyklema, *Fundamentals of interface and colloid science*, volume I, Academic Press Limited, London, 1991.
- [32] G. A. van Ewijk and A. P. Philipse, Langmuir **17**, 7204 (2001).
- [33] A. van Blaaderen, J. Peetermans, G. Maret, and J. K. G. Dhont, J.

- Chem. Phys. **96**, 4591 (1992).
- [34] E. S. Kooij, E. A. M. Brouwer, H. Wormeester, and B. Poelsema, *Langmuir* **18**, 7677 (2002).
- [35] J. E. Sader, *J. Colloid Interf. Sci.* **188**, 508 (1997).
- [36] R. E. Rosensweig, *Ferrohydrodynamics*, Dover Publications, INC., New York, 1997.
- [37] K. Butter, P. H. Bomans, P. M. Frederik, G. J. Vroege, and A. P. Philipse, *J. Phys.-Condens. Mat.* **15**, S1451 (2003).
- [38] Z. X. Sun, F. W. Su, W. Forsling, and P. O. Samskog, *J. Colloid Interf. Sci.* **197**, 151 (1998).
- [39] T. F. Tadros, *Adv. Colloid Interf.* **46**, 1 (1993).
- [40] K. J. Klabunde, *Nanoscale materials in chemistry*, John Wiley and Sons, Inc., New York, 2001.
- [41] S. Chikazumi, *Physics of ferromagnetism*, Oxford University Press, New York, 1997.
- [42] L. Sun, Y. Hao, C. L. Chien, and P. C. Searson, *IBM J. Res. Dev.* **49**, 79 (2005).
- [43] M. Hilgendorff, B. Tesche, and M. Giersig, *Aust. J. Chem.* **54**, 497 (2001).
- [44] M. P. Pileni, *C. R. Chim.* **6**, 965 (2003).
- [45] F. X. Redl, K. S. Cho, C. B. Murray, and S. O'Brien, *Nature* **423**, 968 (2003).
- [46] C. B. Murray, C. R. Kagan, and M. G. Bawendi, *Annu. Rev. Mater. Sci.* **30**, 545 (2000).
- [47] F. H. Reincke, *Assembly of charged gold nanocrystals at electrodes and liquid/liquid interfaces*, PhD thesis, Utrecht University, Utrecht, The Netherlands, 2004.
- [48] S. A. Iakovenko, A. S. Trifonov, M. Giersig, A. Mamedov, D. K. Nagesha, V. V. Hanin, E. C. Soldatov, and N. A. Kotov, *Adv. Mat.* **11**, 388 (1999).
- [49] S. Lefebure, C. Ménager, V. Cabuil, M. Assenheimer, F. Gallet, and C. Flament, *J. Phys. Chem. B* **102**, 2733 (1998).
- [50] A. Kumar, A. B. Mandale, and M. Sastry, *Langmuir* **16**, 9299 (2000).
- [51] A. Kumar, P. Mukherjee, A. Guha, S. D. Adyantaya, A. B. Mandale, R. Kumar, and M. Sastry, *Langmuir* **16**, 9775 (2000).
- [52] A. Mamedov, J. Ostrander, F. Aliev, and N. A. Kotov, *Langmuir* **16**, 3941 (2000).
- [53] E. S. Kooij, E. A. M. Brouwer, H. Wormeester, and B. Poelsema, *Encycl. Nanosci. Technol.* , 1515 (2004).
- [54] E. A. M. Brouwer, *Electric field assisted adsorption of nanocolloidal*

- gold particles: Characterisation and deposition kinetics*, PhD thesis, University of Twente, Enschede, The Netherlands, 2005.
- [55] M. Giersig and P. Mulvaney, *Langmuir* **9**, 3408 (1993).
- [56] Y. Lalatonne, J. Richardi, and M. P. Pileni, *Nat. Mater.* **3**, 121 (2004).
- [57] C. S. Lee, H. Lee, and R. M. Westervelt, *Appl. Phys. Lett.* **79**, 3308 (2001).
- [58] J. L. Katz, Y. Xing, and R. C. Cammarata, *J. Mater. Res.* **14**, 4457 (1999).

Chapter 2

Anisotropy in nanoporous anodic aluminium oxide: Structural and optical characterization

Abstract

Spectroscopic ellipsometry and electron microscopy (SEM) experiments are used to characterize porous aluminium oxide obtained by anodization of thin aluminium films. Rutherford backscattering and x-ray diffraction experiments provide information on the composition and the structure of the samples. Anodization of aluminium on thin film samples with a well-defined geometry is reproducible and results in a porous aluminium oxide network with randomly distributed, but perfectly aligned cylindrical pores perpendicular to the substrate. Ellipsometry spectra are analyzed using an anisotropic optical model, partly based on the original work by Bruggeman. We show that the model adequately describes the optical response of the anodized film in terms of three physically relevant parameters: the film thickness, the cylinder fraction and the nanoporosity of the aluminium oxide matrix. Values of the first two quantities are in perfect agreement with SEM results. The validity of our optical model was verified by widening of the pores through chemical etching in phosphoric acid. While the cylinder fraction increases significantly with etch time and etchant concentration, the nanoporosity remains almost unchanged. Additionally, based on a simple model considering a linear etch rate, the concentration dependence of the etch rate was determined.

2.1 Introduction

Porous aluminium oxide has stimulated considerable interest as a nanostructural template, primarily due to the self-organized formation of extremely well-aligned cylindrical pores [1–15]. One of the fascinating aspects is the tunability of the interpore distance and pore diameter by simple variation of the anodization parameters [1, 2, 4, 6, 9, 11, 13], such as voltage and electrolyte solution composition. Apart from the application of aluminium oxide films as filtration membranes, they are frequently used to fabricate nanowires with large aspect ratios [13, 15–20]. Many different materials, such as metals, both magnetic [14, 15, 21, 22] and non-magnetic [19, 23–26], semiconductors [19, 27–29], nanotubes [30–32] and even heterostructures [33], have been grown in the porous membranes using primarily electrodeposition, but for example also using a pressure injection technique [26]. Furthermore, porous aluminium oxide membranes have also been used as photonic crystals [7], as humidity sensors [34, 35], or as cathodes for organic light emitting diodes [36].

To control and optimize the formation of the aluminium oxide structure as well as the deposition of material within this porous matrix, truly in situ characterization techniques will be required, which do not interfere with the actual deposition procedure. Optical reflection techniques [37] provide a non-destructive method to quantitatively monitor the anodization procedure and the growth of the nanowires. A major advantage of these techniques is their full compatibility with electrochemical or vacuum environments.

Several studies of porous aluminium oxide structures, obtained under different anodization conditions, using spectroscopic ellipsometry have been published [38–41]. These investigations were performed on aluminium oxide films, formed by anodizing bulk aluminium samples. Different models have been proposed, which take into account the porosity of the film itself, but also include the barrier layer structure between the oxide matrix and the bulk substrate. In these models, the number of parameters is often large and unambiguous optical characterization of the films in terms of actual physical quantities is not straightforward.

To avoid the aforementioned problems related to the barrier layer, and also to enable an accurate determination of the film thickness, a thin film sample geometry may be employed [10, 42, 43]. The aluminium layer has a well-defined thickness, while after anodization it can be determined by ex situ techniques such as electron microscopy. Moreover, full anodization of the aluminium layer allows a smaller number of model parameters, since no bulk aluminium remains and the aforementioned barrier layer is absent.

Obviously, this increases the accuracy of any optical model.

In this chapter we present spectroscopic ellipsometry experiments on aluminium films with a well-defined thickness, grown on a silicon substrate. To ensure electrical conduction during the anodization procedure, a platinum layer is deposited between the aluminium and silicon using a titanium adhesion layer. We show that scanning electron microscopy (SEM) enables accurate *ex situ* characterization of the film thickness and the pore structure after anodization. Furthermore, Rutherford backscattering (RBS) experiments provide information on film thicknesses, which are too thin to distinguish with (cross-section) SEM. The ellipsometry spectra are analyzed in terms of an optical model, which takes into account the anisotropy of the porous structure arising from the randomly distributed, aligned pores within the oxide. Based on the original work by Bruggeman [44] and Wien [45], expressions are given for the parallel and perpendicular components of the dielectric functions, in terms of the cylinder fraction and the nanoporosity of the aluminium oxide matrix. Similar birefringence of a system of air cylinders in a silicon matrix have been described previously [46]. The resulting fit parameters are quantitatively compared with the sample structure determined from electron microscopy images. Furthermore, chemical etching in phosphoric acid solutions enables controlled widening of the pores [23], and therewith provides a means to test the accuracy of our model. Moreover, we show that ellipsometry results on a large number of samples, etched with different concentrations of acid solutions, allows identification of the etch process in terms of a rate constant and the order of the etch reaction.

2.2 Experimental details

2.2.1 Sample fabrication

Thin-film aluminium samples are grown by conventional sputtering on a silicon wafer (Philips Research Laboratories, Eindhoven). A 75nm platinum layer is deposited on a 10nm titanium adhesion layer. The aluminium layer grown on top of this structure is approximately $1\mu\text{m}$ thick. Scanning electron microscopy (SEM) indicates that the actual thickness amounts to $920\pm 5\text{nm}$, while the titanium and platinum layers have a combined thickness of $85\pm 5\text{nm}$. Wafers are cut into $14\text{mm}\times 14\text{mm}$ samples to enable mounting in the anodization cell, which is schematically shown in fig. 2.1. After mounting of the sample using an o-ring, a circular area with a diameter of 7.5mm is exposed to the electrolyte.

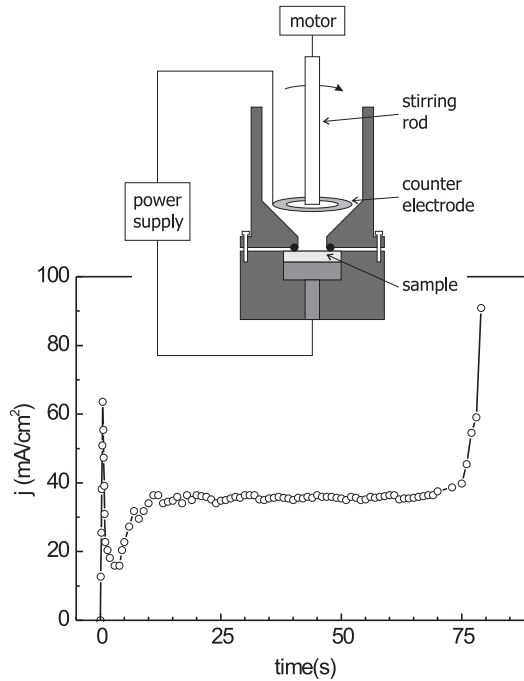


Figure 2.1: Schematic representation of the anodization cell used in the experiments. Also shown is the time evolution of the anodization current during the anodic oxidation at 15V in 15 vol.% H₂SO₄ aqueous solution.

2.2.2 Anodization and chemical etching

Porous aluminium oxide is obtained by anodization of the aluminium film in a two electrode configuration at a constant voltage of 15V in 15 vol.% H₂SO₄ at room temperature under continuous stirring. The procedure is identical to that described by Van der Zande and coworkers [23]. A typical anodization curve is shown in fig. 2.1. Upon applying a voltage, an initial current peak is observed due to double layer charging. After this peak, pore nucleation gives rise to an increase of the current to a plateau corresponding to a constant anodization of the aluminium. After approximately 70s the current increases rapidly, indicating that the pore fronts have reached the platinum substrate. For longer times, oxidation of water gives rise to oxygen gas evolution; bubble formation is indeed observed.

Controlled widening of the pores is achieved by chemical etching in the

same cell as described above. After anodization the cell is carefully rinsed and filled with an aqueous H_3PO_4 solution of known concentration. During this chemical etching procedure the solution is continuously stirred.

All chemicals (Merck) are used as received without any further purification. Aqueous solutions are prepared using water, which is purified in a Milli-Q system.

2.2.3 Characterization techniques

Scanning electron microscopy

SEM measurements are performed with a LEO Gemini 1550 FEG-SEM, equipped with a Field Emission Gun plus Thermo Noran Vantage EDX system and Thermo Noran MAXray Parallel Beam Spectrometer. The electron acceleration voltage can be set between 200V and 30kV; owing to the low voltage, deposition of a thin metal (gold) film is not required to ensure electrical conduction. The lateral resolution is approximately 2nm.

X-ray diffraction

High angle x-ray scattering measurements are performed using a single-crystal diffractometer (CAD4, Enraf Nonius) employing a rotating anode $\text{Cu-K}\alpha$ source ($\lambda_{\text{CuK}\alpha} = 1.542\text{\AA}$). The instrumental broadening for this system is estimated to be 0.2° . Scans are performed in the $\theta - 2\theta$ configuration.

Rutherford backscattering

RBS experiments are performed using a 2.5MV Van de Graaff accelerator (High Voltage Engineering Corp.). To enable alignment with the incident beam, samples are mounted on a three-axis goniometer system (Panmure) with an accuracy of 0.01° for all axes. A standard IBM geometry, with the incident and backscatter (detector) directions both in the tilt-plane, is used in a vacuum system (base pressure= 10^{-7} mbar), with a surface barrier detector (12 keV resolution) positioned at an angle of 165° with respect to the incident beam. All measurements are carried out with a collimated (1mm), monoenergetic beam of 2MeV $^4\text{He}^+$ -ions (30nA). All RBS spectra are normalized with respect to the integrated beam current.

Spectroscopic ellipsometry

For optical characterization, we use a home-built rotating polarizer spectroscopic ellipsometer equipped with a Xe lamp and a scanning monochroma-

tor. Measurements are performed in the visible and near-UV region of the spectrum at energies between 1.5 and 4.0eV at a fixed angle of incidence. The polar angle of incidence can be set between 45° and 70° ; unless stated otherwise, all measurements are done at 70° . Measurements in vacuum are performed using a BK7 glass cell as described in previous work [47]; a filament on the backside of the sample holder enables heating of the sample to 200°C . Both the incoming and outgoing light beams pass perpendicular to the cell windows, positioned at an angle of 67° . Bulk dielectric functions of all materials are taken from literature [48, 49].

2.3 Structural characterization

To enable accurate optical modeling, we characterized the structural properties of the aluminium films before and after anodization. Scanning electron microscopy provides information on the film thickness, pore distribution and the pore diameter. X-ray diffraction is used to characterize the crystallographic structure of the films, while the atomic composition, thickness and density of the layers are determined by RBS.

2.3.1 SEM

In figs. 2.2 and 2.3 typical SEM images are shown for the as-anodized samples (a) and after pore widening by chemical etching (b). The top view images in fig. 2.2 clearly exhibit an approximately random distribution of pores in the aluminium oxide film, both before and after chemical etching. Despite the apparent absence of azimuthal order, there is a preferred lateral distance separating adjacent pores. To quantify this we calculated the radial distribution function for the image in fig. 2.2(a); the result is shown in fig. 2.2(c). A similar result was obtained using the pore distribution in fig. 2.2(b). A single peak is observed at a distance of 33.5nm , corresponding to the average interpore distance. The absence of peaks at larger distances indicates that there is no long range organization of the pores in the film. Close examination of the autocorrelation image (insert in fig. 2.2(c)) indicates that there is some azimuthal order in a six-fold symmetry. The pore density as determined from the top view images amounts to $950\mu\text{m}^{-2}$. With the interpore distance as determined in fig. 2.2(c), we calculate that the pore density for a perfect hexagonal arrangement amounts to $1029\mu\text{m}^{-2}$. Due to a certain degree of azimuthal disorder, exhibited by the ring structure in the insert in fig. 2.2(c), the actual density obtained by counting the pores is slightly lower.

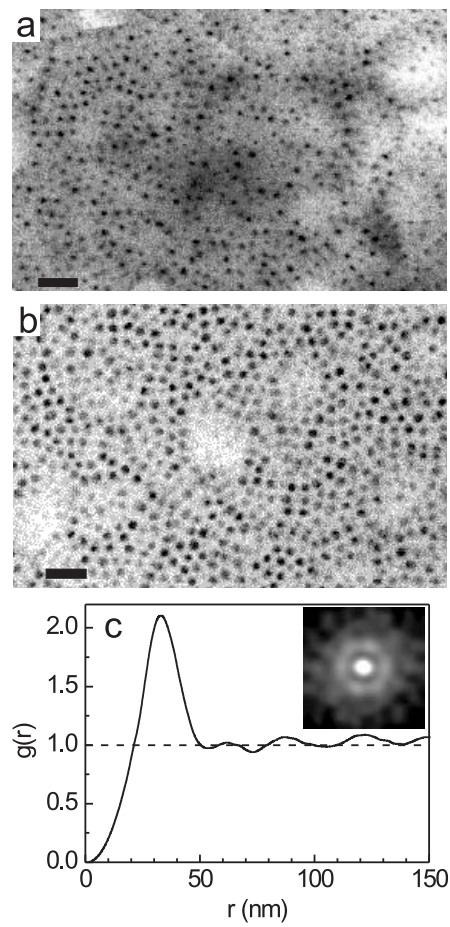


Figure 2.2: Top view SEM images of (a) as-anodized porous aluminium oxide and (b) after chemical etching for 10min in 3 vol.% H₃PO₄ aqueous solution. The bars correspond to 100nm. (c) Radial distribution function determined from (a) by radial integration of the autocorrelation image shown in the insert. The position of the maximum indicates an average pore separation distance of $d = 33.5$ nm.

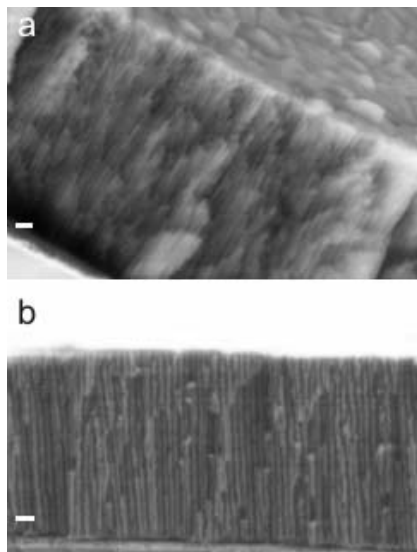


Figure 2.3: Cross section SEM images of (a) as-anodized porous aluminium oxide and (b) after chemical etching for 10min in 2 vol.% H_3PO_4 aqueous solution. The bars correspond to 100nm.

The cross section images in fig. 2.3 clearly show the parallel alignment of the pores, with the same average interpore distance as determined from the top view images in fig. 2.2. The pores initiate at the surface and extend all the way down to the platinum layer. For the as-anodized aluminium oxide, the average pore diameter of 11.5nm is the same throughout the film thickness. Upon chemical etching in phosphoric acid, a homogeneous widening of the pores along their entire length is observed (fig. 2.3(b)). Apparently, diffusion of the etchant or etch products is not rate limiting. The etch rate depends on the concentration of phosphoric acid. The average pore diameter in fig. 2.3(b) after immersion of the as-anodized sample in 2 vol.% H_3PO_4 solution for 10min amounts to 22.4nm. Upon prolonged etching and/or using a higher concentration of phosphoric acid the pores become wider. This will be discussed in more detail later on the basis of the optical results.

The thickness of the aluminium film, as determined from SEM images, prior to anodization amounts to approximately 920nm; upon anodization the film expands considerably to approximately 1400nm. The expansion by 50% is anomalously large. When we neglect the porosity and only consider

the film thickness and the densities of aluminium and aluminium oxide, a maximum thickness increase of 30% is to be expected. The aforementioned 50% expansion can only be explained by taking into account the 10% ‘meso’porosity due to the cylindrical pores and a 33% ‘nano’porosity of the aluminium oxide matrix. The latter porosity arises from defects and nanosized voids resulting from the considerable deformation upon anodization and the corresponding material transport away from the substrate [50]. More quantitatively, the charge involved in the anodization procedure (obtained by integration of the curve in fig. 2.1) can be related to the aluminium density. From this we conclude that practically all aluminium atoms are oxidized to trivalent Al^{3+} . Furthermore, by taking into account the sample thickness after anodization as well as the aforementioned porosities, we find that 28% of the Al^{3+} ions go into solution. This is in good agreement with results obtained by others [14].

2.3.2 X-ray diffraction

X-ray diffraction experiments show that the platinum and aluminium layers before anodization are polycrystalline. In fig. 2.4 a part of the x-ray spectra are shown for samples prior to and after anodization, respectively. The high-intensity Si(004) peak corresponding to the substrate is observed at 69.2° . We designate the first peak in fig. 2.4 at $2\theta = 33.3^\circ$ as the interface Si(002) peak, as the corresponding volume peak is ‘forbidden’; the intensity ratio of the Si(004) and Si(002) peaks is indeed more than 10^4 . The two peaks for the sample prior to anodization in fig. 2.4 at $2\theta = 38.6^\circ$ and $2\theta = 40.0^\circ$ correspond to Al(111) and Pt(111), respectively, and are in perfect agreement with the lattice constants $a = 4.05\text{\AA}$ and $a = 3.92\text{\AA}$ for fcc aluminium and platinum, respectively [51].

After anodization, the Pt(111) peak is still present, but the Al(111) peak is no longer observed. From the height of the Al(111) peak prior to anodization and the noise level in fig. 2.4, we estimate that more than 95% of the aluminium has been transformed into aluminium oxide. This is in good agreement with the conclusion in the previous section based on the quantitative analysis of the anodization experiment. Also, in contrast to the original sample, the x-ray spectrum of the anodized sample in fig. 2.4 exhibits a broad background intensity. We attribute this background signal to the amorphous aluminium oxide formed upon anodization. The amorphous nature of the aluminium oxide is also supported by the absence of any peaks related to crystalline alumina.

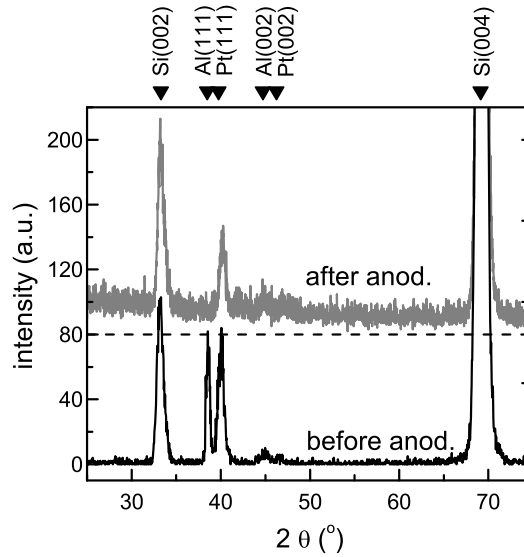


Figure 2.4: Out-of-plane x-ray diffraction spectra before and after anodization of the aluminium sample. The diffraction peak positions for silicon, aluminium and platinum are indicated. The spectrum after anodization is shifted upwards for clarity; the dash line corresponds to zero.

2.3.3 RBS

In fig. 2.5(a) a typical RBS spectrum is shown for our samples prior to anodization. The signal between 1.2MeV and 1.4MeV corresponds to the platinum layer. Integration of the peak area and taking into account the bulk density of platinum indicates a 75nm thick layer, which is in good agreement with the growth parameters and what is observed in SEM images. The plateau between 0.7MeV and 1.15MeV is due to the aluminium layer while the small peak at 0.85MeV represents the titanium contribution. Below 0.6eV the signal increase is due to the silicon substrate. The solid line represents a simulation using a stack of 920nm aluminium, 75nm platinum, 10nm titanium and a silicon substrate. The thickness of the aluminium layer is in perfect agreement with the results obtained from SEM measurements. The simulation takes into account a bulk density of aluminium, so this indicates that our samples have a dense, bulk-like aluminium layer. The energy positions of all signals are well reproduced but the experimental peaks appear to be broader than in the simulated spectrum; this is most obvious for the platinum signal, but a similar broadening is also discerned

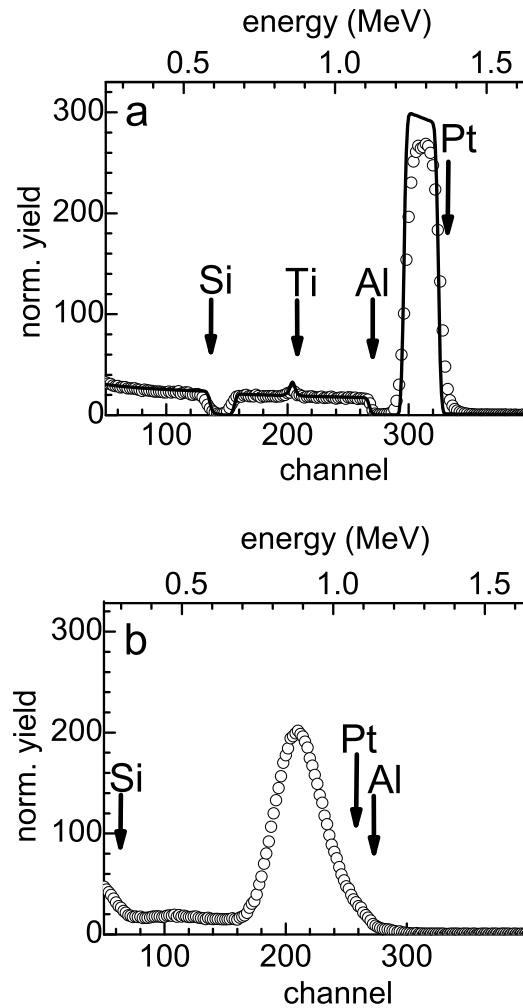


Figure 2.5: (a) Rutherford backscattering (RBS) spectrum (open circles) for an aluminium-platinum-titanium-silicon multilayered sample. The solid line represents a simulation using 920nm aluminium, 75nm platinum and 10nm titanium layers on a silicon substrate. The positions of the different contributions are also indicated. (b) RBS spectrum of the same sample after anodization.

for the titanium peak. Straggling in the top aluminium layer can not account entirely for the broadening; we ascribe this to a roughness of the sample. The energy resolution of the detector may also play a minor role.

Upon anodization, the RBS spectrum changes markedly as can be seen in fig. 2.5(b). The platinum peak between 0.7MeV and 1.1MeV is broadened considerably. Furthermore, the onset of the platinum signal is shifted to lower energies by approximately 0.3MeV. The latter can be accounted for by a larger energy loss in the aluminium oxide layer as compared to the initial aluminium film. Accordingly, the onset of the silicon signal also shows a shift from 0.6MeV to 0.3MeV. The backscattered signal from aluminium in the oxide layer does not suffer from any energy loss, and consequently the onset of this signal should be identical to that in fig. 2.5(a). Indeed, a small shoulder is observed near 1.1MeV on the flank of the platinum signal. Although the platinum peak is very broad, most probably due to large inhomogeneities in the mesoporous aluminium oxide layer, integration of the peak yields a platinum thickness of approximately 75nm, as expected. The aforementioned shift of the silicon and platinum signals should also be observed for the titanium contribution. However, the corresponding peak is not discerned at 0.85MeV.

2.4 Optical characterization

The optical properties of our samples prior to anodization and after formation of porous aluminium oxide are characterized using spectroscopic ellipsometry. Also, the effect of pore widening by chemical etching is investigated. In ellipsometry, the change of the polarization state of linearly polarized light is measured upon reflection at the surface. The complex reflection coefficient ρ is defined as

$$\rho = \frac{r_p}{r_s} = \tan(\Psi) \exp(i\Delta) \quad (2.1)$$

where r_p and r_s are the reflection coefficients for the parallel and perpendicular polarizations, respectively. For a single interface, r_p and r_s represent the Fresnel reflection coefficients. Historically, the quantity ρ is expressed in the two angles Ψ and Δ . Although the actual ellipsometry measurement is relatively simple, the analysis of the results is often complicated. An accurate model is required for the system under consideration, which enables simulation or fitting of the results.

The optical response of a multilayered structure with known dielectric

functions can be calculated using the Abelès matrix algorithm. Details of the original method are described by Azzam and Bashara [37]. Two types of matrices are used. One describes the transition from medium m to medium $m + 1$

$$\mathbf{I}_{m,m+1} = \frac{1}{t_{m,m+1}} \begin{pmatrix} 1 & r_{m,m+1} \\ r_{m,m+1} & 1 \end{pmatrix} \quad (2.2)$$

where $r_{m,m+1}$ and $t_{m,m+1}$ are the Fresnel reflection and transmission coefficients, respectively. Another matrix describes the light passage through the medium and involves the phase factors

$$\mathbf{L}_m = \begin{pmatrix} \exp(-i\Delta_m) & 1 \\ 1 & \exp(i\Delta_m) \end{pmatrix} \quad (2.3)$$

where $\Delta_m = (2\pi/\lambda)d_m n_m \cos(\theta_m)$ with λ being the wavelength of the light in vacuum (in nm), d_m the thickness of layer m (in nm), θ_m the angle of the light, and n_m the refractive index of medium m . The angles in the various media are related through Snell's law

$$n_m \sin(\theta_m) = n_{m+1} \sin(\theta_{m+1}) \quad (2.4)$$

For our system consisting of an anodic aluminium oxide layer ($m = 2$), a platinum layer ($m = 3$), and a titanium layer ($m = 4$) on a silicon substrate ($m = 5$), in contact with the ambient (air; $m = 1$), a matrix product is defined

$$\mathbf{A} = \mathbf{I}_{1,2}\mathbf{L}_2\mathbf{I}_{2,3}\mathbf{L}_3\mathbf{I}_{3,4}\mathbf{L}_4\mathbf{I}_{4,5} \quad (2.5)$$

and the overall reflection coefficient is calculated from $r = \mathbf{A}_{21}/\mathbf{A}_{11}$. For both the parallel and perpendicular polarizations, the reflection coefficients r_p and r_s can be obtained by inserting the appropriate Fresnel coefficients in eq. 2.2 and the ellipsometry quantity in eq. 2.1 can be calculated.

In the case of a film with uniaxial anisotropy, i.e. with an out-of-plane dielectric function ε_{ex} (the extraordinary direction) different from the dielectric function ε_{or} parallel to the substrate surface (the ordinary direction), the same matrix formalism can be used [37]. For our films, in which the cylindrical pores give rise to such uniaxial anisotropy, this is schematically represented in fig. 2.6. Obviously, the optical response for the s-polarization remains unchanged and is completely described by the ordinary dielectric function ε_{or} . For the p-polarization, a modified propagation angle is calculated by inserting the extraordinary refractive index $n_{\text{ex}} = \sqrt{\varepsilon_{\text{ex}}}$ into eq. 2.4. For the rest of the calculation, only the ordinary dielectric function ε_{or} of the anisotropic medium has to be taken into account.

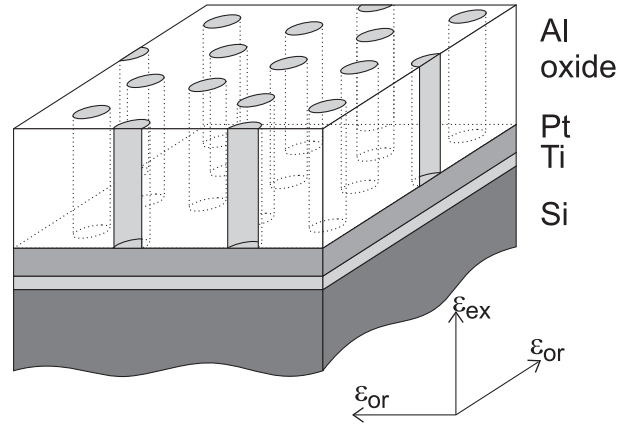


Figure 2.6: Schematic representation of the geometry and structural anisotropy of an anodized thin-film aluminium sample, indicating the ordinary and extraordinary directions referred to in the text.

2.4.1 Anisotropic model for porous anodic aluminium oxide

As is evident from the previous section, the samples have a clear structural anisotropy. However, several studies on the optical characterization of anodic aluminium oxide templates on bulk aluminium substrates did not take this into consideration [38–41]. Results obtained on films formed on bulk aluminium by anodization in sulfuric acid, indicated that there was no apparent optical anisotropy [38]; owing to the small dimension of the pores, conventional effective medium approximations yielded adequate results. Ellipsometry measurements on our samples, which consist of a thin layer of aluminium with a well-defined thickness, indicate that optical anisotropy needs to be taken into account. Especially upon widening of the pores by chemical etching, the anisotropy becomes more pronounced as the pore sizes increase substantially. To obtain adequate, unambiguous fit results, we incorporated the optical anisotropy in a model, which contains a minimum number of three parameters: (i) a film thickness, (ii) a mesoporosity, related to the cylindrical void fraction, and (iii) a nanoporosity of the aluminium oxide matrix [52].

As described in a previous section in relation to the thickness increase of the film during anodization, as observed by SEM, the aluminium oxide matrix is highly amorphous and presumably consists of a highly porous, non-crystalline structure containing voids with sizes in the low-nanometer range. In the work by Palibroda *et al.* [50] the structure of the oxide was reported

to be gel-like, containing a large number of “bubbles”, formed during the anodization procedure. The effective dielectric function of the nanoporous aluminium oxide, with porosity f_p , is modeled using the conventional effective medium approximation established by Bruggeman [44]

$$0 = f_p \frac{\varepsilon_a - \varepsilon_p}{\varepsilon_a + 2\varepsilon_p} + (1 - f_p) \frac{\varepsilon_{\text{Al}_2\text{O}_3} - \varepsilon_p}{\varepsilon_{\text{Al}_2\text{O}_3} + 2\varepsilon_p} \quad (2.6)$$

where ε_a and $\varepsilon_{\text{Al}_2\text{O}_3}$ represent the dielectric functions of the ambient (air in all cases presented here; $\varepsilon_a = 1$) and that of the aluminium oxide structure (we use the value of crystalline Al_2O_3 as taken from literature [49]), respectively.

The system with uniaxial anisotropy, formed by the almost perfectly aligned cylindrical pores in the oxide matrix, is described by two different dielectric functions ε_{ex} and ε_{or} (fig. 2.6). Although we are dealing with a much smaller length scale, this is similar to the description of optical anisotropy in macroporous silicon samples [46]. The extraordinary component describes the optical response of the film for electric field vectors parallel to the long axis of the cylindrical pores. Owing to the relatively small difference in dielectric constants of the oxide and the ambient, screening effects can be neglected. Therefore, we can interpret the system of parallel pores as a set of parallel plates and use the corresponding Wiener bound [45] to describe the dielectric function ε_{ex}

$$\varepsilon_{\text{ex}} = f_{\text{cyl}}\varepsilon_a + (1 - f_{\text{cyl}})\varepsilon_p \quad (2.7)$$

where f_{cyl} represents the overall pore volume fraction.

For the ordinary component we consider a cross-section through the film parallel to the interface. The effective dielectric function ε_{or} of this two-dimensional system of randomly distributed circles (with ε_a) in the oxide matrix (with ε_p) is modeled using an adaptation from the original work of Bruggeman [44]

$$1 - f_{\text{cyl}} = \frac{\varepsilon_a - \varepsilon_{\text{or}}}{\varepsilon_a - \varepsilon_p} \sqrt{\frac{\varepsilon_p}{\varepsilon_{\text{or}}}}. \quad (2.8)$$

Note that this is not the frequently employed conventional Bruggeman effective medium approximation (EMA). Also, the Maxwell-Garnett EMA can not be applied here as it is only valid for low cylinder fractions, $f_{\text{cyl}} < 10 - 20\%$. Further details with respect to the derivation of this expression are described in the Appendix on page 43.

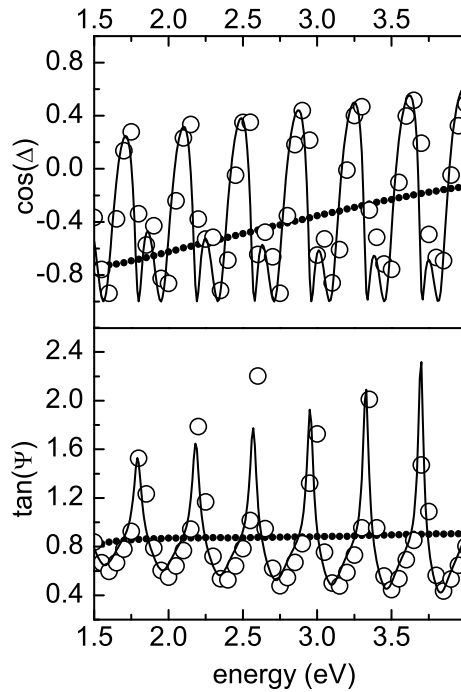


Figure 2.7: Ellipsometry spectrum for an as-anodized porous anodic aluminium oxide film. The open circles represent experimental data, while the solid lines are obtained from a fitting procedure using a five-layer. The small dots represent the spectrum for a sample prior to anodization.

2.4.2 Ellipsometry spectra of as-anodized aluminium oxide

In fig. 2.7 a typical ellipsometry spectrum is shown for a film prior to (small dots) and after (open symbols) anodization. The spectrum before anodizing the sample is almost identical to a bulk aluminium sample, and can therefore be adequately modeled using a single aluminium/air interface, with a thin layer of natural oxide on the surface. It is evident that the optical response after anodization is completely different from that of bulk aluminium. As already described in previous sections, anodic oxidation leads to a highly porous, oxidic structure of approximately 1400nm thickness, which is essentially transparent for visible light. This explains the oscillations observed

in both $\cos(\Delta)$ and $\tan(\Psi)$ in fig. 2.7, which arise from interference of light reflected at the platinum/aluminium oxide and at the aluminium oxide/air interfaces. As the optical thickness increases the number of oscillations also increase.

The solid lines in fig. 2.7 represent the result of a fitting procedure using the Abelès matrix algorithm and the optical model described in preceding sections. The aforementioned three, physically relevant parameters are varied, leading to a thickness of $1400 \pm 40 \text{ nm}$, a cylinder fraction $f_{\text{cyl}} = 9.9 \pm 0.3\%$ and a nanoporosity $f_{\text{p}} = 28 \pm 3\%$. These results are in good, quantitative agreement with what we concluded from analysis of the SEM images on identical samples.

To verify the accuracy of our model we also performed measurements at different incident angles. Although the absolute values of both $\cos(\Delta)$ and $\tan(\Psi)$ are different, oscillations similar to those in fig. 2.7 are observed. Comparison of the experimental results at different angles to calculations of the optical response using the parameters obtained from the fitting procedure as described in relation to fig. 2.7 yields perfect correlation between the calculation and the measurements, supporting the validity of our model.

Despite the convincing results presented above, one might argue that, even after prolonged drying under ambient conditions, some aqueous solution may still be present in the porous structure. Especially for nanoporous oxide materials, it has been reported that water, incorporated during the preparation, is still present within the nanovoids [47]. This would have a pronounced influence on the analysis of the optical response in terms of eqs. 2.6, 2.7 and 2.8. To obtain an indication if there is any water present in as-anodized samples after drying in air, we performed ellipsometry measurements on such a sample before and after heating to approximately 200°C under moderate vacuum conditions. All optical spectra, both before and after heating in vacuum were identical, indicating the absence of any water within the porous structure of as-anodized samples. This indicates that either there is indeed no water present within the nanoporous matrix, or that the water is contained in such small volumes that capillary forces prevent evaporation of the aqueous solvent even at elevated temperature. The latter explanation, however, may be dismissed. As we will show in the next section, chemical etching does not affect the nanoporous structure, presumably due to the fact that aqueous solution is not able to penetrate into the (sub)nanometer sized voids.

2.4.3 Tunable pore sizes by chemical etching

Chemical etching in aqueous phosphoric acid solutions leads to controlled, homogeneous widening of the pores along their entire length, as can be seen in SEM images such as those in figs. 2.3 and 2.8(a). Apparently, diffusion of the etchant or etch products is not rate limiting. The average pore diameter in fig. 2.8(a) after immersion of the as-anodized sample in 2 vol.% H_3PO_4 solution for 10min increases from 11.5nm to approximately 22nm. Upon prolonged etching and/or a higher concentration of phosphoric acid, the pores become wider, as we will discuss later.

Furthermore, the enlargement of the pores now also enables the study

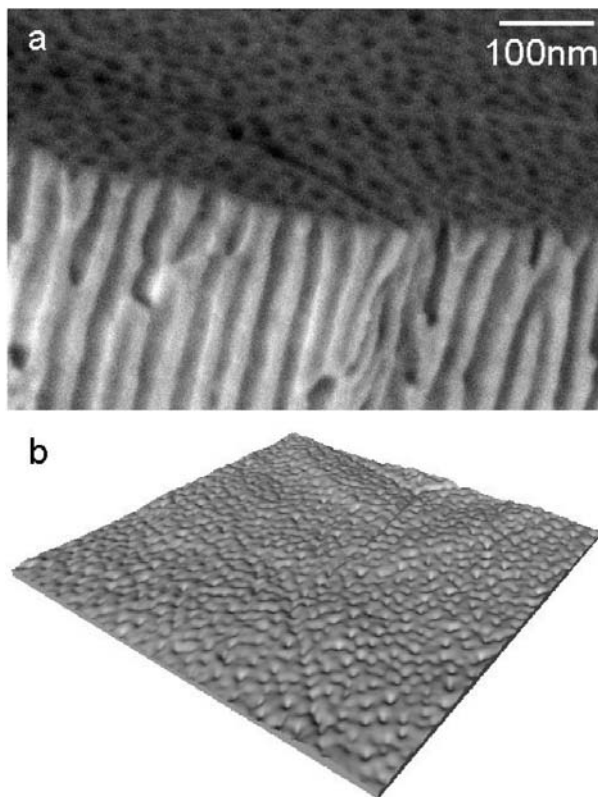


Figure 2.8: (a) Scanning electron microscope and (b) atomic force microscope images of a porous aluminium oxide sample after chemical etching for 10min in a 2 vol.% H_3PO_4 aqueous solution. Scan size in the AFM image is $1\mu\text{m} \times 1\mu\text{m}$.

of these membranes using atomic force microscopy (AFM), as shown in fig. 2.8(b). AFM measurements are performed using a Picoscan (Molecular Imaging) operated in AC mode, using silicon cantilevers (Nanosensors). The pore size of as-anodized samples is too small compared to the tip radius; the tip cannot reach into the pores to obtain a good image. After sufficient pore widening, the pores can be imaged but they appear markedly smaller than their actual size.

We studied the effect of chemical etching using spectroscopic ellipsometry, with a two-fold objective: (i) The use of a non-invasive technique, which is readily available, allows a fast characterization of the temporal-evolution of the porous system, and (ii) The controlled etching of the pores allows us to verify the validity and assess the accuracy of our optical model as it has been described in the previous section.

In fig. 2.9 the ellipsometry spectrum of a sample after chemical etching for 10min in a 3 vol.% H_3PO_4 aqueous solution is shown. Comparison with the results in fig. 2.7 indicates that the number of oscillations has decreased. This can be understood qualitatively by the fact that, owing to the higher cylinder fraction, the optical thickness is reduced, which gives rise to a change of the interference. Also, with increasing energy the amplitude of the oscillations in both $\cos(\Delta)$ and $\tan(\Psi)$ decreases. This is direct evidence for the contribution of anisotropy to the optical response. In the absence of anisotropy, the amplitude of the oscillations will be identical over the entire energy range. The solid lines in fig. 2.9 are obtained by fitting the results to our optical model, as described in the previous section. Clearly, the calculated lines are in perfect agreement with the measured data, thereby supporting our model. The fit results indicate a thickness of 1395nm, a cylinder void fraction $f_{\text{cyl}} = 46\%$ and a nanoporosity $f_{\text{p}} = 34\%$. When we compare these results with that obtained for the as-anodized sample, chemical etching leads to a significant increase of the cylinder fraction. It may be expected that chemical etching leads to a decrease of the film thickness, but the change is within the error of the fitting procedure. The same holds for the negligible increase of the nanoporosity during chemical etching.

The cylinder fraction is related to the average pore radius through

$$f_{\text{cyl}} = \rho_{\text{cyl}} \cdot \pi r^2 \quad (2.9)$$

where ρ_{cyl} is the pore density as determined from SEM and/or AFM images, such as those in figs. 2.2 and 2.8(b). This allows us to compare the results obtained from the analysis of the ellipsometry spectra to the average pore radius determined from cross-section SEM images. In fig. 2.10 the latter

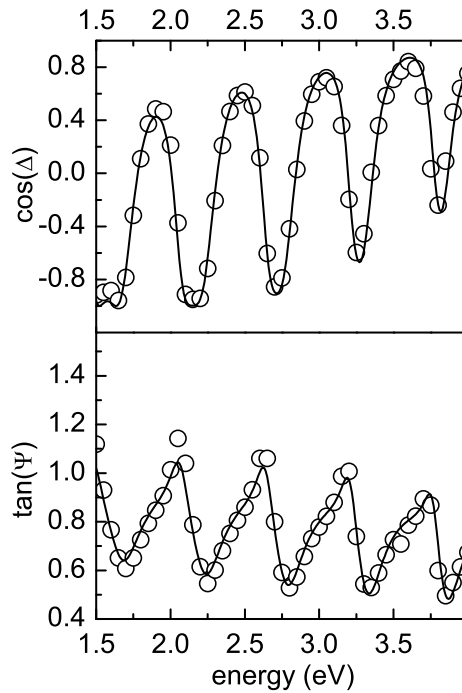


Figure 2.9: Ellipsometry spectrum for a porous anodic aluminium oxide film, after chemical etching for 10min in 3 vol.% H_3PO_4 aqueous solution. The open circles represent experimental data, while the solid lines result from a fitting procedure using a five-layer model.

is shown as a function of the pore radius derived from ellipsometry results using eq. 2.9. Clearly, over the entire range of cylinder fractions there is a good agreement, providing valuable evidence for the validity of our optical model.

As is to be expected, the etch rate, and therewith the pore widening process, depend on the concentration of the phosphoric acid solution. This is shown in fig. 2.11, in which the cylinder fraction is plotted as a function of etch time for different H_3PO_4 concentrations. With an increasing amount of etchant in solution, the etch rate, and thus the rate with which the pores are widened, rise. A simple model is used to analyze the results in fig. 2.11. We assume a linear etch rate $\nu(c) = dr/dt$, which only depends on the H_3PO_4

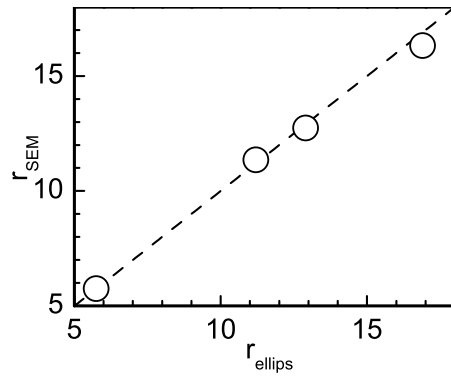


Figure 2.10: The average pore radius, determined from SEM images after different etching times, as a function of the radius determined from ellipsometry spectra.

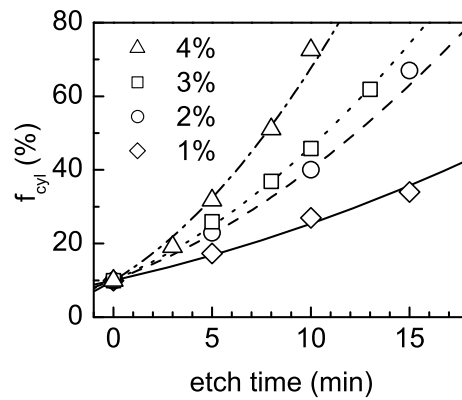


Figure 2.11: Cylinder fraction f_{cyl} as a function of the etching time in different H_3PO_4 aqueous solutions. The different symbols correspond to H_3PO_4 concentrations of 1, 2, 3, and 4 vol.%, respectively, as indicated. The lines represent fit results.

concentration c . Correspondingly, the pore radius r increases linearly with time t

$$r = r_0 + \nu t \quad (2.10)$$

where $r_0 = 5.75\text{nm}$ is the initial pore radius after anodization prior to chemical etching. The time-dependence of the cylinder fraction is obtained by taking the derivative of eq. 2.9

$$\frac{df_{\text{cyl}}}{dt} = \frac{df_{\text{cyl}}}{dr} \frac{dr}{dt} = \rho_{\text{cyl}} \cdot 2\pi r \cdot \nu \quad (2.11)$$

where $dr/dt = \nu$. After substitution of the time-dependence of the pore radius (eq. 2.10), the above expression is integrated to yield

$$f_{\text{cyl}} = f_0 + \pi\rho_{\text{cyl}} (2r_0\nu t + \nu^2 t^2) \quad (2.12)$$

where $f_0 = \rho_{\text{cyl}} \cdot \pi r_0^2$ is the initial cylinder fraction before chemical etching. With the linear etch rate $\nu(c)$ being the only parameter, we fitted the data in fig. 2.11. The results for the different H_3PO_4 concentrations are represented by the broken lines in fig. 2.11. A log-log plot of the etch rate $\nu(c)$ as a function of the H_3PO_4 concentration c indicates that, within the concentration range of our experiments, the order of the reaction amounts to $n = 2/3$, with $\nu(c) = k \cdot c^n$. To further substantiate this, the etch rate is replotted as a function of $c^{2/3}$ in fig. 2.12. The solid line represents a linear fit through the origin. The rate constant, determined from the slope, amounts to $k = 1.7 \times 10^{-13} \text{m}^3 \text{s}^{-1} \text{mol}^{-2/3}$.

Finally, the analysis of ellipsometry spectra using the aforementioned model also yields values for the nanoporosity f_p . The results for different phosphoric acid concentrations and etch times are shown in fig. 2.13. Although there appears to be a relatively small increase of f_p in the initial stages of the etch procedure, it is much less pronounced than the increase of the cylinder fraction f_{cyl} in fig. 2.11. In fact, the variation of f_p is almost within the numerical fitting errors. The slight increase in the first stages of chemical etching may indicate that the pore walls are comprised of aluminium oxide with a slightly higher density than the major part of the alumina matrix. In fact, this is in line with previous studies by Fukuda [53] on the anion contamination in the aluminium oxide matrix. From this work it was concluded that the anion concentration is lower near the pore walls compared to the center of the oxide. A lower anion concentration would imply a higher aluminium oxide density of the pore walls. Upon etching this denser alumina layer, the overall nanoporosity, as determined by ellip-

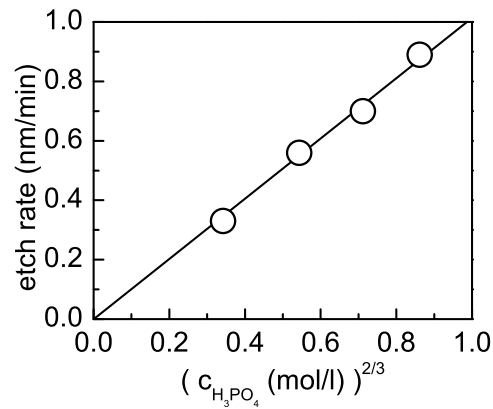


Figure 2.12: The linear etch rate, obtained from the fitted curves in fig. 2.11, as a function of the H_3PO_4 concentration. The solid line represents a fit.

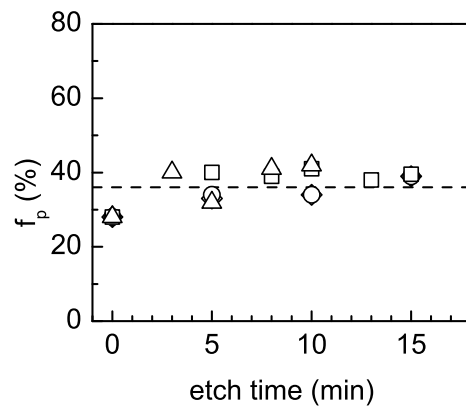


Figure 2.13: The nanoporosity f_p obtained from analysis of ellipsometry spectra, as a function of the etch time in H_3PO_4 solutions. The symbols correspond to different H_3PO_4 concentrations, see fig. 2.11. The horizontal dashed line is merely a guide to the eye. The data is plotted on the same scale as the results in fig. 2.11 to allow straightforward comparison.

sometry, increases slightly.

Furthermore, there is no discernible difference for high and low H_3PO_4 concentrations. Apparently, owing to their very small size, the voids within the nanoporous structure are not accessible to the solvent which inhibits chemical etching in these (sub)nanometer voids. This is not unlikely, as the considerable deformations during the anodic oxide formation give rise to a large number of defects, such as dislocations and vacancies [50, 54, 55]. Obviously, these small 'voids' in the amorphous oxide matrix are not accessible to the relatively large water molecules.

The average nanoporosity, indicated by the dashed line, amounts to approximately 36%. This is in good agreement with the value we indirectly deduced on the basis of the film thickness increase upon anodization of the aluminium, as determined from cross-section SEM images (fig. 2.3).

2.5 Conclusions

We have presented a detailed characterization study of porous aluminium oxide formed through anodization of thin film aluminium samples with a well-defined geometry. Prior to anodization, the thicknesses of the aluminium film, the platinum layer, which provides sufficient electrical conduction, and the titanium adhesion layer was determined using scanning electron microscopy in combination with Rutherford backscattering. X-ray diffraction experiments yield powder-like spectra, indicating that both the platinum and aluminium layers are polycrystalline; the limited titanium thickness does not yield measurable diffracted intensities.

Electron microscopy clearly shows the formation of randomly distributed, but almost perfectly aligned cylindrical pores with their long axis perpendicular to the film/substrate interface. Additionally, comparison of x-ray diffraction spectra obtained before and after anodization show a nearly complete transformation of aluminium to aluminium oxide.

Ellipsometry spectra, obtained after anodization, were analyzed in terms of a newly developed model, which contains only three physically relevant parameters: the film thickness, the cylindrical pore fraction and the nanoporosity of the remaining aluminium oxide matrix. The model accurately reproduces the experimentally observed features, and the absolute values of the fitting parameters are in perfect agreement with what is observed in electron microscopy images.

Chemical etching of the porous structure in diluted phosphoric acid solution gives rise to a homogeneous widening of the pores over their entire

length. This provides us with an ideal system to verify the accuracy of our optical model. The increase of the cylinder fraction with increasing etching time and etchant concentration, as determined from ellipsometry spectra, is again in perfect agreement with electron microscopy images. It enabled an easy determination of the order and rate constant of the etching reaction. In contrast to the cylinder fraction, the nanoporosity of the aluminium oxide remains unchanged. This is presumably due to the inaccessibility of the small defect-like voids in the amorphous oxide to the etch solution.

Appendix: Alternative Bruggeman EMA

In his original work, Bruggeman [44] provides expressions for the effective dielectric function ε' of small spherical inclusions of fraction δ' , with dielectric function ε_i , in a host matrix with ε_h , for both the two and three dimensional cases. These equations, referred to as the Rayleigh formulas, can be summarized in a generalized expression

$$\frac{\varepsilon' - \varepsilon_h}{\varepsilon' + (n-1)\varepsilon_h} = \delta' \frac{\varepsilon_i - \varepsilon_h}{\varepsilon_i + (n-1)\varepsilon_h} \quad (2.13)$$

with $n = 2, 3$ the system dimension. Rewriting yields an expression for the effective dielectric function

$$\varepsilon' = \varepsilon_h \frac{1 + \delta' (n-1) \frac{\varepsilon_i - \varepsilon_h}{\varepsilon_i + (n-1)\varepsilon_h}}{1 - \delta' \frac{\varepsilon_i - \varepsilon_h}{\varepsilon_i + (n-1)\varepsilon_h}}. \quad (2.14)$$

As δ' is small, we may neglect higher order terms to obtain

$$\varepsilon' \approx \varepsilon_h \left(1 + \delta' n \frac{\varepsilon_i - \varepsilon_h}{\varepsilon_i + (n-1)\varepsilon_h} \right). \quad (2.15)$$

The above is only valid for infinitely small inclusions. Bruggeman [44] extended this to an arbitrary concentration f of one medium dispersed in the host material. Consider a first inclusion δ' of medium with ε_i in the host with ε_h ; this will result in a dielectric function ε' of this quasi-homogeneous medium, as given by eq. 2.15. A second inclusion δ'' will give rise to an effective dielectric function

$$\varepsilon'' \approx \varepsilon' \left(1 + \delta'' n \frac{\varepsilon_i - \varepsilon'}{\varepsilon_i + (n-1)\varepsilon'} \right) \quad (2.16)$$

where ε' is the dielectric function of the quasi-homogeneous material before adding δ'' . In general, to obtain an increase $d\delta_1$ of material with dielectric function ε_1 , in case of an already present fraction δ_1 , an amount $\delta' = \frac{d\delta_1}{1-\delta_1}$ needs to be added. This can be explained as follows: A fraction δ_1 of the amount δ' is distributed in the already present quantity δ_1 , while only a fraction $1 - \delta_1$ of δ' leads to an increase of δ_1 .

From eq. 2.16 we find

$$\frac{d\varepsilon}{n\varepsilon} = \frac{d\delta_1}{1-\delta_1} \cdot \frac{\varepsilon_i - \varepsilon}{\varepsilon_i + (n-1)\varepsilon} \quad (2.17)$$

which can be rewritten to yield

$$\left(\frac{1}{\varepsilon_i - \varepsilon} + \frac{1}{n\varepsilon} \right) d\varepsilon = \frac{d\delta_1}{1-\delta_1}. \quad (2.18)$$

The right hand side is integrated from $\delta_1 = 0$ to $\delta_1 = f$, while on the left we integrate from $\varepsilon = \varepsilon_h$ (initially at $\delta_1 = 0$ there are no inclusions) to $\varepsilon = \varepsilon_{or}$ (the final effective dielectric function of a fraction f of the medium with dielectric function ε_i in the host matrix with ε_h):

$$\int_{\varepsilon_h}^{\varepsilon_{or}} \left(\frac{1}{\varepsilon_i - \varepsilon} + \frac{1}{n\varepsilon} \right) d\varepsilon = \int_0^f \frac{d\delta_1}{1-\delta_1} \quad (2.19)$$

We obtain

$$1 - f = \frac{\varepsilon_i - \varepsilon_{or}}{\varepsilon_i - \varepsilon_h} \sqrt[n]{\frac{\varepsilon_h}{\varepsilon_{or}}} \quad (2.20)$$

which, for a two dimensional system ($n = 2$) with $\varepsilon_i = \varepsilon_a$ and $\varepsilon_h = \varepsilon_p$, yields eq. 2.8 used in the text.

References

- [1] F. Keller, M. S. Hunter, and D. L. Robinson, *J. Electrochem. Soc.* **100**, 411 (1953).
- [2] H. Masuda, H. Hasegawa, and S. Ono, *J. Electrochem. Soc.* **144**, L127 (1997).
- [3] G. E. Thompson, *Thin Solid Films* **297**, 192 (1997).
- [4] H. Masuda, H. Yamada, M. Satoh, H. Asoh, M. Nakao, and T. Tamamura, *Appl. Phys. Lett.* **71**, 2770 (1997).
- [5] O. Jessensky, F. Müller, and U. Gösele, *Appl. Phys. Lett.* **72**, 1173 (1998).

- [6] A. P. Li, F. Müller, A. Birner, K. Nielsch, and U. Gösele, *J. Appl. Phys.* **84**, 6023 (1998).
- [7] A. P. Li, F. Müller, A. Birner, K. Nielsch, and U. Gösele, *Adv. Mater.* **11**, 483 (1999).
- [8] A. P. Li, F. Müller, A. Birner, K. Nielsch, and U. Gösele, *J. Vac. Sci. Technol. A* **17**, 1428 (1999).
- [9] A. P. Li, F. Müller, and U. Gösele, *Electrochem. Solid-State Lett.* **3**, 131 (2000).
- [10] D. Crouse, Y. H. Lo, A. E. Miller, and M. Crouse, *Appl. Phys. Lett.* **76**, 49 (2000).
- [11] G. D. Sulka, S. Stroobants, V. Borghs, and J. P. Celis, *J. Electrochem. Soc.* **149**, D97 (2002).
- [12] Z. Yuan, H. Huang, and S. Fan, *Adv. Mater.* **14**, 303 (2002).
- [13] T. Gao, G. Meng, J. Zhang, S. Sun, and L. Zhang, *Appl. Phys. A* **74**, 403 (2002).
- [14] K. Nielsch, J. Choi, K. Schwirn, R. B. Wehrspohn, and U. Gösele, *Nano Lett.* **2**, 677 (2002).
- [15] W. Schwarzacher, O. I. Kasyutich, P. R. Evans, M. G. Darbyshire, G. Yi, V. M. Fedosyuk, F. Rousseaux, E. Cambril, and D. Decanini, *J. Magn. Magn. Mater.* **199**, 185 (1999).
- [16] J. C. Hulteen and C. R. Martin, *J. Mater. Chem.* **7**, 1075 (1997).
- [17] T. A. Hanaoka, A. Heilmann, M. Kröll, H. Kormann, T. Sawitowski, G. Schmid, P. Jutzi, A. Klipp, U. Kreibig, and R. Neuendorf, *Appl. Organomet. Chem.* **12**, 367 (1998).
- [18] G. Ihlein, B. Junges, U. Junges, F. Laeri, F. Schüth, and U. Vietze, *Appl. Organomet. Chem.* **12**, 305 (1998).
- [19] X. Y. Zhang, L. D. Zhang, W. Chen, G. W. Meng, M. J. Zheng, L. X. Zhao, and F. Phillipp, *Chem. Mater.* **13**, 2511 (2001).
- [20] G. Schmid, *J. Mater. Chem.* **12**, 1231 (2002).
- [21] R. M. Metzger, V. V. Konovalov, M. Sun, T. Xu, G. Zangari, B. Xu, M. Benakli, and W. D. Doyle, *IEEE Transact. Magn.* **36**, 30 (2000).
- [22] P. M. Paulus, F. Luis, M. Kröll, G. Schmid, and L. J. de Jongh, *J. Magn. Magn. Mater.* **224**, 180 (2001).
- [23] B. M. I. van der Zande, M. R. Böhmer, L. G. J. Fokkink, and C. Schönenberger, *Langmuir* **16**, 451 (2000).
- [24] F. Müller, A. D. Müller, M. Kröll, and G. Schmid, *Appl. Surf. Sci.* **171**, 125 (2001).
- [25] G. Sauer, G. Brehm, S. Schneider, K. Nielsch, R. B. Wehrspohn, J. Choi, H. Hofmeister, and U. Gösele, *J. Appl. Phys.* **91**, 3243 (2002).
- [26] M. R. Black, M. Padi, S. B. Cronin, Y. M. Lin, O. Rabin, T. McClure,

- G. Dresselhaus, P. L. Hagelstein, and M. S. Dresselhaus, *Appl. Phys. Lett.* **77**, 4142 (2000).
- [27] C. M. Zelenski, G. L. Hornyak, and P. K. Dorhout, *Nanostruct. Mater.* **9**, 173 (1997).
- [28] M. S. Sander, R. Gronsky, T. Sands, and A. M. Stacy, *Chem. Mater.* **15**, 335 (2003).
- [29] Z. Wang and H. Li, *Appl. Phys. A* **74**, 201 (2002).
- [30] T. Iwasaki, T. Motoi, and T. Den, *Appl. Phys. Lett.* **75**, 2044 (1999).
- [31] S. H. Jeong, H. Y. Hwang, K. H. Lee, and Y. Leong, *Appl. Phys. Lett.* **78**, 2052 (2001).
- [32] M. Steinhart, J. H. Wendroff, A. Greiner, R. B. Wehrspohn, K. Nielsch, J. Schilling, J. Choi, and U. Gösele, *Science* **296**, 1997 (2002).
- [33] D. J. Peña, J. K. N. Mbindyo, A. J. Carado, T. E. Mallouk, C. D. Keating, B. Razavi, and T. S. Mayer, *J. Phys. Chem. B* **106**, 7458 (2002).
- [34] G. Sberveglieri, R. Murri, and N. Pinto, *Sens. Actuators B* **23**, 177 (1995).
- [35] R. K. Nahar and V. K. Khanna, *Sens. Actuators B* **46**, 35 (1998).
- [36] A. V. Kukhta, G. G. Gorokh, E. E. Kolesnik, A. I. Mitkovets, M. I. Taoubi, Y. A. Koshin, and A. M. Mozalev, *Surf. Sci.* **507–510**, 593 (2002).
- [37] R. M. A. Azzam and N. H. Bashara, *Ellipsometry and polarized light*, North Holland, Amsterdam, 1987.
- [38] J. De Laet, J. Vanhellefont, H. Terryn, and J. Vereecken, *Appl. Phys. A* **54**, 72 (1992).
- [39] J. De Laet, J. Vanhellefont, H. Terryn, and J. Vereecken, *Thin Solid Films* **233**, 58 (1993).
- [40] J. De Laet, H. Terryn, and J. Vereecken, *Thin Solid Films* **320**, 241 (1998).
- [41] N. Stein, M. Rommelfangen, V. Hody, L. Johann, and J. M. Lecuire, *Electrochim. Acta* **47**, 1811 (2002).
- [42] W. Hu, D. Gong, Z. Chen, L. Yuan, K. Saito, C. A. Grimes, and P. Kichambare, *Appl. Phys. Lett.* **79**, 3083 (2001).
- [43] S. Z. Chu, K. Wada, S. Inoue, and S. Todoroki, *J. Electrochem. Soc.* **149**, B321 (2002).
- [44] D. A. G. Bruggeman, *Ann. Phys.* **24**, 636 (1935).
- [45] O. Wien, *Phys. Z.* **12**, 332 (1904).
- [46] F. Genereux, S. W. Leonard, H. M. van Driel, A. Birner, and U. Gösele, *Phys. Rev. B* **63**, 161101 (2001).
- [47] N. Benes, G. Spijksma, H. Verweij, H. Wormeester, and B. Poelsema,

- AICHe J. **47**, 1212 (2001).
- [48] E. D. Palik, *Handbook of optical constants of solids*, volume I, Academic Press, Orlando, 1985.
- [49] E. D. Palik, *Handbook of optical constants of solids*, volume II, Academic Press, Boston, 1991.
- [50] E. Palibroda, T. Farcas, and A. Lupsan, *Mater. Sci. Eng. B* **32**, 1 (1995).
- [51] <http://www.webelements.com> .
- [52] E. S. Kooij, H. Wormeester, A. C. Gâlcă, and B. Poelsema, *Electrochem. Solid-State Lett.* **6**, B52 (2003).
- [53] Y. Fukuda, *Trans. Nat. Res. Inst. Metals* **17**, 25 (1975).
- [54] Y. Du, W. L. Cai, C. M. Mo, J. Chen, L. D. Zhang, and X. G. Zhu, *Appl. Phys. Lett.* **74**, 2951 (1999).
- [55] G. S. Huang, X. L. Wu, Y. F. Mei, X. F. Shao, and G. G. Siu, *J. Appl. Phys.* **93**, 582 (2003).

Chapter 3

Linear magneto-optical properties of ferrofluids: A transmission ellipsometry study

Abstract

Linear birefringence and dichroism of magnetite ferrofluids are studied simultaneously using spectroscopic ellipsometry in transmission mode. It is shown that this versatile technique enables highly accurate characterization of magneto-optical phenomena. The magnetic field-dependent linear birefringence and dichroism as well as the spectral dependence are shown to be in line with previous results. Despite the qualitative agreement with established models for magneto-optical phenomena, these fail to provide an accurate, quantitative description of our experimental results using the bulk dielectric function of magnetite. We discuss the results in relation to these models, and indicate how the modified dielectric function of the magnetite nanoparticles can be obtained.

3.1 Introduction

Colloidal suspensions of single-domain ferro- or ferrimagnetic nanoparticles are generally referred to as ferrofluids. Typical materials constituting the particles are pure metals (Fe, Ni, and Co) or cubic spinel oxides such as $\text{Fe}_2\text{O}_3\text{-}'\text{X}'\text{O}$, where $'\text{X}'=\text{Fe, Co, Ni or Cd}$. The size of the particles is generally in the 3 – 20nm range. To avoid precipitation and aggregation of the particles suspended in polar or non-polar solvents, various types of surfactants are used to induce steric or electrostatic inter-particle repulsive interactions.

Many different application fields have benefited from the characteristic properties of ferrofluids. They are found in mechanical devices, such as seals, bearings and dampers, and also in electromechanical devices such as loudspeakers, stepper motors and sensors). Ferrofluids have also been employed as a material for testing components such a magnetic tapes, stainless steels and turbine blades in a non-destructive way.

The optical properties of ferrofluids under the application of an external magnetic field has initiated substantial research effort, ultimately aimed at incorporating the optically active ferrofluids in applications such as optical shutters, switches, and tunable polarizing or phase-changing elements. The transition from an optically isotropic material to an (optically) anisotropic medium was first observed by Majorana [1, 2] in colloids as the magnetic equivalent of the electrical Kerr effect. Shortly after this, Cotton and Mouton [3] observed similar magnetically induced birefringence and dichroism in liquids. Consequently, these optical phenomena, tunable via the applied magnetic field, are often referred to as Cotton-Mouton effects.

Well-described synthesis procedures [4–8], and also the commercial availability of a wide variety of ferrofluids has stimulated scientific research in this field. Both experimental and theoretical work is focused on elucidating the origin of the magneto-optical properties of these suspensions [9–27]. Also, their possible use in optical devices is investigated.

Initially, the theoretical description of the magneto-optical properties of ferrofluids was based on the alignment of slightly non-spherical particles with uniaxial magnetic anisotropy in an applied magnetic field [9]. The magnetically induced optical anisotropy was attributed to the shape anisotropy of the prolate ellipsoidal particles with different polarizabilities along their short and long axes [9, 16]. The possible contribution of pre-existing aggregates, or conglomerates formed in the applied field have been discussed and investigated [11–14, 18]. Linear chains consisting of many particles have also been considered as a possible explanation for the magneto-optical proper-

ties [15]. Finally, Rasa presented a general theory for all magneto-optical phenomena due to non-interacting particles, in which the dielectric tensor of the ferrofluid is considered [21, 22].

The magneto-optical properties of ferrofluids have been investigated in the past with a number of different experimental set-ups [9, 10, 14, 17–20, 22]. Most often only birefringence is considered, and the magnetically induced dichroism is neglected. However, in some cases both aforementioned quantities are obtained, at a single wavelength or over a larger spectral range, but in the analysis the quantitative relation between the birefringence and the dichroism is not considered.

In this work we study both linear magneto-optical properties, i.e. birefringence and dichroism, of an oil-based ferrofluid in the presence of a homogeneous externally applied magnetic field. We demonstrate the versatility of using a spectroscopic ellipsometer in transmission mode for simultaneously measuring the aforementioned linear magneto-optical quantities with high accuracy. The relations between the ellipsometric quantities Ψ and Δ on one hand and the birefringence and dichroism on the other hand, are derived. In a final section, the results are compared to previous work and existing theoretical models, which describe magneto-optical behavior.

3.2 Ferrofluid synthesis and characterization

3.2.1 Synthesis

All measurements described in this paper are done using oleic acid stabilized magnetite (Fe_3O_4) suspensions, synthesized by reduction of ferrous and ferric chloride by ammonium hydroxide as for example described by Van Ewijk *et al.* [6]. In a typical synthesis, 1.3gr FeCl_3 and 0.5gr FeCl_2 are dissolved in 80ml of demineralized water. While stirring vigorously, 5ml 25% NH_3 is added, resulting in a black precipitate. The magnetite is precipitated using a magnet and the supernatant is discarded, after which it is washed at least 4 times in demineralized water, until the solution pH is 7. Subsequently, 50ml of demineralized water and 50ml of oleic acid are added to the washed precipitate, and the mixture is stirred for at least 30min while heating to 50°C . After cooling of the mixture, the water is removed, and 50ml of acetone is added. Using a magnet, the magnetite is precipitated and the supernatant is discarded. This washing procedure is repeated at least 4 times, after which the acetone is removed from the black substance by moderate heating. Finally, 50ml cyclohexane is added to the dried residue to yield a suspension with a volume fraction of approximately $\Phi_0 = 1.56 \times 10^{-3}$.

3.2.2 Characterization

A typical TEM image of the as-prepared magnetite ferrofluid, obtained using a Philips CM30 Twin/STEM system with a standard carbon-coated copper grid, is shown in fig. 3.1. As can be seen, the shape of the magnetite nanoparticles is very irregular. To assess the size dispersion and shape anisotropy, TEM images are analyzed by determining the long and short axes of a large number of particles. The resulting histograms of both short and long axes are shown in fig. 3.2(a) and (b), respectively. Assuming a normal distribution, the average diameter \bar{d} for the short and long axes amount to 5.9nm and 7.7nm, respectively. The polydispersity $100\% \cdot \sigma / \bar{d}$ of both distributions is approximately 30%, with $\sigma = \sqrt{\overline{d^2} - \bar{d}^2}$ the standard deviation. In addition to what is clearly observed in fig. 3.1, this indicates that the suspension is far from monodisperse. For a monodisperse suspension, the polydispersity parameter is generally required to be less than 5%, or at most 10% [28]. Often the particle size distributions are considered to follow a log-normal

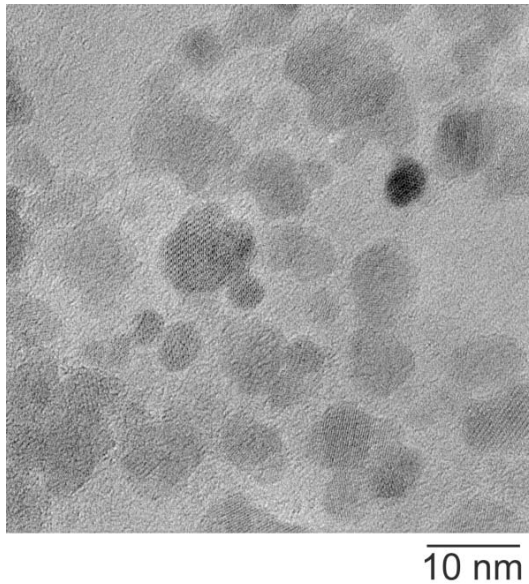


Figure 3.1: TEM image of Fe_3O_4 nanoparticles in a magnetite ferrofluid, synthesized as described in the text.

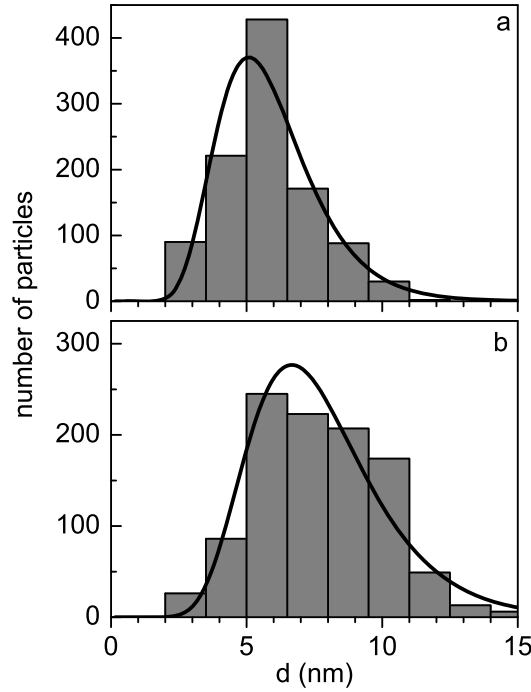


Figure 3.2: Size distribution of the short (a) and long (b) diameters of the Fe_3O_4 nanoparticles as determined from TEM images such as the one in fig. 3.1

distribution [19, 22], given by

$$f(d) = \frac{1}{s \cdot d \cdot \sqrt{2\pi}} \exp\left(-\frac{\ln^2(d/d_0)}{2s^2}\right) \quad (3.1)$$

where $\ln(d_0)$ and s are the mean value and standard deviation of $\ln(d)$. The solid lines in fig. 3.2 show the log-normal functions obtained from the distributions. For the short and long diameters, $d_0 = 5.6\text{nm}$ and $d_0 = 7.4\text{nm}$ are obtained, while the standard deviation amounts to $s = 0.31$ for both diameter distributions. These parameters will be employed in the analysis of the magneto-optical properties.

To assess the optical properties of isolated particles, UV-VIS absorbance¹

¹The absorbance is defined by $A = -\log(I/I_0)$. The extinction coefficient γ_{ext} is given by $I/I_0 = \exp(-\gamma_{\text{ext}}z)$ with I/I_0 the attenuation of the incident light with intensity I_0 at a depth z .

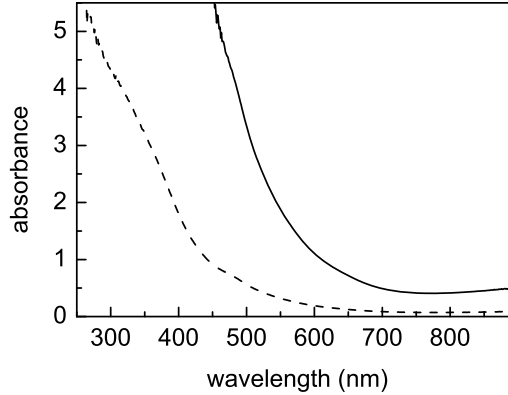


Figure 3.3: UV-Vis absorbance spectra of Fe_3O_4 ferrofluids as used in this work. As-prepared suspensions were diluted to yield fill fractions of $\Phi = 1.56 \times 10^{-4}$ and $\Phi = 2.60 \times 10^{-5}$ (solid and dashed lines, respectively).

spectra were recorded on a Varian Cary 300 Scan spectrophotometer in double-beam mode, using a 1cm cuvette filled with only the solvent (cyclohexane) as reference. The ferrofluid appearance is dark brown to black, even for moderate fill fractions. This is also observed in the spectra in fig. 3.3. For the relatively high fill fraction ($\Phi = 1.56 \times 10^{-4}$, solid line) the absorbance exceeds the experimentally available range for wavelengths below approximately 500nm. Considerably more diluted suspensions still exhibit the strong increase of the absorbance toward shorter wavelengths.

3.3 Linear magneto-optics

3.3.1 Transmission ellipsometry setup

Magneto-optical properties are investigated using a home-built rotating polarizer spectroscopic ellipsometer, equipped with a Xe lamp, a rotating polarizer, fixed analyzer and a scanning monochromator [29]. Measurements are performed in the visible region of the spectrum. Standard quartz spectrometer cuvettes (Starna) with optical path lengths of 1.0mm and 10mm are used. A cuvette is placed in a homogeneous DC magnetic field generated between the poles of a home-built water-cooled electromagnet, connected to a Delta Elektronika SM3540 power supply. A more elaborate description of our magnet configuration will be presented in chapter 4. The direction of the applied magnetic field is in all cases perpendicular to the light propa-

gation direction, allowing only the determination of linear magneto-optical birefringence and dichroism.

The incident light is linearly polarized, which upon transmission through an anisotropic medium is generally transformed to elliptically polarized light. The complex transmission coefficient ρ is defined through

$$\rho = \frac{t_p}{t_s} = \tan(\Psi) \exp(i\Delta) \quad (3.2)$$

where t_p and t_s are the transmission coefficients for parallel and perpendicular polarizations, respectively [30]. In reflection ellipsometry, the polarization directions are defined with respect to the plane of reflection, spanned by the incoming and outgoing light beams. Prior to a measurement, the azimuthal angles of the optical components, such as the polarizer, the analyzer and possibly a compensator, are accurately calibrated with respect to this plane of reflection. In the absence of a magnetic field, the ferrofluid in the cuvette is isotropic and, since we are using the ellipsometer in transmission mode, such a reference plane can not be defined. However, when a magnetic field is applied, we can calibrate all angles with respect to the field direction. In analogy with the more frequently employed reflection ellipsometry, the p- and s-polarization directions are defined as being parallel and perpendicular to the magnetic field, respectively.

To calibrate the ellipsometer components, we use a standard residue calibration as described by De Nijs *et al.* [31] for reflection ellipsometry. In a similar way, it can be applied to our transmission configuration. The residue function R is defined by

$$R = 1 - \eta^2 + 4\eta^2 \left(\frac{\tan(\Psi) \sin(\Delta) \tan(A)}{\tan^2(\Psi) + \tan^2(A)} \right)^2 \quad (3.3)$$

where A is the angle of the analyzer, and η is a frequency dependent factor describing the difference in AC and DC attenuation of the electronics; generally it is found that $\eta < 1$. The angle A , which defines the reference plane, is found in the minimum of eq. 3.3.

In fig. 3.4 the measured residue is plotted as a function of the analyzer angle A for different values of the applied magnetic field. As expected, the residue R does not depend on the analyzer angle in the absence of an external magnetic field. In this case, the optical system comprising the cuvette with ferrofluid, is isotropic and the aforementioned p- and s-directions are not defined. Upon applying a very moderate magnetic field, an angle-dependence is observed. The residue exhibits a minimum, which is independent of the

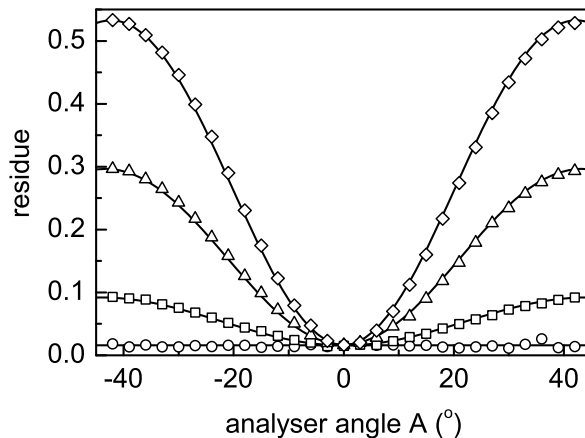


Figure 3.4: Residue calibration curves for different values of the externally applied magnetic field. In the absence of a magnetic field the residue is independent of the analyzer angle A , indicated by the circles. The squares, triangles and diamonds correspond to magnetic flux densities of 0.014T, 0.025T and 0.039T, respectively. The solid lines represent fit results obtained using eq. 3.3. The calibration was performed at 600nm, while the fill fraction was $\Phi = 3.60 \times 10^{-4}$.

magnitude of the applied magnetic field. The minimum corresponds to the p-direction, the s-direction is perpendicular to it. The residue function R is symmetric with respect to the minimum, while the value of R increases with rising magnetic flux density. To obtain more quantitative information, we fitted the data in fig. 3.4 using eq. 3.3. The fitted curves are represented by the solid lines in fig. 3.4. The resulting fit parameters are summarized in table 3.1. The attenuation factor η does not depend on the applied magnetic field, as is to be expected for an experimentally defined quantity.

Table 3.1: Fit parameters corresponding to the solid lines in fig. 3.4, obtained using the residue fit function in eq. 3.3. Additionally, the values for birefringence and dichroism, obtained using eqs. 3.8, are given.

B (T)	η	$\tan(\Psi)$	Δ ($^\circ$)	δn	δk
0.014	0.992	0.985	16.18	2.70×10^{-6}	1.44×10^{-7}
0.025	0.992	0.944	32.23	5.37×10^{-6}	5.50×10^{-7}
0.039	0.992	0.911	46.44	7.74×10^{-6}	8.90×10^{-7}

The quantities $\tan(\Psi)$ and Δ determine the shape of the residue curve and exhibit a considerable variation with the applied magnetic flux density B . Details on the quantitative interpretation of $\tan(\Psi)$ and Δ in terms of linear magneto-optical properties will be discussed in the following section.

3.3.2 Linear birefringence and dichroism

To extract the linear birefringence and dichroism from our ellipsometry parameters $\tan(\Psi)$ and Δ in eq. 3.2, we first consider the linearly polarized incident light, propagating along the z -direction, to be described by [32]

$$E_{p,s}(z, t) = E_{p,s}^0 \exp\left(i\frac{2\pi}{\lambda}\tilde{n}z\right) \exp(-i\omega t) \quad (3.4)$$

in which p and s indicate the polarization directions, $E_{p,s}^0$ is the amplitude of the incident wave, $\tilde{n} = n + ik$ the complex refractive index, λ the wavelength in vacuum, and ω the angular frequency. As already described above, upon applying a magnetic field perpendicular to the direction of light propagation, the optical system, consisting of the cuvette filled with ferrofluid, becomes uniaxially anisotropic. The extraordinary direction is parallel, while the ordinary directions are perpendicular to the magnetic field. As a result of the calibration described in the previous section, the extraordinary and ordinary directions correspond directly to the p- and s-directions. The Jones matrix describing the transmission characteristics of such an anisotropic medium, also referred to as a linearly dichroic retarder [30], is given by

$$\begin{pmatrix} E'_p \\ E'_s \end{pmatrix} = \begin{pmatrix} \exp\left(i\frac{2\pi}{\lambda}\tilde{n}_{\text{ex}}d\right) & 0 \\ 0 & \exp\left(i\frac{2\pi}{\lambda}\tilde{n}_{\text{or}}d\right) \end{pmatrix} \begin{pmatrix} E_p \\ E_s \end{pmatrix} \quad (3.5)$$

where $E_{p,s}$ and $E'_{p,s}$ represent the polarization states of the incident and transmitted light, respectively. The complex refractive indices for the two anisotropy axes are represented by \tilde{n}_{ex} and \tilde{n}_{or} , and d is the optical path length, i.e. the internal thickness of the cuvette. In fact, the diagonal terms of the Jones matrix in eq. 3.5 are identical to the transmission coefficients $t_{p,s}$ in eq. 3.2 since

$$t_p = \frac{E'_p}{E_p} = \exp\left(i\frac{2\pi}{\lambda}n_{\text{ex}}d\right) \cdot \exp\left(-\frac{2\pi}{\lambda}k_{\text{ex}}d\right) \quad (3.6a)$$

$$t_s = \frac{E'_s}{E_s} = \exp\left(i\frac{2\pi}{\lambda}n_{\text{or}}d\right) \cdot \exp\left(-\frac{2\pi}{\lambda}k_{\text{or}}d\right) \quad (3.6b)$$

Structural anisotropy in a material generally gives rise to anisotropic optical properties. Linear birefringence and dichroism are related to differences in the real and imaginary parts of the complex refractive index for different directions, i.e. polarization states, in a material. In our case of a ferrofluid in an external magnetic field, the linear birefringence and dichroism are given by

$$\delta n = n_{\text{ex}} - n_{\text{or}} \quad (3.7\text{a})$$

$$\delta k = k_{\text{ex}} - k_{\text{or}} \quad (3.7\text{b})$$

in which n_{ex} (n_{or}) and k_{ex} (k_{or}) are the real and imaginary parts of the complex refractive index in the extraordinary (ordinary) directions. Inserting eqs. 3.6 into the complex reflection coefficient ρ (eq. 3.2), and using eqs. 3.7, we obtain simple relations between the ellipsometry parameters $\tan(\Psi)$ and Δ :

$$\delta n = \frac{\Delta \cdot \lambda}{2\pi \cdot d} \quad (3.8\text{a})$$

$$\delta k = -\frac{\ln(\tan(\Psi)) \cdot \lambda}{2\pi \cdot d} \quad (3.8\text{b})$$

Using these expressions, the linear magneto-optical properties can be readily derived from the experimentally determined ellipsometry parameters. For the Ψ and Δ values obtained from fig. 3.4, the birefringence and dichroism values, calculated using eqs. 3.8, are given in table 3.1.

3.3.3 Experimental results

In one of the previous sections, we determined the values of Ψ and Δ from the residue calibration curves. It enables determination of the linear magneto-optical properties through eqs. 3.8, but this procedure is quite elaborate and thus relatively slow. To determine birefringence and dichroism spectra, the analyzer angle was set to 45° . This is the most logical choice since initially, before applying a field, the system is isotropic and t_p is equal to t_s , i.e. the components parallel and perpendicular to the magnetic field are equal.

In fig. 3.5 the birefringence δn and dichroism δk are plotted as a function of wavelength for three values of the applied magnetic field. Below approximately 500nm the optical absorption in the ferrofluid becomes so large that accurate measurements can not be performed using the present combination of our Xe lamp and a relatively thick cuvette with an optical path length of 1cm. As is well-known, for increasing magnetic flux densities the bire-

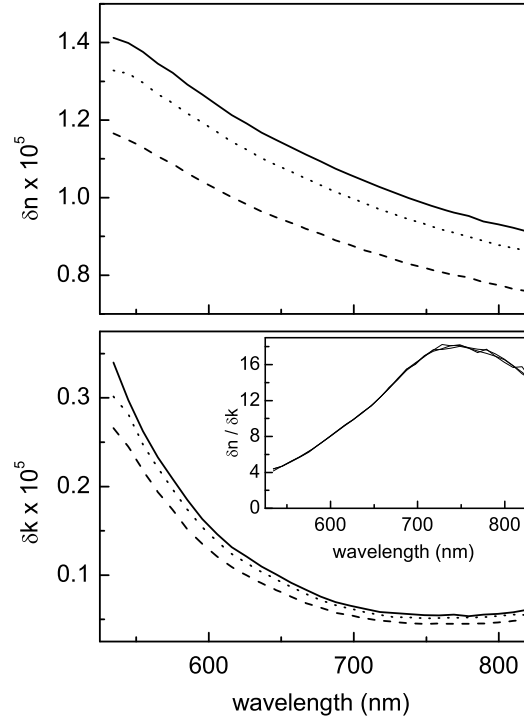


Figure 3.5: Birefringence δn and dichroism δk as a function of wavelength for different strengths of the applied magnetic field. The dashed, dotted and solid lines correspond to magnetic flux densities of 0.17T, 0.32T and 0.45T, respectively. The inset shows the wavelength dependence of the ratio $\delta n/\delta k$. The fill fraction amounted to $\Phi = 2.18 \times 10^{-4}$.

fringence and dichroism both become larger. Furthermore, the birefringence shows a continuous decrease toward longer wavelengths, while the dichroism exhibits a minimum near 750nm. This is very similar to the UV-VIS absorbance curve in fig. 3.3. In fact, from the absorbance data the imaginary part of the dielectric function k can be determined. We find that for the magnetic field strengths considered in this work, the maximum value of the ratio $\delta k/k$ amounts to approximately 7%. Also the wavelength-dependent ratio of birefringence and dichroism $\delta n/\delta k$ is plotted. This ratio increases from a value of 4 on the short-wavelength side, to reach a maximum of 18 at approximately 750nm, followed by a decline toward even longer wavelengths.

To further investigate the field dependence of the linear magneto-optical properties, in fig. 3.6 the birefringence and dichroism are plotted as a func-

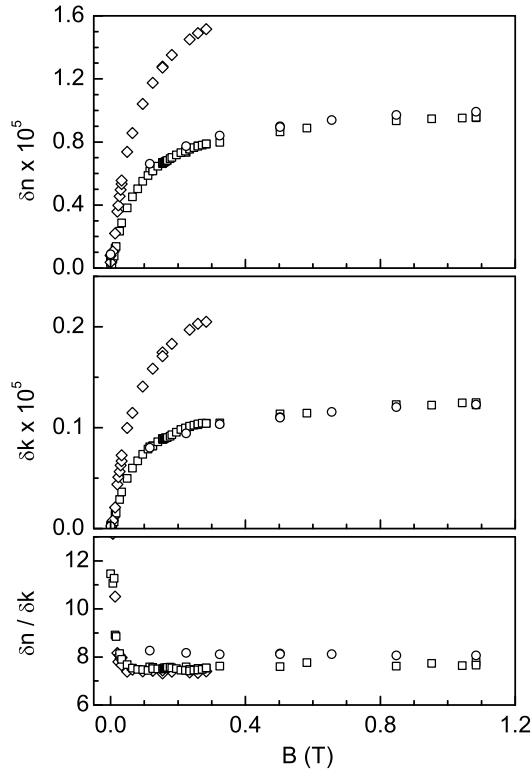


Figure 3.6: Birefringence δn and dichroism δk as a function of magnetic flux density for different concentrations of ferrofluid. The fill fractions amounted to $\Phi = 1.56 \times 10^{-4}$ and $\Phi = 3.12 \times 10^{-4}$ (squares and diamonds, respectively). For the larger concentration ($\Phi = 1.56 \times 10^{-3}$, circles), the values of δn and δk were divided by 10. Also, to circumvent the significantly larger optical absorption at these high concentrations, a cuvette with an optical path length of 1mm was used. The bottom panel shows the field-dependence of the ratio $\delta n/\delta k$. All measurements were performed at a wavelength of 600nm.

tion of the magnetic flux density for various concentrations at a wavelength of 600nm. For the highest concentration a thinner cuvette (1mm optical path length) was used to ensure sufficient intensity on the detector side. As is evident from the data in fig. 3.6, the birefringence and dichroism both scale linearly with concentration over the entire concentration range and also at all values of the field strength. For low fields both magneto-optical quantities δn and δk increase rapidly with the applied magnetic field. The

frequently observed quadratic dependence on the applied field was not found in our results. Apparently, we did not go down to sufficiently low magnetic fields. For fields exceeding approximately 0.3T, birefringence and dichroism approach their saturation value, which depend linearly on the concentration of magnetic nanoparticles in suspension.

In the bottom panel of fig. 3.6, the ratio of δn and δk is shown to be independent of the magnetic field, except for very low flux densities ($< 0.1\text{T}$). The constant ratio $\delta n/\delta k \approx 8$ is in agreement with the value in the inset fig. 3.5. For low flux densities, a strong increase is observed. This distinct rise may be attributed to particles of different sizes contributing to the magneto-optical properties. At low fields, only the larger particles (with a large magnetization) are assumed to contribute to the magneto-optical effects, while for larger fields also the smaller particles (with smaller magnetization) are responsible for the induced birefringence and dichroism. In case the contribution of small particles to δn and δk is different, a deviation can be envisaged.

In the ideal approximation of diluted suspensions, assuming there are no particle-particle interactions and in the absence of polydispersity, the variation of magneto-optical properties with the applied magnetic field strength is generally described by the second Langevin function [21, 22]. For the birefringence, it is given by [19]

$$\delta n(H, d_0, s) = \delta n_s \frac{\int_0^\infty d^3 \left(1 - \frac{3L(\xi(d,H))}{\xi(d,H)}\right) f(d, d_0, s) dd}{\int_0^\infty d^3 f(d, d_0, s) dd} \quad (3.9)$$

where $L(\xi(d, H)) = \coth(\xi) - 1/\xi$ represents the well-known Langevin function describing paramagnetic behavior, with $\xi = \mu_0 m(d)H/k_B T$, μ_0 the permeability of vacuum, $m(d)$ the diameter-dependent magnetic moment of the particle, $H = B/\mu_0$ the strength of the applied magnetic field, k_B the Boltzmann constant and T the absolute temperature. The log-normal size-distribution f , given by eq. 3.1, depends on the parameters d_0 and s . For a perfectly monodisperse suspension, the log-normal distribution is a delta-function, and eq. 3.9 reduces to

$$\delta n = \delta n_s \left(1 - \frac{3L(\xi)}{\xi}\right) \quad (3.10)$$

A similar expression holds for the dichroism δk .

From eq. 3.10, it follows that the saturation values for the birefringence δn_s and dichroism δk_s can be obtained by plotting δn and δk as a function

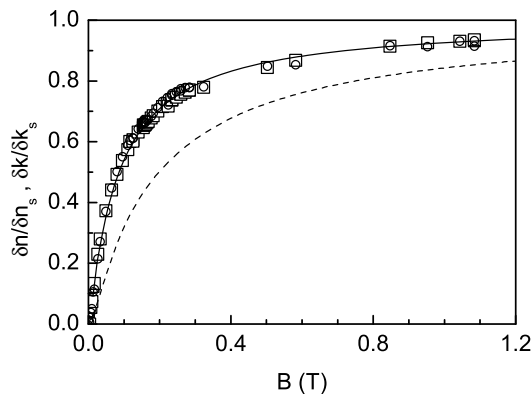


Figure 3.7: Normalised birefringence $\delta n/\delta n_s$ (squares) and dichroism $\delta k/\delta k_s$ (circles) as a function of magnetic flux density. The lines correspond to calculations of the field dependence using a standard deviation $s = 0.31$ of the log-normal distribution (eq. 3.1) and average diameters $d_0 = 7.4\text{nm}$ and $d_0 = 5.6\text{nm}$ (solid and dashed lines, respectively.)

$1/H$. In the high field limit, a linear relation is indeed obtained. For a fill fraction $\Phi = 1.56 \times 10^{-4}$ (squares, in fig. 3.6), we find that $\delta n_s = 1.036 \times 10^{-5}$ and $\delta k_s = 1.34 \times 10^{-6}$. In fig. 3.7 the normalized birefringence and dichroism are plotted. Within experimental error both exhibit the same dependence on the magnetic flux density. The normalized linear magneto-optical parameters are also compared to calculations using eq. 3.9, taking into account the log-normal size distribution, i.e. the polydispersity [21], as shown in fig. 3.2. With the standard deviation $s = 0.31$ determined from the analysis of TEM images (such as fig. 3.1), the normalized birefringence (or dichroism, both exhibit the same dependence on applied field B) is plotted for average diameters of $d_0 = 5.6\text{nm}$ and $d_0 = 7.4\text{nm}$. The calculation based on the latter value shows a remarkably good agreement with the experimental results. This indicates the importance of the anisotropy, i.e. the long axis of the magnetite particles, in the contribution to the magneto-optical behavior of our ferrofluids.

3.3.4 Comparison with other work and established theories

Spectral dependence

In most work on magneto-optical properties of ferrofluids in general, which has been published during the past few decades, a strong emphasis is on

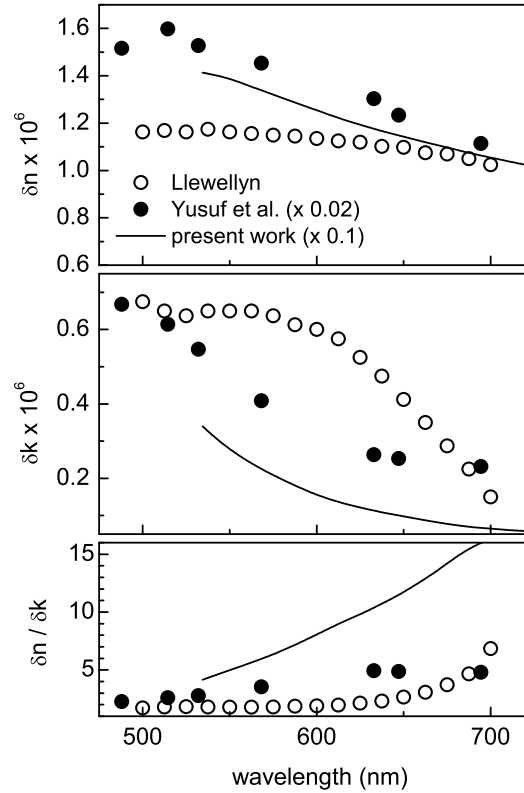


Figure 3.8: Wavelength-dependent magneto-optical birefringence δn and dichroism δk of fig. 3.5 (attenuated by a factor 10), compared to literature data presented by Llewellyn (open symbols) [14] and Yusuf et al. (closed symbols, attenuated by a factor 50) [33] for Fe_3O_4 ferrofluids. The fill fraction for the Yusuf-data amounts to $\Phi = 5.48 \times 10^{-4}$, while this value is not given in the Llewellyn-work. Only the data in the range of 500–700nm are shown. The bottom panel shows the ratio $\delta n/\delta k$ as a function of wavelength.

the magnetic field-dependent optical properties. A few exceptions are the papers by Llewellyn [14] and Yusuf et al. [33]. In the former, the wavelength-dependent birefringence and dichroism of ferrofluids, consisting of (i) Fe_3O_4 in diester and (ii) Co in toluene, are presented in the range of 300–700nm. The latter paper describes concentration and wavelength dependence of the magneto-optical properties of a magnetite ferrofluid. The results from these publications are shown in fig. 3.8 in the spectral range of 500–700nm.

Details on the suspension used by Llewellyn, such as particle size and fill fraction, are not provided. The experiments were performed at a relatively low magnetic flux of 0.075T, which might explain the considerably lower values of δn and δk in their work as compared to our results in fig. 3.5. The fill fraction for the results by Yusuf et al. amounts to $\Phi = 5.48 \times 10^{-4}$. In their case, the saturation values at 0.5T were used for comparison.

Despite the difference of approximately one order of magnitude in the absolute values of birefringence and dichroism, most likely related to different concentrations and/or a lower applied field, there are a number of similarities between the various sets of data in the range of 500 – 700nm. The decrease of the birefringence and the dichroism with increasing wavelength is observed in all experiments. In fig. 3.5, considering the lowest applied field, the decrease of δn and δk amount to approximately 25% and 80%, respectively, while the two magneto-optical quantities in the Llewellyn-data in fig. 3.8 decrease by approximately 15% and 80%. Similar changes of δn and δk (25%, resp. 65%) over this wavelength range are also found by Yusuf et al. Accordingly, the ratio $\delta n/\delta k$ of birefringence and dichroism exhibits a 2.5-4-fold increase in both sets of literature data.

However, the spectral features, i.e. the ‘shape’ of the changes with wavelength are considerably different. One problem is that the bulk dielectric function of Fe_3O_4 is not well-documented in the literature, most likely owing to the difficulty of obtaining an accurate result. Full or partial oxidation of Fe_3O_4 to Fe_2O_3 with prolonged exposure to air will give rise to a mixing of contributions to the measured optical response. Additionally, it is well-known from other work on metallic nanoparticles [34] that the optical response of particles with dimensions in the low-nanometer range may be substantially different from their bulk counterparts. This may also be the case here. For the calculations presented in the next part of this section, we will use the bulk dielectric function as given by Schlegel et al. [35]. Finally, the surrounding medium also influences the spectral characteristics. Llewellyn used diester as solvent, while Yusuf et al. dispersed the particles in Isopar-M liquid. For the experiments presented in this work cyclohexane was used.

Field strength dependence

In contrast to the spectral characteristics of ferrofluid birefringence and dichroism a large amount of work has been done on the magnetic flux dependence [9–27]. For low fields, the well-known quadratic increase of magneto-optical properties has been reported frequently. Also, the high-field

regime has been measured and analyzed extensively. Our results presented in figs. 3.6 and 3.7 are part of the last category, since we did not focus on the low-field limit.

The optical anisotropy of ferrofluids in the presence of an applied magnetic field has often been considered to be due to shape anisotropy of magnetic particles or particle-clusters. Differences between the various models often are due to the assumption of either magnetically induced or preexisting agglomerates of particles. The first theoretical description of this shape anisotropy was provided by Scholten [11], based primarily on the pioneering work of Skibin [9]. More recently, Rasa presented more general formula's for the magneto-optical properties [21, 22]. For the fill fractions Φ (i.e. nanoparticle concentrations) considered in this work, the expressions by Rasa yield identical results as compared to the Scholten-work. The extraordinary and ordinary components ε_{ex} and ε_{or} of the ferrofluid dielectric function parallel and perpendicular to the applied magnetic field are derived by determining the dielectric tensor

$$\varepsilon_{\text{ex}} = \frac{(1 - \Phi)\varepsilon_1 + \Phi(\varepsilon_{\parallel} + 2(\varepsilon_{\perp} - \varepsilon_{\parallel})(L(\xi)/\xi))}{(1 - \Phi) + \frac{\Phi}{\varepsilon_2}(\varepsilon_{\parallel} + 2(\varepsilon_{\perp} - \varepsilon_{\parallel})(L(\xi)/\xi))} \quad (3.11a)$$

$$\varepsilon_{\text{or}} = \frac{(1 - \Phi)\varepsilon_1 + \Phi(\varepsilon_{\perp} + (\varepsilon_{\parallel} - \varepsilon_{\perp})(L(\xi)/\xi))}{(1 - \Phi) + \frac{\Phi}{\varepsilon_2}(\varepsilon_{\perp} + (\varepsilon_{\parallel} - \varepsilon_{\perp})(L(\xi)/\xi))} \quad (3.11b)$$

in which ε_1 is the real dielectric function of the solvent (cyclohexane in our case), ε_2 is the complex dielectric function of magnetite and

$$\varepsilon_{\perp} = \frac{\varepsilon_1 \varepsilon_2}{\varepsilon_1 + (\varepsilon_2 - \varepsilon_1)n_{\perp}} \quad (3.12a)$$

$$\varepsilon_{\parallel} = \frac{\varepsilon_1 \varepsilon_2}{\varepsilon_1 + (\varepsilon_2 - \varepsilon_1)n_{\parallel}} \quad (3.12b)$$

The depolarization factors n_{\parallel} and n_{\perp} for prolate ellipsoidal particles parallel and perpendicular to their long axis are given by

$$n_{\parallel} = \frac{1 - e^2}{e^2} \left(\frac{1}{2e} \ln \left(\frac{1 + e}{1 - e} \right) - 1 \right) \quad (3.13a)$$

$$n_{\perp} = \frac{1 - n_{\parallel}}{2} \quad (3.13b)$$

with the eccentricity $e = \sqrt{1 - \eta^2}$ defined by the ratio η of the short and long diameters. For the particles considered here, $\eta = 5.6\text{nm}/7.4\text{nm} = 0.76$, $e = 0.65$, yielding $n_{\parallel} = 0.26$ and $n_{\perp} = 0.37$.

A few years after the publication by Scholten [11], Taketomi presented a study of the magneto-optical effects in highly concentrated thin films of ferrite fluids [15]. The anomalous results observed in the experiments were attributed to rod-like chain formation and alignment of the ferrite particulate rods in the applied field. On the basis of these results, a dielectric tensor was derived, which also yields expressions for the parallel and perpendicular components of the dielectric functions

$$\varepsilon_{\text{ex}} = \varepsilon_1 + \alpha\Phi \frac{\varepsilon_2 - \varepsilon_1}{\varepsilon_2 + \varepsilon_1} \left(\varepsilon_2 + \varepsilon_1 - 2\varepsilon_2 \frac{L(\xi)}{\xi} \right) \quad (3.14a)$$

$$\varepsilon_{\text{or}} = \varepsilon_1 + \alpha\Phi \frac{\varepsilon_2 - \varepsilon_1}{\varepsilon_2 + \varepsilon_1} \left(\varepsilon_2 + \varepsilon_1 \frac{L(\xi)}{\xi} \right) \quad (3.14b)$$

where the dielectric functions ε_1 and ε_2 are identical to those used in the

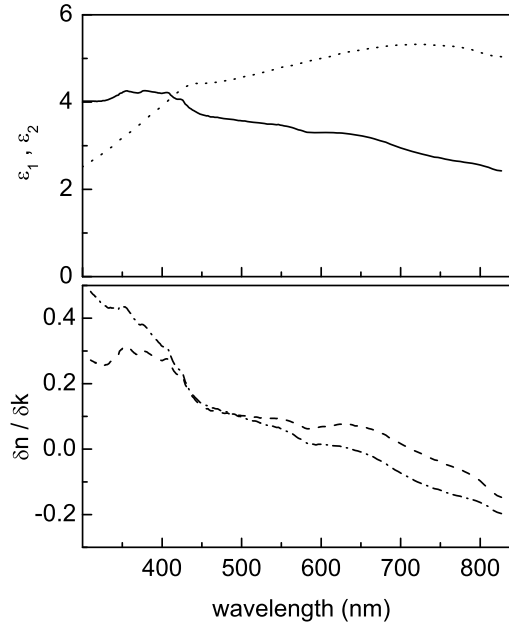


Figure 3.9: (top) Wavelength-dependent real (solid line) and imaginary (dotted line) parts of the dielectric function of bulk Fe_3O_4 as taken from the work by Schlegel et al. [35]. (bottom) Ratio $\delta n / \delta k$ of birefringence δn and dichroism δk as a function wavelength, calculated using the expressions given by Rasa and Taketomi (dashed and dash-dotted lines, respectively) [15, 21].

Rasa-expressions and $\alpha < 1$ is a constant of order unity representing the fraction of magnetic material, i.e. magnetite in our case, in the cylindrical rod-like aggregates. The expressions derived by Rasa [21] reduce to eqs. 3.14 by setting the denominator in eqs. 3.11 equal to 1, inserting the depolarization factors for an infinitely long cylinder ($n_{\parallel} = 0$ and $n_{\perp} = 0.5$) and replacing the magnetic moment of a particle by that of a rod-like aggregate. Despite the considerably lower concentrations in the ferrofluid used in this work, we also compare our experimental results to calculations using this model.

Using the anisotropic dielectric functions as derived by Rasa and Taketomi, the calculation of the linear magneto-optical properties is straightforward. Since $n_{\text{ex}} = \text{Re}(\sqrt{\varepsilon_{\text{ex}}})$, $n_{\text{or}} = \text{Re}(\sqrt{\varepsilon_{\text{or}}})$, $k_{\text{ex}} = \text{Im}(\sqrt{\varepsilon_{\text{ex}}})$, and $k_{\text{or}} = \text{Im}(\sqrt{\varepsilon_{\text{or}}})$, eqs. 3.8 immediately yield the linear birefringence and linear dichroism.

Before turning our attention to the field strength-dependent magneto-optical properties, the equations by Rasa and Taketomi (eqs. 3.11 and 3.14) enable determination of the ratio $\delta n/\delta k$ as a function of wavelength, using the dielectric function of bulk magnetite. The ratio does not exhibit any dependency on the applied magnetic field. In fig. 3.9 the bulk Fe_3O_4 dielectric function is shown in the top panel. In the same figure, the ratio of birefringence and dichroism are shown as calculated from eqs. 3.11 derived by Rasa and eqs. 3.14 by Taketomi using the bulk dielectric function. Despite the similarity of the two calculated wavelength-dependent ratios, comparison of them to the experimental results in figs. 3.5 and 3.8 reveals enormous differences. Where all experiments exhibit a continuous increase of the ratio $\delta n/\delta k$ with wavelength, the calculated spectra show a cross-over from positive to negative values. But most obvious is the order of magnitude difference between measured and calculated spectral dependencies, which is most pronounced for the experimental results obtained in our work presented in this chapter. This marked deviation between experiment and theory is most likely due to the fact that the bulk dielectric function of magnetite can not be used for the Fe_3O_4 nanoparticles in the ferrofluids considered in all experiments, as already described in the previous section. Furthermore, the bulk dielectric function shown in the top panel of fig. 3.9 is also not even in qualitative agreement with the absorbance spectra depicted in fig. 3.3.

The size-dependence of the optical properties of nanoparticles as compared to that of bulk material, may also explain the strong increase of the ratio of birefringence and dichroism observed in our present work (fig. 3.6) for lower fields. At low applied fields only the large particles are influenced by the external applied field, while the smaller particles still are randomly

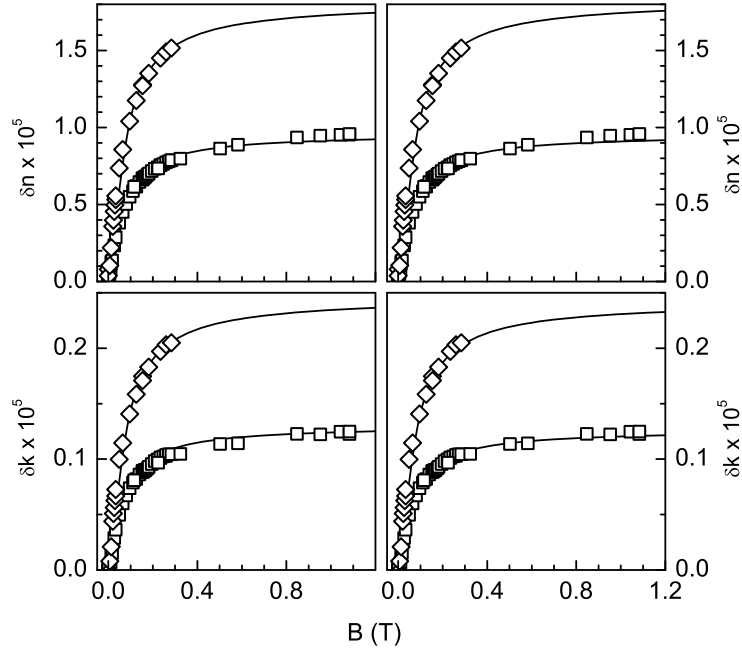


Figure 3.10: Comparison of experimentally determined birefringence δn (top) and dichroism δk (bottom) for fill fractions of $\Phi = 1.56 \times 10^{-4}$ and $\Phi = 3.12 \times 10^{-4}$ (squares and diamonds, respectively) to calculations using the Rasa eqs. 3.11 (left) and Taketomi eqs. 3.14 (right), as described in the text.

oriented in the ferrofluid. Upon increasing the field, the smaller particles, with different dielectric and/or magneto-optical properties, also start to contribute to the birefringence and dichroism.

Using the eqs. 3.11 and 3.14, we also calculated the magnetic field-dependent magneto-optical properties as shown in fig. 3.6. In these calculations we inserted the known fill fractions Φ of our ferrofluid samples, and the dielectric functions $\varepsilon_1 = 2.03$ and $\varepsilon_2 = 3.30 + 5.00i$ of cyclohexane and bulk magnetite, respectively, at a wavelength of 600nm. A very similar qualitative field-dependence is observed in calculations as compared to the experiments. But as with the spectral dependence of the magneto-optical properties, also the theoretical field-dependent birefringence and dichroism do not show quantitative agreement with the experiments.

As mentioned above, we ascribe these considerable discrepancies to the modified bulk dielectric function of magnetite for the nanoscale particles in

ferrofluids. To obtain an indication of this modification, required to achieve quantitative agreement, we used the Rasa and Taketomi models to fit the dielectric function for our nanoparticulate suspensions. To simplify the calculations, we do not take into account polydispersity here. The results are shown in fig. 3.10. Using the expressions of Rasa and the fill fractions $\Phi = 1.56 \times 10^{-4}$ and $\Phi = 3.12 \times 10^{-4}$, as indicated in fig. 3.6, very good quantitative agreement is obtained, as shown in the left panels of fig. 3.10, for an effective magnetite dielectric function $\varepsilon_2 = 4.5 + 0.23i$. The real part of this dielectric constant (at a wavelength of 600nm) is still of the same order of magnitude but 40% higher than the bulk value, but the imaginary part is considerably reduced by an order of magnitude. Similarly, the expressions of Taketomi also yield a good correspondence as shown in the right panels of fig. 3.10. In the latter case a dielectric function $\varepsilon_2 = 4.2 + 0.245i$ is obtained by fitting, very similar to that obtained from the Rasa model. However, as described above, the equations by Taketomi also contain a factor α representing the fraction of magnetite in the rod-like aggregates. A proper fit is found for $\alpha = 0.12$. This value indicates rather low magnetite quantities in the rod-like aggregates due to chain formation. Furthermore, it may also reflect that not all magnetite particles are aggregated. Large separations and thus small interactions between neighbouring magnetite particles in the chain-like aggregates suggest that chaining is not an issue in our experiments. This is in agreement with the low concentrations, i.e. fill fractions of our ferrofluid, as compared to those used by Taketomi [15].

Finally, the magnetic field-dependent experiments presented here for a wavelength of 600nm, can in principle be performed at all wavelengths. As such, it enables determination of the effective dielectric function at all photon energies and thus allows spectral characterization of magnetic nanoparticle suspensions. However, a precise determination of the dielectric function of Fe_3O_4 lies outside the scope of the present work.

3.4 Conclusions

In this chapter we have explored the versatility of spectroscopic ellipsometry in transmission mode to study magneto-optical properties of magnetite ferrofluids. Linear birefringence and linear dichroism are both obtained simultaneously from measured ellipsometric quantities Ψ and Δ as a function of applied magnetic fields up to 1.1T. We derive simple equations, which relate the magneto-optical properties to the experimentally obtained optical quantities. Since we are able to measure birefringence and dichroism

at the same time with high accuracy, and as a function of the wavelength of the light, we can compare our data to previous experimental work and also to theoretical models describing the magneto-optical characteristics of ferrofluids.

The spectral characteristics of the birefringence and dichroism are in line with previous experimental work. However, marked differences are observed which may be related to size distribution of the particles, the solvent in which they are suspended, the degree of oxidation of the magnetite particles and the effective dielectric function of the nanoparticles constituting the ferrofluids. Most pronounced is the large ratio of birefringence and dichroism in our results as compared to previous work. The magnetic field-dependent optical response is in qualitative agreement both with previous experimental work and also with theoretical models. The quantitative discrepancies between our experimental results and the theoretical models have been discussed in relation to a modified dielectric function of the magnetite nanoparticles in the ferrofluids.

References

- [1] Q. Majorana, C. R. Hebd. Acad. Sci. **135**, 159 (1902).
- [2] Q. Majorana, C. R. Hebd. Acad. Sci. **135**, 235 (1902).
- [3] A. Cotton and H. Mouton, C. R. Hebd. Acad. Sci. **141**, 317 (1905).
- [4] P. Berger, N. Adelman, K. Beckman, D. Campbell, A. Ellis, and G. Lisensky, J. Chem. Educ. **76**, 943 (1999).
- [5] D. Bica, L. Vékás, and M. Raşa, J. Magn. Magn. Mater. **252**, 10 (2002).
- [6] G. A. van Ewijk, G. J. Vroege, and A. P. Philipse, J. Magn. Magn. Mater. **201**, 31 (1999).
- [7] R. Massart, E. Dubois, V. Cabuil, and E. Hasmonay, J. Magn. Magn. Mater. **149**, 1 (1995).
- [8] M. Shinkai, J. Biosci. Bioeng. **94**, 606 (2002).
- [9] Y. N. Skibin, V. V. Chekanov, and Y. L. Raikher, Zh. Eksp. Teor. Fiz. **72**, 949 (1977).
- [10] H. W. Davies and J. P. Llewellyn, J. Phys. D: Appl. Phys. **12**, 311 (1979).
- [11] P. C. Scholten, IEEE Trans. Magn. **16**, 221 (1980).
- [12] H. W. Davies and J. P. Llewellyn, J. Phys. D: Appl. Phys. **13**, 2327 (1980).
- [13] P. C. Scholten, J. Phys. D: Appl. Phys. **13**, L231 (1980).
- [14] J. P. Llewellyn, J. Phys. D: Appl. Phys. **16**, 95 (1983).

- [15] S. Taketomi, Jpn. J. Appl. Phys. **22**, 1137 (1983).
- [16] J. J. M. Janssen and J. A. A. J. Perenboom, J. Magn. Magn. Mater. **81**, 14 (1989).
- [17] P. Daveze, H. Sahseh, and J. Monin, Meas. Sci. Technol. **7**, 157 (1996).
- [18] M. Xu and P. J. Ridler, J. Appl. Phys. **82**, 326 (1997).
- [19] E. Hasmonay, E. Dubois, J.-C. Bacri, R. Perzynski, Y. Raikher, and V. Stepanov, Eur. Phys. J. B **5**, 859 (1998).
- [20] H. E. Horng, C.-Y. Hong, H. C. Yang, I. J. Jang, S. Y. Yang, J. M. Wu, S. L. Lee, and F. C. Kuo, J. Magn. Magn. Mater. **201**, 215 (1999).
- [21] M. Raşa, J. Magn. Magn. Mater. **201**, 170 (1999).
- [22] M. Raşa, Eur. Phys. J. E **2**, 265 (2000).
- [23] E. Hasmonay, J. Depeyrot, M. H. Sousa, F. A. Tourinho, J.-C. Bacri, R. Perzynski, Y. L. Raikher, and I. Rosenman, J. Appl. Phys. **88**, 6628 (2000).
- [24] V. Buzmakov and A. F. Pshenichnikov, Colloid J. **63**, 305 (2001).
- [25] C. P. Pang, C. T. Hsieh, and J. T. Lue, J. Phys. D: Appl. Phys **36**, 1764 (2003).
- [26] A. F. Bakuzis, K. S. Neto, P. P. Gravina, L. C. Figueiredo, P. C. Morais, L. P. Silva, R. B. Azevedo, and O. Silva, Appl. Phys. Lett. **84**, 2355 (2004).
- [27] V. Socoliuc and D. Bica, J. Magn. Magn. Mater. **289**, 177 (2005).
- [28] R. J. Hunter, *Foundations of colloid science*, Oxford University Press, New York, 2001.
- [29] J. M. M. de Nijs, *Ellipsometry and the Ti/c-Si solid-state reactio*, PhD thesis, University of Twente, Enschede, The Netherlands, 1989.
- [30] R. M. A. Azzam and N. H. Bashara, *Ellipsometry and Polarized Light*, North Holland, Amsterdam, 1987.
- [31] J. M. M. de Nijs, A. H. M. Holtslag, A. Hoekstra, and A. van Silfhout, J. Opt. Soc. Am. A **5**, 1466 (1988).
- [32] H. G. Tompkins and W. A. McGahan, *Spectroscopic ellipsometry and reflectometry; A user's guide*, John Wiley and Sons, Inc., New York, 1999.
- [33] N. A. Yusuf, A. Ramadan, and H. Abu-Safia, J. Magn. Magn. Mater. **184**, 375 (1998).
- [34] U. Kreibig and M. Vollmer, *Optical properties of metal clusters*, Springer-Verlag, Berlin, 1995.
- [35] A. Schlegel, S. F. Alvarado, and P. Wachter, J. Phys. C: Solid State Phys. **12**, 1157 (1979).

Chapter 4

Finite element analysis of magnetic configurations: Application to magnetophoretic deposition

Abstract

The suitability for magnetophoretic deposition of various (electro-)magnet geometries is studied using finite element methods. The magnetic field distribution in the air gap between the poles of a conventional axisymmetric DC-electromagnet is calculated. First, replacement of one of the originally flat pole shoes by a (truncated) conical one, generates a well-defined magnetic field gradient between the two poles. Also, the flux converging in the vicinity of an isolated bar-magnet or a solenoid with an iron core is discussed. The field gradients are sufficiently strong to compete with Brownian motion and in principle enable magnetophoretic deposition of nanocolloidal particles.

4.1 Introduction

Before the nineteenth century, the only magnetism known was that of natural magnets. The first step in the world of electromagnetism was made accidentally in 1820 by Ørsted, who observed that the electric current affects a compass needle [1], and by Ampère, who discovered that wires carrying current exert a force on each other [2]. Five years later Sturgeon, a British electrician, invented the electromagnet [3]. The tunability of the magnetic fields generated by these electromagnets enabled the development of many different types of devices and machines, such as switches, electric bells and metal-lifting cranes. Also it provided a foundation for electronic communication, when in 1830 Henry used the principle of electromagnetism to develop the first electric telegraph [4].

Nowadays, tunable magnetic configurations include single solenoids, combinations of two (iron)core solenoids (also referred to as conventional electromagnets) and also superconducting magnets. The maximum magnetic field strengths, which can presently be achieved, amount to approximately 75T [5]. The requirements posed by the magnetic fields, in terms of field strength, sample volume, field uniformity and also the frequency (DC or AC) dictate which of the aforementioned methods is used in different geometries.

Homogeneous magnetic fields are generally used to measure sample magnetization and magneto-optical properties, such as the Kerr effect, the magnetic linear birefringence and dichroism. In the case of colloidal magnetic nanoparticles, homogeneous fields can be used to induce particle alignment and achieve chaining due to the interaction of the dipole moments [6–8]. With inhomogeneous magnetic fields, the gradients can be used to perform Stern-Gerlach deflection experiments [9–11] or to control the transport of magnetic particles (magnetophoresis), for example in separation technology [12–14] and in bio-medical applications [15–19].

Organization of magnetic nanoparticles from solution onto a substrate, and the formation of mono- or multi- layers has attracted considerable interest recently [7, 20–22]. During self-assembly of nanoparticles by drop-casting of the nanocolloidal suspension on a substrate, drying effects generally give rise to isotropic ordered or disordered arrays. Application of a homogeneous magnetic field during this drying procedure has been shown to yield highly anisotropic structures [8, 20, 23] (see also chapter 1). An inhomogeneous magnetic field does not only cause alignment of the nanoparticle magnetic moments with the field, but also enables (controlled) movement of nanoparticles to regions of higher flux density. When the particles are driven toward an interface where they are collected, we refer to this as magnetophoretic

deposition.

The force on a nanocolloidal particle due to a magnetic field gradient in the x -direction is given by:

$$\mathbf{F}_x = \frac{\pi M_{sb} d^3 \mu_0}{6} \frac{\delta \mathbf{H}}{\delta x} \quad (4.1)$$

where d is the particle diameter, M_{sb} is the bulk saturation magnetization of particle material, μ_0 is the permeability of vacuum and \mathbf{H} is the magnetic field intensity. If we consider a spherical magnetite (Fe_3O_4) particle of 10nm diameter, in a magnetic field gradient of 10mT/mm, the force \mathbf{F}_x amounts to 2.5×10^{-18} N. The magnetic energy, i.e. the work involved in moving a magnetic nanoparticle over a certain distance x in the solvent, is expressed by [24]:

$$W = \mathbf{F} \cdot \mathbf{x} \quad (4.2)$$

For a typical, experimental distance of 1cm, this energy amounts to approximately $6 \cdot k_B T_r$. If we consider the energy associated with Brownian motion to be in the order of $k_B T_r$ (see also chapter 1), we can conclude that the force induced by the typical gradients of the magnetic field in the order of 10mT/mm, is sufficiently large to compete with Brownian motion.

When we neglect Brownian motion and only consider the drag friction force for a moving particle in a liquid, given by:

$$\mathbf{F}_{\text{drag}} = -3\pi d \eta \mathbf{v} \quad (4.3)$$

where $\eta = 1.02 \cdot 10^{-3}$ Pa.s is the viscosity of the solvent is the relative particle velocity with respect to the solvent, the time required for one single magnetite particle of 10nm diameter to travel 1mm in a field gradient of 100mT/mm will amount to approximately 1h. Since this time is inversely proportional to the magnetic field gradient, a higher gradient will give rise to shorter times.

In this chapter we will focus on finding suitable (electro-)magnetic geometries to perform magnetophoretic deposition measurements. Because it is not straightforward and in many cases impossible to obtain analytical expressions, which describe the field distribution for various electromagnet geometries, we resort to basic finite element predictions. These have the advantage that they are accurate and can be obtained relatively fast. Additionally, we show that the field gradients are sufficiently large to effectively compete with Brownian motion and that magnetophoretic deposition can, in principle, be achieved.

4.2 Finite element calculations

The finite element calculations described in this chapter are performed using Finite Element Method Magnetics (FEMM), version 4 [25]. This is a Windows-based package, which enables solving two-dimensional planar and axisymmetric magnetostatic problems. There are three parts in this package. The interactive shell (*femm.exe*) consists of a Multiple Document Interface pre-processor, which enables drawing of the desired configuration, as well as definition of material properties and boundary conditions. A post-processor allows the user to visualize the field solution, inspect the field at arbitrary points, evaluate line integrals and plot various quantities along any contour. The mesh generator (*triangle.exe*) breaks the solution region down into a large number of triangles. It is a vital part of the finite element process done by the solver (*fkern.exe*), which solves the relevant Maxwell's equations for the set of data files that describe the problem and obtain the values for the desired field throughout the solution domain. The powerful scripting language integrated with the program, Lua, allows to create batch runs, to describe geometries parametrically and to perform optimizations.

In magnetostatic problems, as in the case with DC electromagnets, the fields are time-invariant. In this case only two Maxwell's equation are involved. The field intensity (\mathbf{H}) and flux density (\mathbf{B}) must obey:

$$\operatorname{curl}\mathbf{H} = \mathbf{J} \quad (4.4)$$

$$\operatorname{div}\mathbf{B} = 0 \quad (4.5)$$

while the constitutive relationship between \mathbf{B} and \mathbf{H} for each material must hold:

$$\mathbf{B} = \mu\mathbf{H} \quad (4.6)$$

For nonlinear materials, such as saturating iron or AlNiCo magnets, the permeability μ is a function of \mathbf{B} :

$$\mu = \frac{\mathbf{B}}{\mathbf{H}(\mathbf{B})} \quad (4.7)$$

FEMM resolves the field that satisfies eqs. 4.4– 4.6, using a magnetic vector potential (\mathbf{A}) approach, defining the flux density in terms of \mathbf{A} :

$$\mathbf{B} = \operatorname{curl}\mathbf{A} \quad (4.8)$$

Because this definition of \mathbf{B} always satisfies eq. 4.5, FEMM will retain only

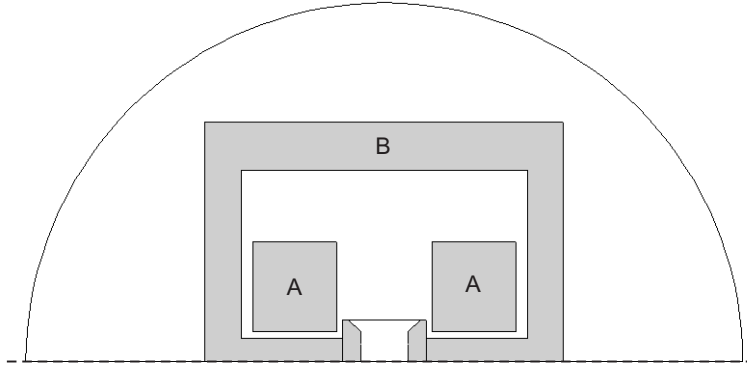


Figure 4.1: 2-D axisymmetric representation of an electromagnet. The gray squares (A) are cross-sections of the copper coils, the other gray area (B) represents the magnetic circuit and the white space is air. The dashed line represents the symmetry-axis of the magnet configuration. The semi-circle (radius of 30cm) is the region, in which the finite element solver defines a mesh and determines a solution.

the rewritten form of eq. 4.4:

$$\text{curl}\left(\frac{1}{\mu(\mathbf{B})} \text{curl}\mathbf{A}\right) = \mathbf{J} \quad (4.9)$$

In this present situation, a two-dimensional axisymmetric case, two of the three components of the vector potential vanish, and only the component in the 'out of page' direction is non-zero. This vector potential approach has the advantage that all the conditions to be satisfied are combined into a single equation, an elliptic partial differential equation. When the solution for \mathbf{A} is found, \mathbf{B} and \mathbf{H} can be easily deduced by differentiation of \mathbf{A} .

Our initial configuration is depicted in fig. 4.1. This is a two-dimensional view of an electromagnet with connected poles. Each coil has an inner diameter of 5cm, an outer diameter of 20cm, an axial length of 7cm, and is constructed from 1000 turns of 2mm copper wire. The steady currents, which flow through the wires, are in the 1 – 15A range. The material of the cores is a soft magnetic iron-based material, which is preferred over pure iron, since it has a much lower remanent value. The poles are slightly tapered and connected for achieving higher magnetic fields. The poles can be removed and replaced with geometrically modified poles. All the tapered surfaces are cones with a half-angle of 45°.

4.3 Homogeneous magnetic fields

To generate an ideal homogeneous magnetic field, devoid of any field gradients in the air gap between the poles of an electromagnet, two conditions should be fulfilled: (i) the poles should be infinitely large and (ii) the distance between them must be very small. In practice this can not be realized. The air gap should be sufficiently large to accommodate the sample and sample holder.

Generally, conventional electromagnets are used to produce magnetic fields up to 1 – 2T. This is achieved by concentration of the magnetic flux, produced by a coil, into a small space using a magnetic circuit. Taking the length of the magnetic circuit l_m , the total number of windings N in the coils, the electric current I , the field strength H_a in the air gap with a length l_a , can be extracted analytically from [26]:

$$H_m l_m + H_a l_a = NI \quad (4.10)$$

When the permeability of the magnetic circuit is sufficiently large, in our case $\mu(0T) \cong 2000\mu_0$, the field in the magnetic circuit H_m can be neglected, yielding a simple linear relationship between the field in the gap and the magnetomotive force NI . In fig. 4.2(a) this relation for our geometry, with $l_a = 40\text{mm}$, $N = 2000$ is plotted. Also shown is the flux density as a function of the current, as determined from FEMM calculations. The linear relationship only holds for currents below approximately 4A. For higher values of the magnetic field, the permeability $\mu = \mathbf{B}/\mathbf{H}(\mathbf{B})$ (eq. 4.7) of the magnetic circuit decreases, and the field H_m can no longer be neglected. Also, it can be seen from eq. 4.10 that for a smaller air gap, the magnetic field will increase. To make the maximum field as high as possible, the poles should be tapered in such way that the tapered surface is a cone with a half-angle of 54.7° [26]. In our situation with tapered surface angle of 45° slightly smaller fields are obtained.

In fig. 4.2(b) the magnetic flux density across the gap between the pole shoes, calculated using FEMM, is compared with the analytical value obtained using eq. 4.10. Near the surface of the pole shoes the flux densities are identical. The results obtained with FEMM exhibit a decrease of approximately 5% in the middle of the gap, which is slightly dependent on the current. This decline reflects a slight field inhomogeneity, which originates from the finite dimensions of the magnet configuration.

The magnetic flux density obtained from FEMM, is plotted in fig. 4.3(a). In fact, this is a geometry very similar to the one used for the magneto-

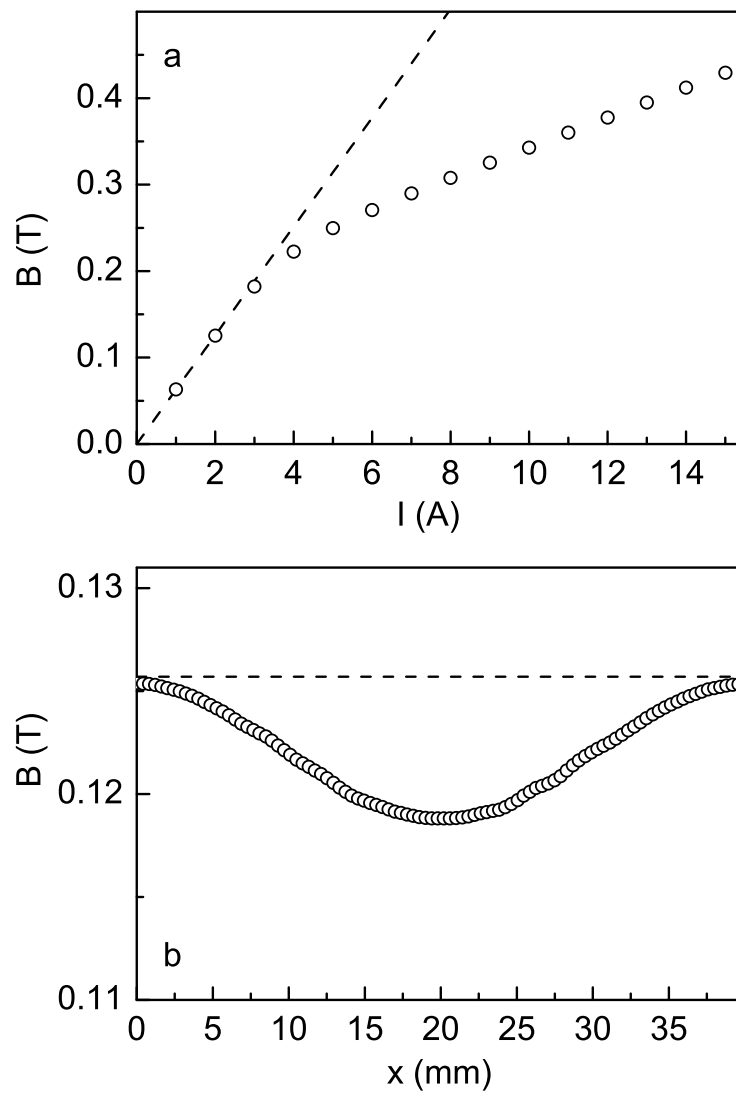


Figure 4.2: (a) The magnetic flux density, as determined by FEMM, close to the center of the magnet pole as a function of the applied current (open circles); the dashed line is the linear relationship, given by eq. 4.10. (b) Distance dependent magnetic flux density plot between the poles along the magnet axis, calculated using FEMM (open circles) and the analytical solution using eq. 4.10 (dashed line). In both cases a current of 2A was used.

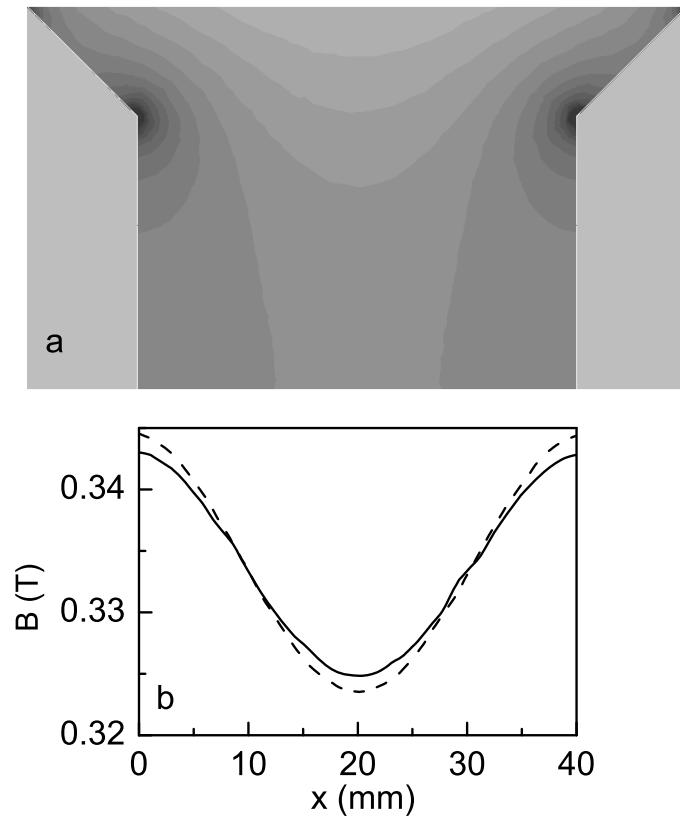


Figure 4.3: (a) Contour plot of the magnetic flux density in the air gap between the electromagnet poles, for a current of 10A. (b) The magnetic flux density along the magnet axis (solid line) and along a line 5mm displaced from the center (dashed line)

optical experiments in chapter 3. The gap has a width of 4cm, while the pole piece surfaces have a diameter of 5cm. Near the magnet axis (bottom in fig. 4.3(a)), the field is almost homogeneous while further away from the center, inhomogeneity becomes more pronounced. As is well-known, the field lines are focused at the points, where the curvature of the surface is large. This is indeed observed in fig. 4.3(a) by the dark areas near the pole edges.

Plots of the magnetic flux density B on a line parallel to the magnet axis,

all exhibit a shape similar to that of fig. 4.2(b). In the center of the gap, a minimum is observed, which becomes more pronounced with increasing distance from the symmetry axis (compare the solid and dashed lines in fig. 4.3(b)). On the axis the field variation is only 5% but it increases to 50% at larger distances from the magnet axis. We can conclude that inside a centered $5\text{mm} \times 5\text{mm}$ region, a quasi-homogeneous magnetic field exists with inhomogeneities smaller than 5%.

4.4 Inhomogeneous magnetic fields

In this section, we will focus on different non-symmetric magnet geometries, which generate inhomogeneous fields. The magnetic field, as well the gradient distribution, will be described, and their (dis-)advantages will be discussed.

4.4.1 Single permanent magnet

The easiest way to obtain a magnetic field gradient is by using a single permanent magnet. The flux lines in the magnet are parallel due to the fact that the magnetic moments of the individual atoms are all aligned in one preferred direction. Outside of the magnet the flux lines will spread out from the north pole and converge at the south pole. There are two ways which enable the tuning of flux density, as well as the field gradient. Modification of the geometry of the magnet, i.e. changing the shape of the poles, is one way to vary the magnetic field. Alternatively, changing the distance from the magnet will influence the field strength as the flux density decreases for large distances.

In fig. 4.4(a) the magnetic flux density for a cylindrical AlNiCo permanent magnet (12mm diameter, 75mm length) with the magneto-anisotropy axis parallel to the long axis is shown. As can be observed in the plot from fig. 4.4(b), the magnetic flux density is very high at the surface of the magnet at one of the poles; it amounts to 0.35T. Within approximately 0.5mm the field strength drops by about 50%, while for larger distances the decay of \mathbf{B} is much slower. For distances exceeding 30mm the flux density vanishes.

Within 10mm from the magnet pole, there is a significant gradient in the magnetic field, which amounts to approximately 15mT/mm. Considering a nanocolloidal Fe_3O_4 particle with a diameter of 10nm, the magnetic energy (eq. 4.2) is calculated to be $9.1 \cdot k_B T_r$. In fact, these results are consistent with the frequently used demonstration of a ferrofluid, which can be 'pulled up' the glass wall of a beaker using a hand-held bar magnet.

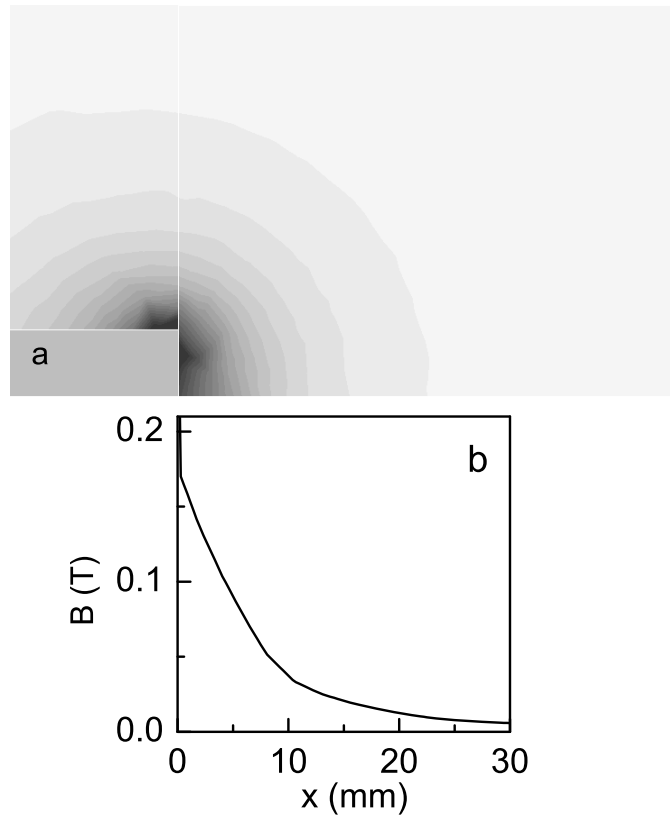


Figure 4.4: (a) Contour plot of the magnetic flux density, as determined by FEMM, in the vicinity of a single pole of an AlNiCo bar magnet. (b) Distance dependence of the magnetic flux density along the magnet axis.

4.4.2 Conically modified pole shape

As was already observed in the previous section on homogeneous magnetic fields, the finite dimensions of a conventional electromagnet, such as the one in fig. 4.1, induces slight inhomogeneities in the field, which are most pronounced at strongly curved surfaces. This 'focusing' of field lines to extremities can be exploited to generate well-defined inhomogeneous magnetic fields. In our first calculation, one of the pole pieces of our magnet in fig. 4.1 is replaced by a conical one, as is illustrated in fig. 4.5(a). The calculations using FEMM indeed show that the flux density is largest at the

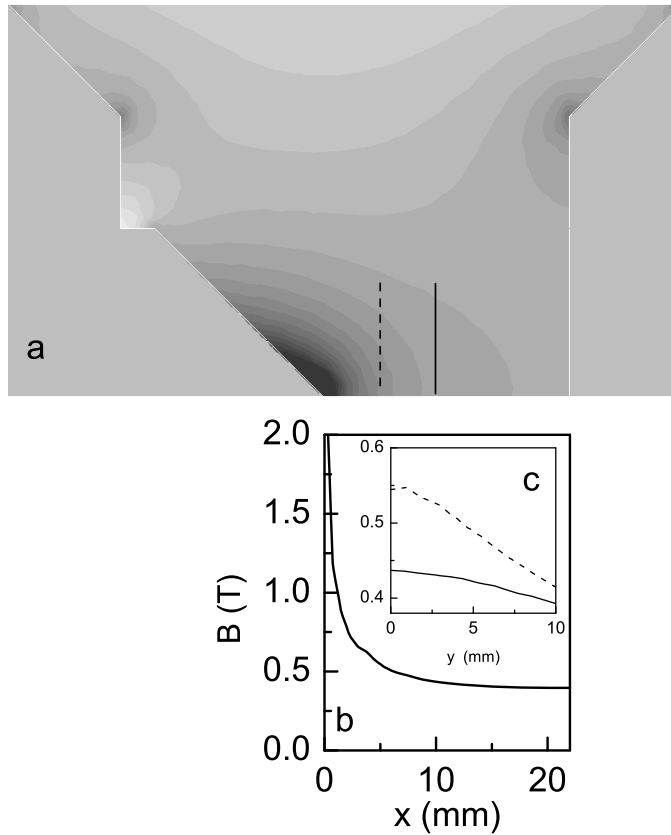


Figure 4.5: (a) Contour plot of the magnetic flux density as determined using FEMM, in the air gap between the electromagnet poles, for a current of 10A. (b) The magnetic flux density along the magnet axis. (c) The magnetic flux density in the radial direction, y , 5mm away from the modified pole apex (dashed line), and 10mm (solid line). The two lines in (a) indicate where the radial plots were made.

very apex of the conical pole. Comparing the value of 2.44T to the field in case of the symmetric magnet configuration (0.35T, see fig. 4.3(b)), the field enhancement is considerable.

Upon moving from the conical pole to the planar pole, the flux density drops to a value of 0.47T. The distance-dependent magnetic flux density plot on the magnet axis in fig. 4.5(b) clearly exhibits the decrease of the magnetic

field, but also shows the decline of the field gradient toward the flat pole. Due to the rapid decrease of the magnetic field away from the magnet axis, as well as the fact that the field lines are not parallel to each other near the conical pole, this is not an ideal geometry for any experiments which require constant field gradients over the sample areas of approximately $0.25 - 1\text{cm}^2$.

In the previous, we only focused on the gradient parallel to the axis. For driving the particles toward a surface which is perpendicular to magnet axis, this suffices. However, there is also a radial component, which may be interesting. The degree of order of nanoparticles depends on a number of parameters, including polydispersity, surface roughness and particle concentration. In all cases there must be a balance between repulsive and attractive forces. The former one is generally due to steric interaction while the latter force would be due to a magnetic gradient in the radial direction. As can be seen in fig. 4.5(c), there is a significant gradient in the radial direction, which induces also a net force on the particles toward the electromagnet axis. At 5mm away from the modified pole apex there is a gradient of approximately 10mT/mm , which is strong enough to compete with the Brownian motion as we have shown earlier. Obviously, for larger distances this radial gradient decreases.

4.4.3 Truncated cone modified pole shape

Using the results in the previous subsection, which indicate strongly inhomogeneous fields for asymmetric configurations, we set out to investigate a configuration, in which the field gradients are well-defined over areas corresponding to our sample sizes. For this reason, the conical extension in fig. 4.5(a) was truncated by removing the top 5mm of the cone. In fig. 4.6(a) the magnetic flux density obtained using FEMM is shown. Similar features are observed in the contour plot, of which the field line focusing is the most prominent at strongly curved surfaces. Our attention will focus on the cylindrical region around the magnet axis with a diameter equal to the truncated pole. As can be seen in fig. 4.6(b), the magnetic flux density at the truncated pole shoe center is much lower than in the case of conical pole in in fig. 4.5, primarily due to the geometrical change. Also, the slightly larger distance between the two poles has an effect on the field strength.

In fig. 4.6(b), we also compare the flux density along the magnet axis (solid line) and along a line at 2.5mm distance from the axis (dashed line). Surprisingly, the decay of the magnetic field is almost identical for both curves, indicating that the magnetic field as well as its gradient are constant over an area approximately equal to the surface of the truncated cone, i.e.

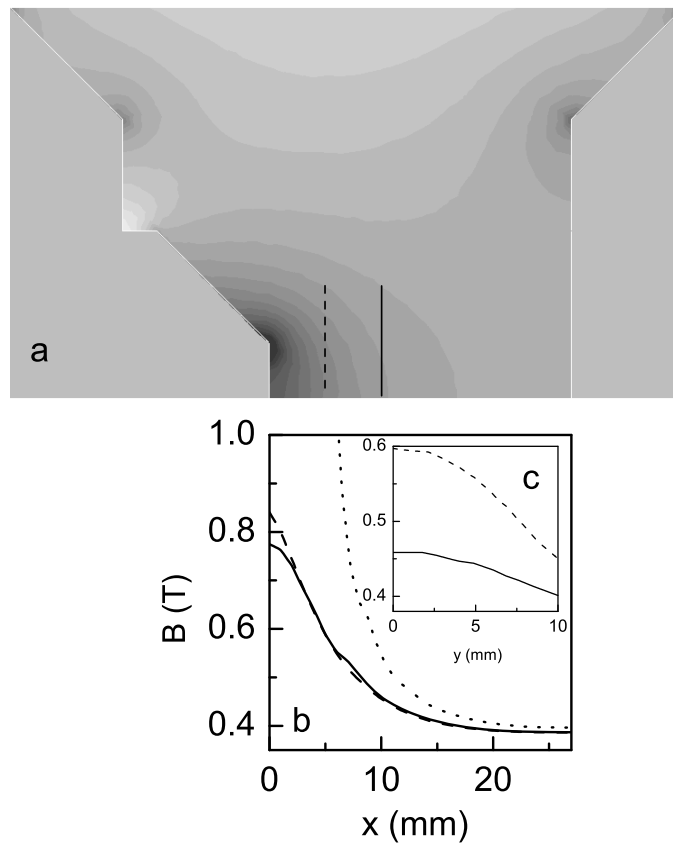


Figure 4.6: (a) Contour plot of the magnetic flux density obtained using FEMM, in the air gap between the electromagnet poles, for a current of 10A. (b) The magnetic flux density along the magnet axis (solid line) and along a line 2.5mm displaced from the center(dashed line); the dotted line is the magnetic flux density in the conical pole case fig. 4.5. (c) The magnetic flux density in the radial direction, y , 5mm away from the modified pole surface (dashed line), and 10mm (solid line). The two lines in (a) indicate where the radial plots were made.

≈ 5 mm. In this region, the field gradient is a constant, and only depends on the applied current. The magnetic flux density B scales approximately linearly with the current, and consequently this also holds for the gradient.

Also, as was calculated in the previous subsection, we plot in fig. 4.6(c)

the radial magnetic flux density. In agreement with the negligible difference between the solid and dashed lines in fig. 4.6(b), the magnetic flux density is almost constant within 2.5mm of the pole surface. Inhomogeneities appear for larger distances. This radial magnetic flux density induces a movement of the particles toward the magnet axis. Because its gradient is negligible on a surface of 2.5mm radius perpendicular to the axis, the magnetically induced attractive interparticle interaction is negligible, and only repulsive dipole-dipole interaction remains.

4.4.4 Single electromagnet pole

To accommodate the sample, the sample holder and the desired magnet configuration for various measurements, a large gap between the pole shoes is required. To obtain similar fields and gradients in a larger sample area, i.e. a larger gap between the poles, considerably larger currents are required in configurations of much larger dimensions. An alternative is to use only half of a conventional electromagnet, and use the available space to place the sample and its holder.

The principles of a ‘single electromagnet pole’ are similar to that of a bar magnet, but there are two main advantages: (i) the magnetic flux density at specific points in the sample space is tunable via the current in the coils, and (ii) consequently, the magnetic field line distribution remains unchanged. The divergence of the field lines away from the poles forces us to place our sample as close to the pole shoe as possible.

The geometry we insert into FEMM (see the insert in fig. 4.7(a)) for the calculation is very similar to the experimental configuration we will use in the next chapter. The extension of the original pole is a 12.2cm long cylinder with a radius of 15mm, having a tapered extremity with a final radius of 5mm. The magnetic flux density was calculated using FEMM and measured with a transverse Hall probe IDR-309 KiloGaussmeter.

In fig. 4.7(a), the calculated and measured magnetic flux densities are compared for different applied currents and varying distance from the pole. Apparently, there is reasonable agreement between calculation and experiment. The magnetic flux density at a fixed point on the magnet axis can be tuned almost linearly by varying the applied current. With respect to the divergence of the field at larger distance from the pole surface, the deviation of the \mathbf{B} direction with respect to the magnet axis, at a point 20mm from the pole surface and 5mm from the magnet axis, is approximately 7.5° . This value is independent of the applied current, as is to be expected.

The gradient of the magnetic flux density on the magnet axis is plotted

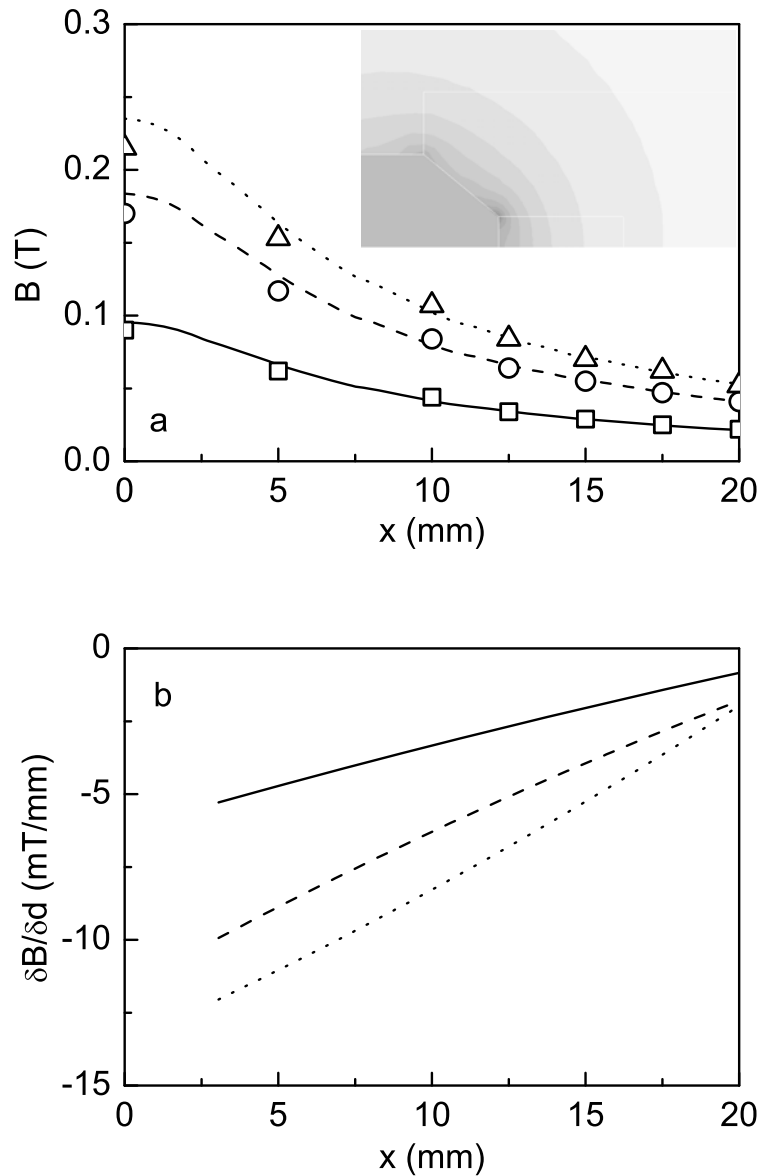


Figure 4.7: (a) Magnetic flux density on the axis of the magnet in the vicinity of the pole shoe, calculated with FEMM (lines) and measured (symbols) for currents of 5A, 10A and, respectively 15A. The inset is the contour plot of the magnetic flux density obtained using FEMM, in the vicinity of the electromagnet pole, for a current of 10A (b) The magnetic flux density gradient for the same values of the applied current.

in fig. 4.7(b). For currents smaller than approximately 10A, there is a linear dependence on the distance and the applied current. The values, about 3 times lower than those calculated in the air gap of the two poles geometry, are sufficiently strong for our experiments.

4.5 Conclusions

Several different conventional (electro)magnet configurations are presented. The spatial distribution of the magnetic flux density in the air gap (for 2 pole-configuration) and in the vicinity of one of the poles (for single magnets), is calculated using a finite element method. This has the advantage that essentially any configuration can be investigated accurately and relatively fast.

Considerable magnetic field gradients can be obtained using relatively low currents and moderate voltages. The main focus of this chapter was to understand and control the magnetic flux density in the desired space, i.e. the sample volume, only by varying the applied current. Modification of the pole shoes to yield an asymmetric geometry is shown to have a significant effect on the field distribution and also on the magnitude of the generated gradients. We show that the tunable magnetic field gradients are sufficiently large to compete with Brownian motion of the magnetic nanoparticles in suspension. Owing to this effective competition, magnetophoretic deposition can, in principle, be achieved.

References

- [1] H. C. Ørsted, *Experimenta circa effectum conflictus electrici in acum magneticam*, Copenhagen, 1820.
- [2] A. M. Ampère, *La théorie mathématique des phénomènes électrodynamiques uniquement déduite de l'expérience*, 1827.
- [3] W. Sturgeon, Transactions of the Society for the Encouragement of the Arts **43** (1824).
- [4] J. Henry, Am. J. Sci. Art. **19**, 404 (1831).
- [5] <http://www.magnet.fsu.edu/spotlights/pulsed75T/>.
- [6] K. Butter, K. Kassapidou, G. J. Vroege, and A. P. Philipse, J. Colloid. Interf. Sci. **287**, 485 (2005).
- [7] M. P. Pileni, C. R. Chim. **6**, 965 (2003).
- [8] Y. Lalatonne, J. Richardi, and M. P. Pileni, Nat. Mater. **3**, 121 (2004).
- [9] W. A. de Heer and P. Milani, Rev. Sci. Instrum. **62**, 670 (1991).

-
- [10] J. P. Bucher and L. A. Bloomfield, *Int. J. Mod. Phys. B* **7**, 1079 (1993).
- [11] R. K. Das, A. Konar, and S. Dattagupta, *Phys. Rev. B* **71**, 014442 (2005).
- [12] T. Y. Ying, F. C. Prenger, L. A. Worl, M. D. Johnson, J. A. Waynert, and R. M. Wingo, *Separ. Sci. Technol.* **39**, 2915 (2004).
- [13] K. Smistrup, O. Hansen, H. Bruus, and M. F. Hansen, *J. Magn. Magn. Mater.* **293**, 597 (2005).
- [14] F. Carpino, L. R. Moore, M. Zborowski, J. J. Chalmers, and P. S. Williams, *J. Magn. Magn. Mater.* **293**, 546 (2005).
- [15] H. Watarai, M. Suwa, and Y. Iiguni, *Anal. Bioanal. Chem.* **378**, 1693 (2004).
- [16] M. Zborowski, G. R. Ostera, L. R. Moore, S. Milliron, J. J. Chalmers, and A. N. Schechter, *Biophys. J.* **84**, 2638 (2003).
- [17] C. Wilhelm, C. Billotey, J. Roger, J. N. Pons, J. C. Bacri, and F. Gazeau, *Biomaterials* **24**, 1001 (2003).
- [18] B. W. Barry, *Eur. J. Pharm. Sci.* **14**, 101 (2001).
- [19] D. L. Holligan, G. T. Gillies, and J. P. Dailey, *Nanotechnology* **14**, 661 (2003).
- [20] M. Giersig and M. Hilgendorff, *Colloid. Surface. A* **202**, 207 (2002).
- [21] F. X. Redl, K. S. Cho, C. B. Murray, and S. O'Brien, *Nature* **423**, 968 (2003).
- [22] A. Vorobiev, J. Major, H. Dosch, G. Gordeev, and D. Orlova, *Phys. Rev. Lett.* **93**, 267203 (2004).
- [23] M. Hilgendorff, B. Tesche, and M. Giersig, *Aust. J. Chem.* **54**, 497 (2001).
- [24] R. E. Rosensweig, *Ferrohydrodynamics*, Dover Publications, INC., New York, 1997.
- [25] <http://femm.foster-miller.net/> .
- [26] S. Chikazumi, *Physics of ferromagnetism*, Oxford University Press, New York, 1997.

Chapter 5

In situ study of ferrofluids in external magnetic fields

Abstract

In this chapter, the influence of external magnetic fields on the redistribution of magnetite (Fe_3O_4) nanoparticles in an oil-based ferrofluid is investigated. In the first part, the presence of a very moderate magnetic field gradient is shown to give rise to a separation of the ferrofluid in low- and high-density phases. Upon removing the applied field, intriguing flow behavior is observed. The results are discussed in terms of density variations in the fluid. The second part describes an in situ study of magnetophoretic deposition of magnetite nanoparticles by means of spectroscopic ellipsometry in a total internal reflection configuration. A description of the experimental set-up is followed by a discussion of the magnetophoretic deposition results in terms of particle size distribution and reorganization of particles at the interface.

5.1 Introduction

One of the most flexible ways to tune and control the interactions between magnetic nanoparticles, suspended in a solvent (also generally referred to as a ferrofluid), is by applying an external magnetic field. In the case of a homogeneous field, the alignment of dipolar entities will give rise to net interactions between neighboring particles. These interparticle forces are repulsive and attractive in the directions perpendicular and parallel to the applied field, respectively. When the external field is inhomogeneous, i.e. there is a gradient in the magnetic flux density, a net translational force will act on the individual dipolar nanoparticles. As we have shown in the previous chapter, sufficiently large field gradients can give rise to migration of the particles, thus enabling the assembly of the nanoscale magnetic entities into three-dimensional superstructures. To control the formation of magnetic assemblies and achieve reproducible adsorption of films at a substrate, a number of parameters is to be considered. Among them are the degree of polydispersity of the suspension from which the particles are assembled, the magnetic properties of the nanoparticles, the specific geometry of the magnetic field and also drying effects occurring when removing the superstructures from the liquid environment.

Over the past decade, magnetic field-induced self-assembly of magnetic nanoparticles has attracted considerable interest. A large variety of two- and three-dimensional superstructures of magnetic nanoparticles and nanocrystals, assembled using magnetic fields and field gradients, has been reported [1–11]. Magnetic field gradients have also been used to align multiwalled carbon nanotubes coated with magnetic nanoparticles [12]. Magnetophoretic deposition has also been reported as a valuable tool in the fabrication of various nanocomposites. In one example, magnetic nanoparticles are assembled and held on an electrode surface at a predefined density, after which metal atoms are electrochemically deposited in the interstices between them [13]. In another report, a field gradient is used to drive nanoparticles into a polycarbonate membrane to produce granular magnetic nanowires [14].

Non-invasive in situ experiments on the behavior of ferrofluids in (in)homogeneous magnetic fields and also during the deposition of nanoparticles at surfaces can, in principle, reveal the different mechanisms relevant for migration and assembly of magnetic nanoparticles. In this chapter we use optical methods to study the behavior of an oil-based Fe_3O_4 suspension in inhomogeneous magnetic fields. First, we use video imaging to study the phase-separation in dilute suspensions of magnetic nanoparticles in the presence of slightly inhomogeneous field. In the second part of this chapter, we

use in situ spectroscopic ellipsometry to investigate the reversible adsorption and assembly of magnetic nanoparticles at a solid-liquid interface.

5.2 Visualization and kinetics of ferrofluid phase-separation

5.2.1 Experimental observations

During experiments similar to those described in chapter 3, we obtained some anomalous results, which could not be accounted for by established theories. Most prominently, when an approximately homogeneous field is applied for long periods of time, using a geometry such as that shown in fig. 4.3 in the previous chapter, irreproducible intensity variations were often observed. Visual inspection of the system under consideration, i.e. a thin-film glass cell (a standard Starna cuvette) with a 1mm optical path length, filled with an oil-based magnetite (Fe_3O_4) revealed interesting phenomena related to field-induced phase separation.

It is well-known that ferrofluids, consisting of dispersed magnetic nanoparticles, exhibit phase-separation under the influence of an applied external field [10, 15–18]. Labyrinth-like fingering and column-like structures are generally observed, which are generally attributed to anisotropic interactions between the nanoparticles in suspensions. For fields parallel to a thin film cell, wire-shaped aggregates of particles align along the field direction. Mutual distances between the wires as well as their lengths can be controlled by the magnetic flux density, the rate of increase of the flux and also the time the field is applied. Magnetic fields perpendicular to a thin film cell give rise to hexagonally ordered patterns of high-density drop-like aggregates in a low-density matrix. In more theoretical treatments, the phase-separation of the ferrofluid with initial concentration into two phases with lower and higher concentrations is generally described in terms of a “ferrocolloidal gas-ferrocolloidal liquid” phase transition. However, in our case the volume fraction of the ferrofluid occupied by magnetite particles $\Phi = 1.56 \times 10^{-3}$ is considerably smaller than what has previously been considered.

In fig. 5.1, the aforementioned glass cell filled with the Fe_3O_4 ferrofluid is shown after application of a field of approximately 1T for 15min or more. In (a) the field is still applied. On both sides of the cell, the truncated cone-shaped pole-pieces are visible; the gap separating the poles amounts to 20mm. Close examination of fig. 5.1(a) shows that the transmission at the very top of the cuvette, near the liquid/gas interface, is larger than in the

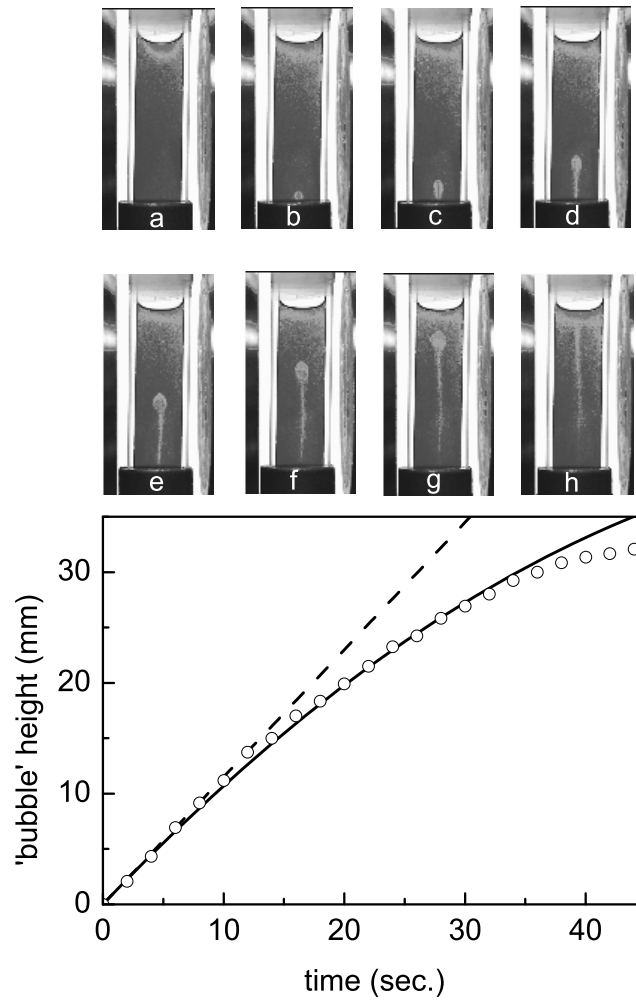


Figure 5.1: Series of photographs depicting the field-induced phase separation in a magnetite ferrofluid. The inner width of the glass cell amounts to 10mm. The applied field is oriented from left to right. The images were recorded (a) at the moment of switching off the magnetic field, (b) after 2s, (c) 4s, (d) 8s, (e) 14s, (f) 22s, (g) 32s, and (h) 44s. The contrast in the images has been enhanced considerably to visualize relevant features. The height of the low density 'bubble' as a function of time is shown in the graph. The dashed and solid lines are described in the text.

rest of the cell volume. The intensity profile, which actually visualizes the nanoparticle density in the suspension, is very similar to the flux density distribution between the poles, as shown in fig. 4.3(a). The same behavior occurs at the bottom of the glass cell, but because it is inserted into a holder, this is less clearly visible. The slight gradient of the magnetic field gives rise to a density variation throughout the cuvette.

When the magnetic field is switched off, a peculiar flow profile of the ferrofluid is observed in the sequence of images in fig. 5.1(b)-(h). The absence of the magnetic field results in a relaxation of the liquid/air interface, as is best seen by comparing figs. 5.1(a) and (b). Within approximately two seconds, the lower particle density region at the bottom of the cuvette develops into a ‘bubble’ of low density phase that starts to rise in the higher density liquid. The nucleation of the ‘bubble’ is always in the middle between the two poles of the magnet. In fig. 5.1 the cuvette was centered between the magnet poles, so the low-density region is also in the middle of the cuvette. However, if the cuvette is displaced from the centered position between the pole pieces by a certain distance, the ‘bubble’ still originates exactly in the middle of the gap between the poles.

During its ascent upwards, the ‘bubble’ develops a tail-like feature. Surprisingly, despite considerable convection in the liquid, the two phases (low density ‘bubble’ and high density surrounding liquid) remain reasonably well-separated. Also, the shape changes slightly with increasing height, while the ‘tail’ eventually disappears (see fig. 5.1(g) and (h) at the bottom). The height of the top of the ‘bubble’ as a function of time is also depicted in the graph in fig. 5.1. Apparently, the speed with which the ‘bubble’ rises toward the surface decreases with increasing height. A more quantitative analysis will be given below.

If the cuvette is left for sufficient time, typically 5 – 10min, diffusion again restores the homogeneously distributed ferrofluid. However, when the magnetic field is applied during the ascent of the ‘bubble’, again peculiar behavior is observed. Upon reapplying the field before the ‘bubble’ reaches the magnet axis, i.e. the middle of the cuvette, the ‘bubble’ seems to descend and the density distribution in the liquid is restored very rapidly to the situation prior to switching off the magnetic field. When the magnetic field is increased after the ‘bubble’ has passed the middle of the cuvette, its ascending speed increases markedly and the ‘tail’ vanishes within seconds, to also yield the original density distribution before switching off the field. Apparently, the ‘bubble’ with lower density ferrofluid rushes toward its lowest energetic position, i.e. at the top or bottom of the cuvette, depending on which of these is at a shorter distance.

5.2.2 Quantitative analysis

For a quantitative analysis of the experimentally determined height of the ‘bubble’ as a function of time, shown in fig. 5.1, we treat the system in a way comparable to the settling of colloidal particles in a gravitational field [19], but in this case it is reversed. If we consider the ‘bubble’ to have a lower density related to a lower concentration of magnetite nanoparticles, there are two forces acting on it. The lower density and thus weight of the ‘bubble’ gives rise to a buoyancy force F_{buoy} given by

$$F_{\text{buoy}} = V \cdot \Delta\rho \cdot g \quad (5.1)$$

where V is the volume of the ‘bubble’, $\Delta\rho = \rho_0 - \rho_1$ is the density difference between the surrounding ferrofluid (ρ_0) and the ‘bubble’ (ρ_1) and $g = 9.81\text{m/s}^2$. This force is directed upwards.

As soon as the ‘bubble’ moves, it will experience a drag force F_{drag} given by

$$F_{\text{drag}} = 6\pi\eta r \cdot u \quad (5.2)$$

where $\eta = 0.9\text{mPa} \cdot \text{s}$ is the viscosity of the solvent (cyclohexane), r is the effective radius of the ‘bubble’ and u is its velocity. As mentioned above, the buoyancy force is directed upwards, which implies that the drag force is directed downwards.

Similar to what is assumed for settling colloidal particles, but what is also observed for rising gas bubbles in a liquid, a steady-state situation with a constant velocity u is reached relatively fast. If the ascending velocity is time-independent, the net force on the rising ‘bubble’ is zero, so eqs. 5.1 and 5.2 are equal. This yields an expression for the density difference

$$\Delta\rho = \frac{6\pi\eta r}{Vg} u \quad (5.3)$$

From the initial ‘bubble’ in fig. 5.1(c) we estimate its radius to amount to approximately $r = 1.05\text{mm}$, and its initial velocity to amount to 1.15mm/s . The latter is indicated by the dashed in the plot of the height as a function of time in fig. 5.1. With the volume $V = 4\pi r^3/3$ and the aforementioned viscosity η , we find that $\Delta\rho = 4.31 \times 10^{-4}\text{kg/m}^3$. For a fill fraction $\Phi = 1.56 \times 10^{-3}$ (see chapter 3), we find a density $\rho_0 = \rho_{\text{cyclo}}(1 - \Phi) + \rho_{\text{Fe}_3\text{O}_4}\Phi = 0.785\text{gr/cm}^3$, where $\rho_{\text{cyclo}} = 0.779\text{gr/cm}^3$ and $\rho_{\text{Fe}_3\text{O}_4} = 5.10\text{gr/cm}^3$ are the densities of cyclohexane and magnetite (Fe_3O_4), respectively. The density difference $\Delta\rho = \rho_0 - \rho_1$ yields a value for the ‘bubble’ density ρ_1 from which we estimate the fill fraction in the ‘bubble’ to amount to $\Phi = 1.46 \times 10^{-3}$.

From the absorbance spectrum in fig. 3.3 we estimate the initial transmission of the suspension at a wavelength of 650nm in a 1mm cuvette to amount to 25%. Using the Lambert-Beer law, the lower density and corresponding fill fraction leads to a higher transmission of approximately 27.5% in the ‘bubble’-region. We stress that the contrast in the images in fig. 5.1 has been enhanced considerably.

As is clearly seen in fig. 5.1 the ‘bubble’ develops a tail-like feature when it rises toward the surface. This implies that its effective volume decreases. Alternatively, one can consider that due to mixing induced by convection, the density ρ_1 increases with time, i.e. $\Delta\rho$ decreases for larger heights. We can take this into account by assuming that the velocity decreases linearly with time

$$u(t) = \frac{\Delta\rho \cdot Vg}{6\pi\eta r}(1 - ct) \quad (5.4)$$

Integration of eq. 5.4 and fitting it to the data for $t < 30$ s yields the solid line in fig. 5.1 and a value for the time-dependence parameter $c = 0.014$. This implies that the ‘bubble’ density (or volume) decreases by 1.4% of its original value per second. As can be seen in fig. 5.1, the solid line corresponds quite well with the data up to a height of 30mm. Furthermore, comparing the ‘bubble’ in fig. 5.1(c) to that in fig. 5.1(f) reveals that its radius increases for larger heights. This implies that the drag force (eq. 5.2) becomes more pronounced and slows the ascent of the ‘bubble’. Finally, as it reaches the liquid/gas interface, the ‘bubble’ will obviously not rise any further but deform and eventually disappear.

5.3 In situ study of magnetophoretic deposition

As already described in the previous chapter, and as has been shown in work presented in literature [13, 14, 20], migration of magnetic nanoparticles can in principle be achieved using a moderate field gradient. Using the magnetic configuration presented in fig. 4.6, we visualized the accumulation of magnetic nanoparticles in an oil-based Fe_3O_4 ferrofluid (for details on the suspension, see chapter 3) under the influence of a magnetic field gradient. The result is shown in fig. 5.2. As can be clearly observed in the images, a high density region is formed at the cell wall near the pole of the electromagnet. The field gradient is largest near the pole, as shown in the contour plot of fig. 4.6, giving rise to the accumulation of nanoparticles in this region. At the surface of the truncated cone-shaped pole, the largest gradient is near the edge. Indeed, if the glass cell is placed as close to the pole as possible,

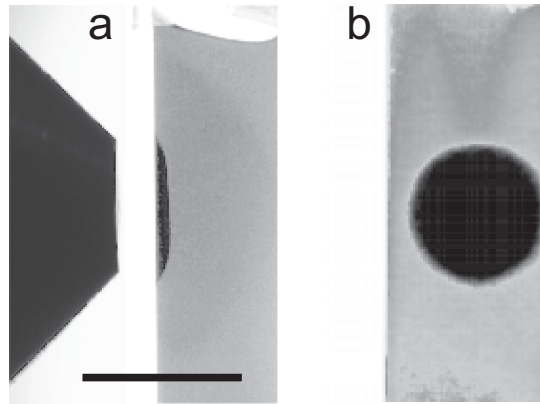


Figure 5.2: Side-view (a) and front-view (b) of a glass cell containing an oil-based magnetite ferrofluid, showing the accumulation of magnetic material, i.e. nanoparticles, under the influence of a magnetic field gradient. The nanoparticles accumulate in areas where the flux density is largest. In (a) the truncated cone-shaped magnet pole is visible. The contrast in the images is enhanced considerably using photo-editing software. The bar in (a) corresponds to 10mm.

a ring-shaped pattern of high density material is observed. In the following we present results on the application of spectroscopic ellipsometry to quantitatively characterize the assembly of nanoparticles at the solid/liquid interface as a function of applied field strength.

5.3.1 Experimental configuration

For the experiments described in this section, we used a standard rectangular glass cuvette (Starna), with inner dimensions of $10\text{mm} \times 10\text{mm}$. The cuvette acts as a glass cell, and has two clear windows, which are approximately 1.25mm thick. To enable optical access to the solid/liquid interface, and circumvent the problem of strong light absorption in the ferrofluid, a truncated glass prism is used in a total internal reflection configuration [21]. Furthermore, this configuration is most sensitive to the optical processes occurring at the solid/liquid interface. In fig. 5.3 a schematic representation of our experimental set-up is shown. Both the cell and the truncated prism are made of BK7 optical glass with high transmission in the visible range of the spectrum. To prevent reflections at the prism/cell interface,

the gap between the substrate and the cell is filled with a refractive index matching fluid (Immersion oil, $n = 1.515$, DIN 58884, Merck). Additionally, the surface tension of the immersion oil also provides sufficient adhesion between the prism and the glass window of the cuvette to keep them fixed with respect to each other.

Also shown in fig. 5.3 is the pole of the electromagnet employed to generate the magnetic field gradient enabling magnetophoretic deposition of nanoparticles. The magnet configuration is identical to the single electromagnet pole presented in chapter 4, depicted in fig. 4.7. The home-built, water-cooled electromagnet is powered by a Delta Elektronika SM3540 power supply. For details on the magnetic configuration, we refer to section 4.4.4. Since the truncated prism is required to provide optical access

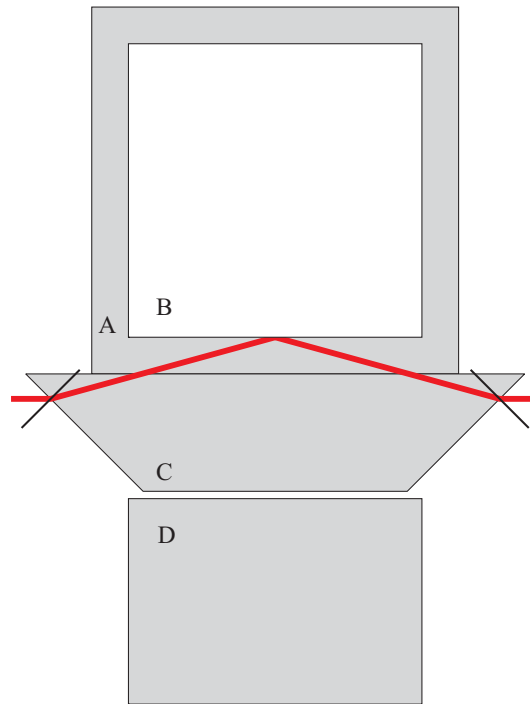


Figure 5.3: Schematic top-view cross-section of the glass fluid cell (walls A, volume B), the truncated prism (C) and electromagnet pole (D) used in our experiments. Between the glass cell and the prism, a thin film of immersion oil is present. The light path is indicated by the thick line; the thin lines depict the normal to the prism faces.

to the solid/liquid interface at which the nanoparticles are accumulated, the minimum distance between the magnet pole and this interface amounts to approximately 6mm. From fig. 4.7, it is found that for this configuration the maximum magnetic field, which can be achieved amounts to approximately 0.15T, while the field gradient is maximized to approximately 10mT/mm for the highest current density.

5.3.2 Spectroscopic ellipsometry

For the optical measurements, we use a Woollam Variable Angle Spectroscopic Ellipsometer (VASE) system, equipped with a high pressure Xe discharge lamp, which generates light in the spectral range 0.8 – 5eV from the near-IR to the UV. The lamp is incorporated in an HS-190 monochromator to enable spectral characterization of the interface.

In reflection ellipsometry, the change of the polarization state of linearly polarized light is measured upon reflection at an interface. Identical to what is described in chapter 2, the complex reflection coefficient ρ is defined as

$$\rho = \frac{r_p}{r_s} = \tan(\Psi) \exp(i\Delta) \quad (5.5)$$

where r_p and r_s are the reflection coefficients for the parallel and perpendicular polarizations, respectively. Historically, the quantity ρ is expressed in the two angles Ψ and Δ [22]. Although the actual ellipsometry measurement is relatively simple, the analysis of the results is often complicated. An accurate model is required for the system under investigation, which enables simulation or fitting of the results.

For reflection at a single interface between two media with refractive indices n_0 and n_1 , r_p and r_s represent the Fresnel reflection coefficients given by

$$r_p = \frac{n_1 \cos \theta_0 - n_0 \cos \theta_1}{n_1 \cos \theta_0 + n_0 \cos \theta_1} \quad (5.6a)$$

$$r_s = \frac{n_0 \cos \theta_0 - n_1 \cos \theta_1}{n_0 \cos \theta_0 + n_1 \cos \theta_1} \quad (5.6b)$$

where the angles of incidence and refraction θ_0 and θ_1 are related through Snell's law

$$n_0 \sin \theta_0 = n_1 \sin \theta_1 \quad (5.7)$$

If the two media are transparent, i.e. both indices of refraction are non-complex quantities, the angles θ_0 and θ_1 are also real. Otherwise, when

either one of the two media is absorbing and has a non-vanishing imaginary part of the refractive index, the aforementioned angles will in general be complex quantities.

The propagation of the incident and reflected light beam in our total internal reflection set-up is shown in fig. 5.3. As described in the previous section, the glass cell is mounted on the long side of a truncated, triangular prism. The incident beam enters the prism at one of the short sides and after reflection at the inner surface of the cuvette, leaves the prism again at the other side. In this way, light does not propagate through the strongly absorbing ferrofluid suspension. The incident light is totally reflected, implying a high reflection intensity. There is no propagating wave in the suspension; the exponentially decaying evanescent field probes the interface where magnetophoretic deposition occurs. A major advantage of this configuration is that it allows to accommodate the electromagnet.

In addition to the reflection ρ at the inner surface of the glass cell, the light is also refracted at the air/glass interface upon entering the prism, and also at the glass/air interface upon exiting the prism (see fig. 5.3). Therefore, the additional contribution to the polarization change of the light must be taken into account. The total measured reflection coefficient ρ_{exp} is related to ρ through

$$\rho_{\text{exp}} = \frac{t_{\text{p}}^{\text{ag}}}{t_{\text{s}}^{\text{ag}}} \cdot \rho \cdot \frac{t_{\text{p}}^{\text{ga}}}{t_{\text{s}}^{\text{ga}}} \quad (5.8)$$

where $t_{\text{p,s}}^{\text{ag}}$ and $t_{\text{p,s}}^{\text{ga}}$ are the Fresnel transmission coefficients at the air/glass and glass/air interface, respectively, for parallel and perpendicular polarized light. The Fresnel transmission coefficients can be rewritten [22] using Snell's law (eq. 5.7) to yield

$$t_{\text{p}} = \frac{2 \sin \theta_1 \cos \theta_0}{\sin(\theta_0 + \theta_1) \cos(\theta_0 - \theta_1)} \quad (5.9a)$$

$$t_{\text{s}} = \frac{2 \sin \theta_1 \cos \theta_0}{\sin(\theta_0 + \theta_1)} \quad (5.9b)$$

Applying these equation to the air/glass and glass/air interfaces and inserting them into eq. 5.8 yields

$$\rho_{\text{exp}} = \frac{1}{\cos(\theta_{\text{a}} - \theta_{\text{g}})} \cdot \rho \cdot \frac{1}{\cos(\theta_{\text{g}} - \theta_{\text{a}})} = \frac{\rho}{\cos^2(\theta_{\text{a}} - \theta_{\text{g}})} \quad (5.10)$$

in which $\theta_{\text{a}} = 45^\circ$ (defined by the 90° top angle of the prism) and θ_{g} are the incident and refracted angles, respectively, with respect to the normal

of the short sides of the prism. The incident angle θ_0 on the inner surface of the glass cell is given by $\theta_0 = 45^\circ + \theta_g$. The angle θ_g is related to θ_a through Snell's law. Since θ_g depends on the refractive index of the prism, and the latter is a function of the photon energy of the light, the incident angle θ_0 also varies slightly with the photon energy. Using the refractive index of BK7 optical glass (dashed line in fig. 5.4(a)) we find that the effective incident angle θ_0 decreases from 72.92° to 72.37° between 1.5eV and 3.5eV (solid line in fig. 5.4(b)).

Now that we know the wavelength-dependent refraction angle in the prism, the correction factor $\cos^2(\theta_a - \theta_g)$ in eq. 5.10 can be calculated as a function of photon energy. Since the BK7 glass is transparent over the entire measured photon energy range (0.8 – 3.5eV), the refraction angle θ_g , and consequently also the correction factor, is a real, non-complex quantity. Therefore, the correction factor, plotted in fig. 5.4(e), only influences the experimentally determined value of Ψ .

To characterize our set-up, we first measured the optical response of an empty cell, and also after filling it with cyclohexane (the solvent of the ferrofluids used in this work). The energy-dependent values of Ψ and Δ for both cases are shown in figs. 5.4(c) and (d), respectively. Also, for comparison, the calculated values for the ellipsometric angles, using the refractive indices for BK7 glass and cyclohexane (shown in fig. 5.4(a)) are depicted. Since in these cases we are dealing with transparent media, Ψ at the solid/liquid interface amounts to 45° for all photon energies. Taking into account the correction as given in eq. 5.10, results in good agreement between the calculated and measured Ψ . For Δ , the experimental and theoretical values do not agree very well. A possible reason for this discrepancy may be the influence of the thin film of index matching fluid (immersion oil), which is used to join the prism and the glass cell. Since we do not know the energy-dependent dielectric function of the immersion oil and it is not possible to control its thickness, we examine the differences in optical response between the experimental complex reflection coefficients ρ for the empty and cyclohexane-filled cases. This can be done by taking the ratio of both $\tan(\Psi)$ values, and the differences between the Δ angles. A similar comparison can be made for the two calculated spectra. As shown by the energy-dependent differences in Δ in fig. 5.4, a relative measurement is in fair agreement with the theoretical calculation. The deviation at higher energies may be attributed to an uncertainty in the cyclohexane refractive index [23]. The latter has been determined in the near-infrared, after which the spectrum has been extrapolated, introducing an increased inaccuracy at higher energies.

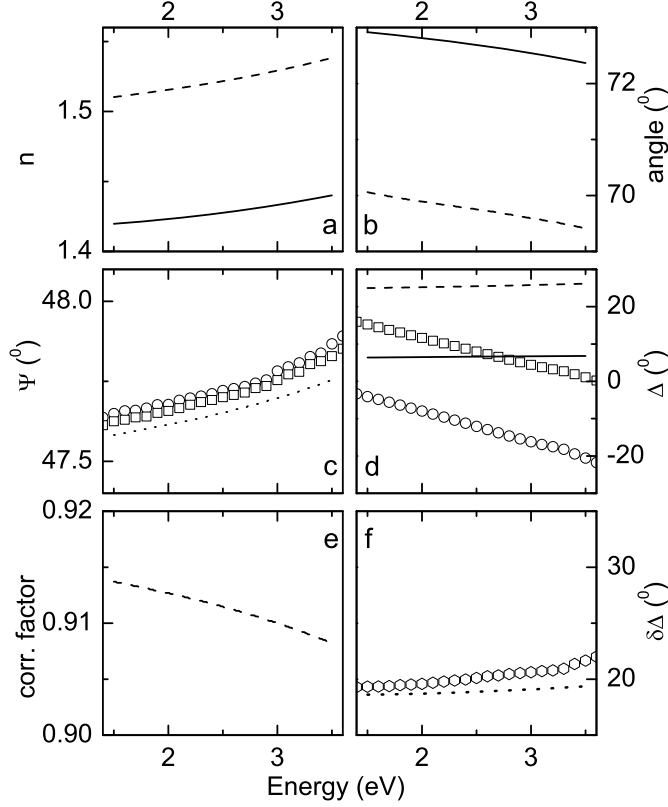


Figure 5.4: (a) Refractive indices of BK7 glass (Schott catalogue) and cyclohexane [23], as a function of photon energy (dashed and solid lines, respectively). (b) Incidence angle (solid line) and the total reflection critical angle (dashed line) for the glass/cyclohexane interface. (c,d) Experimental Ψ and Δ values, obtained with an empty (squares) and a cyclohexane-filled (circles) cell, compared to calculated angles. (e) Energy-dependent correction factor $\cos^2(\theta_a - \theta_g)$ in eq. 5.10. (f) Calculated (dotted line) and measured (symbols) difference in Δ between the empty and cyclohexane-filled case.

Finally, to check whether we are indeed operating our cell in total internal reflection mode, we calculated the critical incident angle θ_c above which light does not propagate at the liquid side of the interface. The angle θ_c is obtained from eq. 5.7 by setting the refracted angle $\theta_1 = 90^\circ$. In the case of an empty cell, i.e. air (with $n_1 = 1$) at the outer side of the interface, a value of approximately $\theta_c = 41^\circ$ is found. If the glass cell is filled with

cyclohexane, the optical contrast between the BK7 glass and the liquid is considerably smaller, due to the smaller difference in refractive index as shown in fig. 5.4(a). This results in a considerably larger critical angle, which is compared to the actual incidence angle in fig. 5.4(b). Although there is still total internal reflection, the penetration of the light into the liquid is markedly increased, which implies that the penetration depth of the evanescent field is considerable.

5.3.3 Results

Using the experimental set-up described in the previous sections, optical characterization of magnetophoretically deposited magnetite nanoparticles is performed using a standard procedure. First, the empty glass cell together with the prism is mounted on the sample holder of the ellipsometer, followed by an alignment procedure. This is done in the absence of a liquid, because in that case the critical angle for total internal reflection ($\theta_c \approx 41^\circ$) is smallest, and the reflection at the fixed angle of incidence ($\theta_0 \approx 72.5^\circ$, see fig. 5.4(b)) is highest. Subsequently, the cell is filled with ferrofluid having a fill fraction $\Phi = 1.6 \times 10^{-3}$. Without an applied field, a single spectrum, denoted by ρ_0 , is obtained as a reference for all other spectra measured in the same series. After application of an external field, spectra are measured as a function of time and/or applied magnetic field strength, denoted by $\rho(t, B)$. In all experiments the wavelength scan from 3.5eV to 0.8eV takes approximately 5min. To circumvent problems related to slight differences in alignment and other initial conditions, the spectra $\rho(t, B)$ are in all cases related to the initial spectrum ρ_0 of that specific experiment through

$$Y = \frac{\rho(t, B)}{\rho_0} - 1 \quad (5.11)$$

From preliminary experiments we found that using the complex quantity Y (in fact, a normalized difference spectrum) yields reproducible information on the processes occurring at the glass/liquid interface where magnetophoretically deposited particles accumulate.

In fig. 5.5, spectra obtained at various times and different applied magnetic field strengths are shown. At the glass/liquid interface the flux densities amount to approximately 50mT, 75mT and 100mT. As can be seen in fig. 4.7, the accompanying field gradients vary from approximately 5mT/mm to 9mT/mm. Although these fields and the corresponding gradients are relatively low, a clear change of the optical properties at the solid/liquid interface is observed. With time, the magnitude of the spectral changes increases

and also for larger applied fields, and thus larger magnetic field gradients, the changes become more significant.

Not only the magnitude of the spectra varies with time and applied field, also the shape of the spectra changes. For short times, and low magnetic field strengths, the real component of the normalized difference spectra exhibits a maximum (i.e. a minimal change) near approximately 1.5eV and a minimum near 3eV. The imaginary part also shows a shallow maximum near 1eV, a gradually decreasing minimum near 2eV and additionally, a characteristic

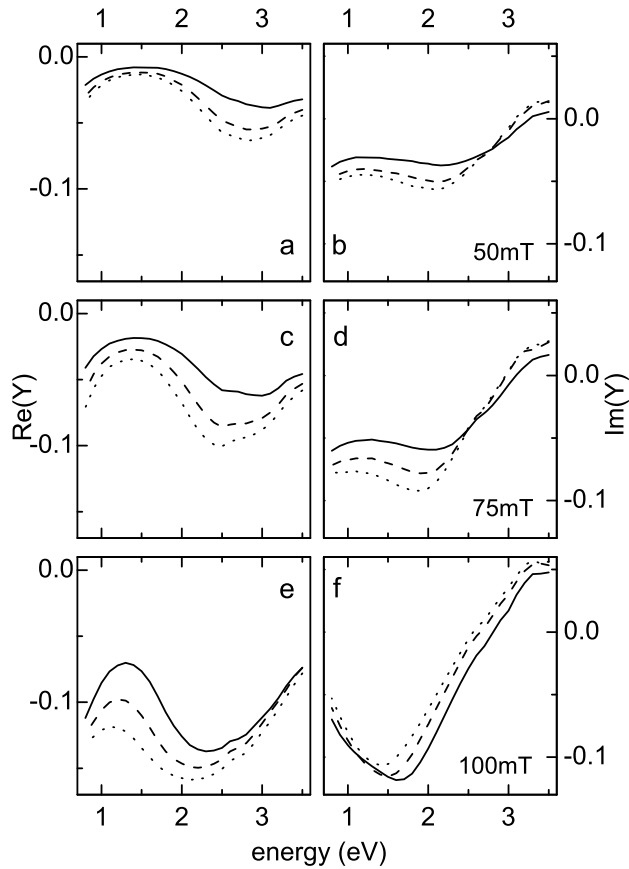


Figure 5.5: Real (a,c,e) and imaginary (b,d,f) components of the normalized change Y of the complex reflection coefficient after switching to magnetic field strengths of 50mT (a,b), 75mT (c,d), and 100mT (e,f). Spectra after 24min, $t = 96$ min and $t = 187$ min are shown, represented by the solid, dashed and dotted lines, respectively.

cross-over from negative to positive values around 3eV. With progressing time and at higher field strengths, all these spectral features move to shorter wavelengths.

To obtain a feeling for the time-scale at which the processes occur at the interface, the time-dependence of the quantity Y , after switching the magnetic flux density to a specific value, is shown in fig. 5.6. There are two time regimes, most pronounced in the real component. A fast drop of Y during the first 20min is followed by a much slower variation of the signal with time. For the imaginary parts, the signal even reaches a minimum after which it increases again.

In the initial regime, in which the optical response varies relatively fast, the rate of change (the slope in fig. 5.6) becomes larger for higher magnetic fields. This relation between decrease of $\text{Re}(Y)$ and $\text{Im}(Y)$ and the magnetic flux density is not that clear in the second regime where the variation of the aforementioned quantities is considerably smaller. Surprisingly, on the time-scale of our experiment, i.e. 200min, the spectra in fig. 5.5 do not yet

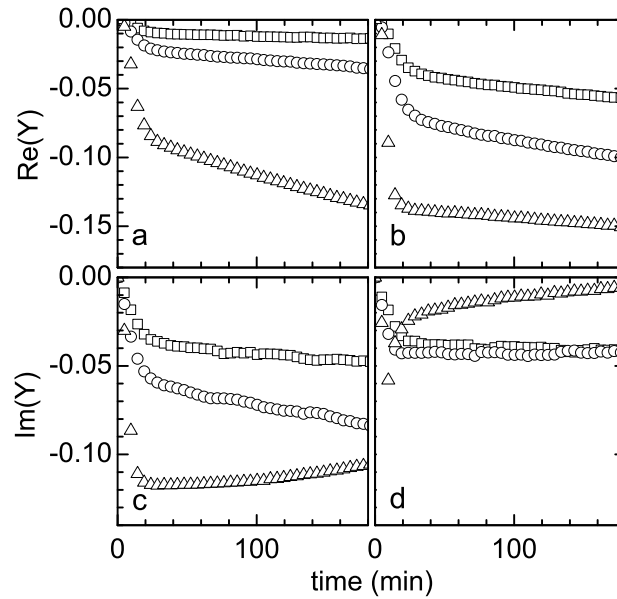


Figure 5.6: Time-dependence of the real (a,b) and imaginary (c,d) components of the normalized change Y of the complex reflection coefficient at photon energies of 1.5eV (a,c) and 2.5eV (b,d) after switching the magnetic field strength to 50mT (squares), 75mT (circles), and 100mT (triangles).

show a saturation. This is also obvious from the kinetic plots in fig. 5.6. Apparently, there are still processes occurring at the solid/liquid interface, which give rise to a variation of the optical response of the magnetite layer accumulating at the surface.

The aforementioned experiments were performed by stepping the magnetic field from zero to a specific value. Therefore, the results in fig. 5.6 reveal the kinetics in the presence of a constant magnetic field. In fig. 5.7 the results for a quasi-static experiment are presented. The magnetic field is increased (or decreased) step-wise with 2mT increments. After every change of the flux density, the system is left to relax for 10min before a next step is applied. For the results in fig. 5.7, the field is varied in the range 0 – 100mT, which implies that the maximum field strength is reached after 500min, substantially later than in the results of fig. 5.5. In every step we assume that the system reaches an equilibrium condition at that specific

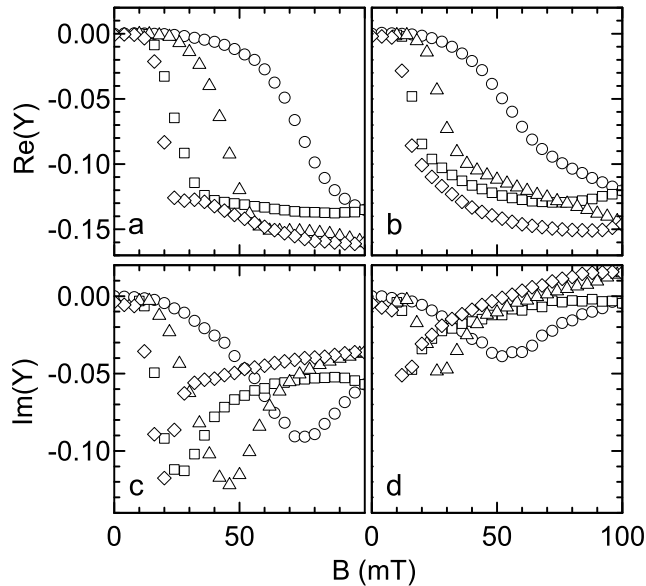


Figure 5.7: Real (a,b) and imaginary (c,d) components of the normalized change Y of the complex reflection coefficient at photon energies of 1.5eV (a,c) and 2.5eV (b,d) during a step-wise scan. The magnetic field strength is changed in step of 2mT/10min, subsequently from 0 – 100mT (circles), from 100 – 10mT (squares), from 10 – 100mT (triangles) and finally from 100 – 0mT.

field. The final optical response as observed in fig. 5.7 is comparable but not identical to that shown in fig. 5.6 for 100mT. As indicated above, the system apparently has not reached its equilibrium after 200min. In fact, in the first return scan, $\text{Re}(Y)$ still becomes more negative (most pronounced at 2.5eV, fig 5.7(b)) indicating that still material is being accumulated at the interface after 500min.

Furthermore, the system exhibits hysteresis in that the return scan from 100 – 10mT does not yield the same behavior as the initial scan from 0 – 100mT. Visual inspection of the glass cell and the ferrofluid is consistent with this. During the first increase of the magnetic field, a high-density phase forms at the solid/liquid interface, similar to that shown in fig. 5.2. However, upon step-wise decrease of the field, this high-density phase does not redisperse and mix homogeneously with the rest of the liquid. Instead, at a certain field strength, the entire high-density phase detaches from the interface and ‘drops’ to the bottom of the glass cell. This ‘delayed’ return to the initial situation with little or no magnetite nanoparticles near the interface is also observed in fig. 5.7. The real part shows a transition at considerably lower fields as during the first scan, while the minimum in the imaginary component is at much lower flux densities.

In a second step-wise scan to 100mT without mixing the ferrofluid, visual inspection of the cell reveals that magnetite nanoparticles are again accumulated at the interface (as in the first scan), but at a certain value of the field, the high-density phase at the bottom of the cell is ‘pulled’ up and results in the relatively fast optical response as compared to the first scan. The second return scan to zero field shows very similar behavior as the first return scan, with the ‘drop’ of the high-density phase being even more pronounced than before.

5.3.4 Discussion

As described in the previous section, only very moderate magnetic field strengths and corresponding field gradients give rise to very distinct, reproducible changes in the optical response of the interface between the glass cell and the ferrofluid where magnetite nanoparticles are magnetophoretically accumulated. However, the spectral changes due to the applied magnetic fields have not yet been related to actual particle concentrations at the interface. Visual inspection (see fig. 5.2) confirms that indeed a higher density of particles is present at the interface as evidenced by the considerably darker phase, indicating a stronger optical absorbance.

In our effort to model the optical response, we encountered similar prob-

lems as described in chapter 3, where the magneto-optical properties of identical ferrofluids were investigated. The relatively simple experimental configuration allows straightforward calculation of the optical response if the dielectric functions of all constituents of our optical system are known. As argued in chapter 3, the optical properties of the magnetite nanoparticles in our ferrofluid can not be described by the bulk dielectric function, most likely due to the nanoscale dimensions of the particles. Moreover, the optical properties presumably also depend on the actual size of the particles; the size-distribution will therefore give rise to even more complex behavior.

Despite the fact that we have not been able to determine accurate energy-dependent optical characteristics of the magnetite nanoparticles, a qualitative comparison of the results in the previous section can be made. It is not straightforward to compare the measurements in figs. 5.5 and 5.6, since upon applying a higher magnetic field all processes proceed considerably faster. To circumvent the interference of the time-contribution, we replotted the data, such as those in fig. 5.6, in a plot of $\text{Im}(Y)$ as a function of $\text{Re}(Y)$. The results are shown in fig. 5.8. In all cases, the data follow a similar curved trajectory. For the low photon energies (1.2eV and 1.5eV), the measurements obtained using three different magnetic field strengths seem to trace the same trajectory, while for higher photon energies (2.0eV and 2.5eV) the trajectories for the highest field are slightly lower.

The magnetic flux densities at the position of the glass/liquid interface are relatively low and correspond to the range where anomalous magneto-optical behavior was observed (see fig. 3.6) in terms of the ratio $\delta n/\delta k$ of birefringence and dichroism. In chapter 3, these results were discussed in relation to the size distribution of the magnetite suspensions. At high fields, all particles (small and large) are assumed to contribute to the response of the system. However, as the field strength becomes smaller, the larger particles are still responsive to the magnetic field, while the smaller particles are not affected. With decreasing size, the volume magnetization declines while Brownian motion becomes more important. A similar situation probably occurs in this case. With the lowest field strength of 50mT only the larger particles are magnetized, while the smaller particles are not. Consequently, only these larger particles migrate under the influence of the magnetic field. For the higher field strength of 100mT, a larger fraction of the size distribution is magnetized and accumulated at the solid/liquid interface under the influence of the magnetic field gradient. The results in fig. 5.5 are in agreement with this, since the higher fields give rise to large optical changes, even at long time-scales.

The experimental results of fig. 5.7 can be represented in a similar way.

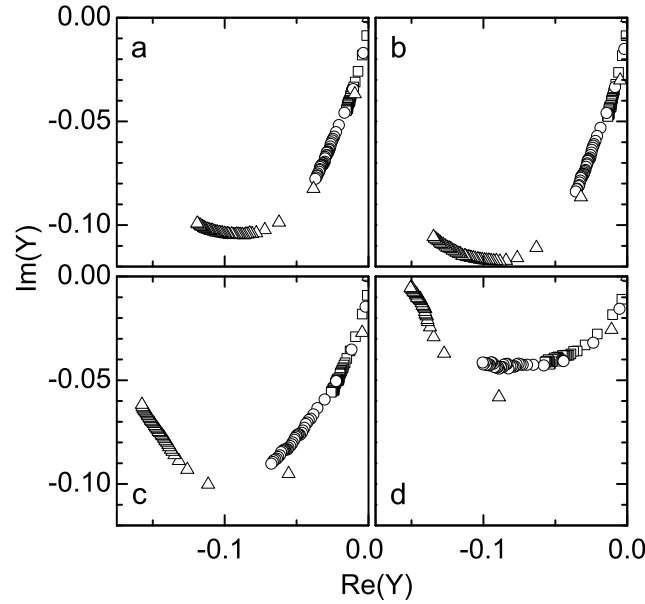


Figure 5.8: Plots of the relation between the imaginary and real parts of the normalized change Y for different times and magnetic fields (for details and explanation of symbols, see fig. 5.6) at photon energies of 1.2eV (a), 1.5eV (b), 2.0eV (c) and 2.5eV (d).

The resulting $\text{Re}(Y)$ - $\text{Im}(Y)$ plots are shown in fig. 5.9. Again, curved trajectories are observed. Comparison of figs. 5.8 and 5.9 reveals that the data-points in the latter figure follow longer trajectories, i.e. the processes are further advanced, or in other words closer to saturation. Also the relative $\text{Im}(Y)$ and $\text{Re}(Y)$ values in the trajectories at different photon energies are comparable.

The agreement between the two different experiments is most obvious when the second scan from 10 – 100mT and back is considered. The data points in the first scan follow trajectories with less negative $\text{Im}(Y)$ values. A similar argument as before can be used to account for this observation. The lowest field, applied during the experiments in figs. 5.5 and 5.6, amounts to 50mT. However, the initial fields used in the step-wise scans is significantly lower, as incremental steps of 2mT are used. Therefore, in the first stages of the experiment, only the largest particles in the size distribution are considered. Once the maximum field strength of 100mT is applied, the same range of particles is magnetophoretically driven toward the surface.

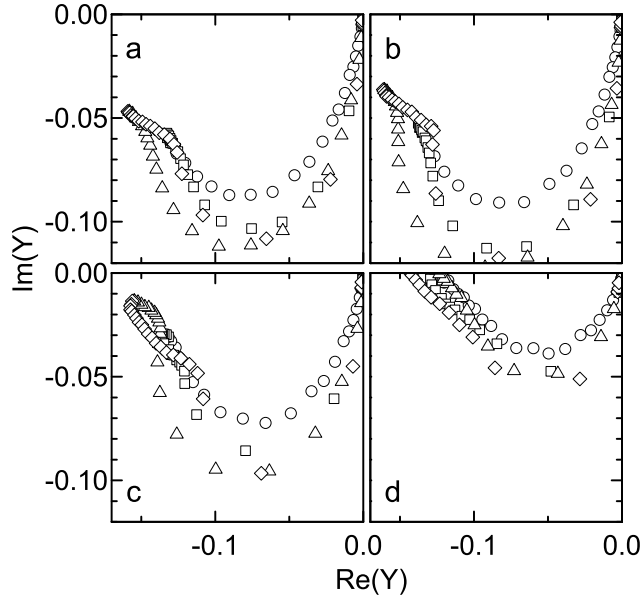


Figure 5.9: Plots of the relation between the imaginary and real parts of the normalized change Y for different magnetic fields (for details and explanation of symbols, see fig. 5.7) at photon energies of 1.2eV (a), 1.5eV (b), 2.0eV (c) and 2.5eV (d).

Consequently, the trajectory described by the data of the return scan have markedly lower $\text{Im}(Y)$ values. In subsequent scans, the entire high-density phase, which contains both large and small particles, is re-accumulated at the surface, as described in the previous section.

Although the spectral changes upon applying a magnetic field could not be modeled adequately, we nevertheless attempted to calculate the $\text{Re}(Y)$ - $\text{Im}(Y)$ trajectories using the bulk dielectric function of Fe_3O_4 as given by Schlegel et al. [24] (shown in fig. 3.9). The experimentally obtained reflection at the interface was calculated with eqs. 5.5-5.10 using the known dielectric functions for BK7 glass and cyclohexane. To represent the optical properties of the ferrofluid, the Bruggeman effective medium approximation was used in combination with the bulk magnetite dielectric function. Using the fill fraction of our ferrofluid ($\Phi = 1.6 \times 10^{-3}$) the reference spectrum ρ_0 was obtained, while difference spectra for larger fill fractions yield the data points shown in fig. 5.10. Despite the poor quantitative agreement of the calculated spectral features with experimental results, similar curved trajectories are

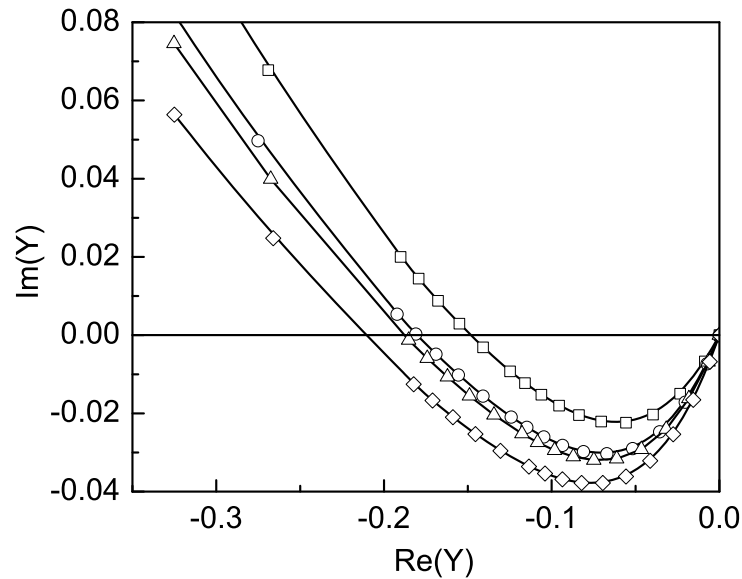


Figure 5.10: Calculated relation (for details see the text) between the imaginary and real parts of the normalized change Y for different fill fractions, at photon energies of 1.5eV (squares), 2.0eV (circles), 2.5eV (triangles) and 3eV (diamonds). The data points represent fill fractions in the range from 0 (origin of the graph) to 0.3, with 0.005-increments in the range 0-0.05, 0.01-increments in the range 0.05-0.1 and 0.1-increments in the 0.1-0.3 range.

observed. However, where the experiments exhibit the lowest $-\text{Im}(Y)$ values at the lowest energies, the opposite is true for the calculations. Again, this demonstrates the inadequacy of using the bulk Fe_3O_4 dielectric function for a proper description of the optical response.

The trajectory in fig. 5.9 at a photon energy of 2.0eV ends nearly at $\text{Im}(Y) = 0$. Comparison to the calculated trajectory in fig. 5.10 and neglecting the absolute differences in magnitude of $\text{Im}(Y)$, indicates this to correspond to a saturation fill fraction of approximately 9%. For randomly close-packed spheres in three-dimensions, the packing density amounts to 64%. Considering that our magnetite particles consist of a core with a diameter of 7nm with a 2.5nm thick shell consisting of oleic acid, the fraction of Fe_3O_4 is estimated to be approximately 20%. Considering the rough estimation made here, and the virtually unknown dielectric function of the magnetite nanoparticles, this is a reasonable agreement.

Finally, we turn to the time-dependence of the spectra in fig. 5.5, most clearly depicted in fig. 5.6. The time-scale of the initial fast regime is approximately 20min. In chapter 4 it has been shown that in a field gradient of 10mT/mm, taking into account the drag force, the speed of a magnetite particle (with 10nm diameter) is approximately 3×10^{-8} m/s. The aforementioned time-scale of 20min would imply a length scale of approximately 35 μ m. Apparently, within the first regime a region of this thickness contributes to the initial optical response. In the second, considerably slower regime migration, reorganization and reorientation of the nanoparticles in the vicinity of the glass/liquid interface gives rise to a steady increase of the optical response with time.

The region of high density at the glass/liquid interface is macroscopic, since it can be observed by the naked eye (see fig. 5.2). However, the reorganization at the interface, assumed to give rise to the gradual optical changes in the aforementioned second regime, may well lead to an organized layer near the interface. Such an ordered layer of magnetite nanoparticles in an Fe₃O₄ ferrofluid has indeed been observed experimentally using in situ neutron reflectometry experiments [11]. Vorobiev et al. reported ordered layers consisting of up to 30 nanoparticle layers. In our case this would correspond to layers of approximately 200 – 300nm. In fact, the spectra in fig. 5.5 show minima and maxima, which may arise from interference of light reflected at two interfaces of a thin layer with a thickness of the same order of magnitude as the wavelength of the light. In agreement with this assumption, longer deposition times in fig. 5.5 and higher magnetic flux densities, presumably corresponding to (optically) thicker, more ordered layers, give rise to a shift of the minima and maxima to lower energies. Also, these presumably interference-related spectral features are most pronounced at lower energies. This again is in agreement with the higher transmission of the magnetite suspension at longer wavelengths as shown in fig. 3.3.

5.4 Conclusions

In this chapter we investigate effects related to inhomogeneous magnetic flux density distributions in oil-based magnetite ferrofluids. In the first section, a thin glass cell placed in a nearly homogeneous magnetic field gives rise to a lower magnetite nanoparticle concentration, as evidenced by a slightly higher optical transmission, in regions where the flux density is slightly smaller. Upon removal of the applied magnetic field, the low-density region in the bottom of the glass cell begins to rise as a result of buoyancy. The

corresponding time scale is of the order of minutes, allowing simple optical monitoring of the ascending ‘bubble’. The kinetics are analyzed in terms of a very simple model taking into account buoyancy of the ‘bubble’ and the drag due to its velocity in the surrounding ferrofluid. Despite the simplicity of the model, it provides an adequate quantitative description of the experimental observations.

In the second part of this chapter, we describe an experimental study of magnetophoretically deposited magnetite nanoparticles at a glass/liquid interface, using a total internal reflection configuration. After a description of the set-up, it is shown that despite the relatively low magnetic flux densities and correspondingly small field gradients, nanoparticles are indeed reversibly accumulated at the solid/liquid interface. Similar changes in the optical response are observed when the magnetic field is either increased at once or step-wise to its maximum value. Since we do not know the effective dielectric function of the magnetite nanoparticles, it is not possible to quantitatively model our experimentally obtained spectra. However, qualitative analysis is achieved by considering the relatively broad size distribution of the particles. For low fields only the largest particles are affected by the field gradient, while for higher magnetic fields, also smaller particles start to contribute to the optical response. Finally, maxima and minima in the spectra are discussed in terms of an ordered magnetite layer at the interface, similar to what has been described in literature. The shift of the spectral features with longer deposition times and higher magnetic fields are in qualitative agreement with this assumption.

References

- [1] M. Giersig and M. Hilgendorff, *J. Phys. D: Appl. Phys.* **32**, L111 (1999).
- [2] M. Giersig and M. Hilgendorff, *Colloid. Surface. A* **202**, 207 (2002).
- [3] M. Hilgendorff, B. Tesche, and M. Giersig, *Austr. J. Chem.* **54**, 497 (2001).
- [4] M. Giersig and M. Hilgendorff, *Eur. J. Inorg. Chem.* **18**, 3571 (2005).
- [5] A. T. Ngo and M. P. Pileni, *Adv. Mater.* **12**, 276 (2000).
- [6] M. Spasova, U. Wiedwald, M. Farle, T. Radetic, U. Dahmen, M. Hilgendorff, and M. Giersig, *J. Magn. Mater.* **272–276**, 1508 (2004).
- [7] A. T. Ngo, J. Richardi, and M. P. Pileni, *Langmuir* **21**, 10234 (2005).
- [8] M. P. Pileni and A. T. Ngo, *Chem. Phys. Chem.* **6**, 1027 (2005).
- [9] Y. Lalatonne, J. Richardi, and M. P. Pileni, *Nat. Mater.* **3**, 121 (2004).

- [10] H. E. Horng, C. Y. Hong, S. Y. Yang, and H. C. Yang, *J. Phys. Chem. Sol.* **62**, 1749 (2001).
- [11] A. Vorobiev, J. Major, H. Dosch, G. Gordeev, and D. Orlova, *Phys. Rev. Lett.* **93**, 267203 (2004).
- [12] M. A. Correa-Duarte, M. Grzelczak, V. Salgueiriño-Maceira, M. Giersig, L. M. Liz-Márzan, M. Farle, K. Sieradzki, and R. Diaz, *J. Phys. Chem. B* **109**, 19060 (2005).
- [13] J. L. Katz, Y. Xing, and R. C. Cammarata, *J. Mater. Res.* **14**, 4457 (1999).
- [14] J. E. Wegrowe, T. Wade, X. Hoffer, L. Gravier, J. M. Bonard, and J. P. Ansermet, *Phys. Rev. B* **67**, 104418 (2003).
- [15] H. Wang, Y. Zhu, C. Boyd, W. Luo, A. Cebers, and R. E. Rosenschweig, *Phys. Rev. Lett.* **72**, 1929 (1994).
- [16] Y. A. Buyevich and A. O. Ivanov, *Physica A* **190**, 276 (1992).
- [17] C. Y. Hong, I. J. Jang, H. E. Horng, C. J. Hsu, Y. D. Yao, and H. C. Yang, *J. Appl. Phys.* **81**, 4275 (1997).
- [18] A. O. Ivanov and A. Y. Zubarev, *J. Magn. Magn. Mater.* **201**, 222 (1999).
- [19] R. J. Hunter, *Foundations of colloid science*, Oxford University Press, New York, 2001.
- [20] C. S. Lee, H. Lee, and R. M. Westervelt, *Appl. Phys. Lett.* **79**, 3308 (2001).
- [21] H. Wormeester, E. S. Kooij, A. A. Mewe, S. Rekveld, and B. Poelsema, *Thin Solid Films* **455-456**, 323 (2004).
- [22] R. M. A. Azzam and N. H. Bashara, *Ellipsometry and polarized light*, North Holland, Amsterdam, 1987.
- [23] J. Rheims, J. Köser, and T. Wriedt, *Meas. Sci. Technol.* **8**, 601 (1997).
- [24] A. Schlegel, S. F. Alvarado, and P. Wachter, *J. Phys. C: Solid State Phys.* **12**, 1157 (1979).

Summary

In this thesis we describe a comprehensive study of anisotropic nanoscaled media, primarily using spectroscopic ellipsometry. Two distinct systems are investigated in this work. Porous anodic aluminium oxide, often used as a versatile template for manufacture of anisotropic nanostructures, but also for filtration purposes, is characterized by ellipsometry in combination with a number of other relevant techniques. In the second part of the thesis, we focus on magnetite ferrofluids in the presence of external magnetic fields. The content of this work is presented in five chapters.

In chapter 1 an overview is given of the fundamental aspects in nanocolloid science. The interactions, which play a role in nanocolloidal suspensions, and the stabilization of the nanoparticles in solution are described. The relative strengths of the governing interactions are considered in relation to the parameters characterizing the experimental system. Methods for obtaining thin colloidal films and the influence of external fields during nanoparticle deposition from solution are reviewed. The main focus in this chapter is on ferrofluids and the self-assembly of nanoscale systems.

Chapter 2 presents a detailed investigation of porous aluminium oxide formed through anodization of thin film aluminium samples. Spectroscopic ellipsometry and electron microscopy experiments are used to characterize porous aluminium oxide obtained by anodization of thin aluminium films. Rutherford backscattering and x-ray diffraction experiments provide information on the composition and the structure of the samples. Anodization of aluminium on thin film samples with a well-defined geometry is reproducible. Electron microscopy clearly shows the formation of randomly distributed, but almost perfectly aligned cylindrical pores with their long axis perpendicular to the film/substrate interface. Additionally, comparison of x-ray diffraction spectra obtained before and after anodization show a nearly complete transformation of aluminium to aluminium oxide. Ellipsometry spectra are analyzed using a newly developed anisotropic optical model, partly based on the original work by Bruggeman. We show that the model

adequately describes the optical response of the anodized film in terms of three physically relevant parameters: the film thickness, the cylinder fraction and the nanoporosity of the aluminium oxide matrix. Values of the first two quantities are in perfect agreement with electron microscopy images. The validity of our optical model is verified by widening of the pores through chemical etching in phosphoric acid. The increase of the cylinder fraction with increasing etching time and etchant concentration, as determined from ellipsometry spectra, is again in perfect agreement with electron microscopy images. The results enable easy determination of the order and rate constant of the etching reaction. In contrast to the cylinder fraction, the nanoporosity of the aluminium oxide remains unchanged, presumably due to the inaccessibility of the small defect-like voids in the amorphous oxide to the etch solution.

In chapter 3 the versatility of spectroscopic ellipsometry in transmission mode to study magneto-optical properties of magnetite ferrofluids is explored. Linear birefringence and linear dichroism are both obtained simultaneously from experimental ellipsometry spectra as a function of applied magnetic field. We derive simple equations, which relate the experimentally obtained optical quantities to the magneto-optical properties. The simultaneous measurement of birefringence and dichroism with high accuracy enables comparison of our data to previous experimental and theoretical work on the magneto-optical characteristics of ferrofluids. The spectral characteristics of the birefringence and dichroism are in line with previous experimental work. However, marked differences are observed, which may be related to size distribution of the particles, the solvent in which they are suspended, the degree of oxidation of the magnetite particles and the effective dielectric function of the nanoparticles constituting the ferrofluids. Most pronounced is the large ratio of birefringence and dichroism in our results as compared to previous work. The magnetic field-dependent optical response is in qualitative agreement both with previous experimental work and also with theoretical models. The quantitative discrepancies are discussed in relation to a modified dielectric function of the magnetite nanoparticles in the ferrofluids.

The suitability of various (electro-)magnet configurations for magneto-phoretic deposition is studied in chapter 4. Using finite element methods, the spatial distribution of the magnetic flux density in the air gap (for 2 pole-configuration) and in the vicinity of one of the poles (for single magnets) is calculated. Finite element calculations have the advantage that essentially any configuration can be investigated accurately and relatively fast. It is shown that, using relatively low currents and moderate voltages, con-

siderable magnetic field gradients can be obtained. The main focus of this chapter is to understand and control the magnetic flux density in the desired space, i.e. the sample volume, only by varying the applied current. Modification of the pole shoes to yield an asymmetric geometry has a significant effect on the field distribution and also on the magnitude of the generated gradients. We show that the tunable magnetic field gradients are sufficiently strong to effectively compete with Brownian motion and in principle enable magnetophoretic deposition of nanocolloidal magnetic particles.

In the final chapter 5, the influence of external magnetic fields on the redistribution of magnetite (Fe_3O_4) nanoparticles in an oil-based ferrofluid is investigated experimentally. In the first part of the chapter, the presence of a very moderate magnetic field gradient is shown to give rise to a separation of the ferrofluid in low- and high-density phases, as evidenced by slight differences in optical transmission. Upon removing the applied magnetic field, the low-density region in the bottom of the cell begins to rise as a result of buoyancy. The corresponding time scale is of the order of minutes, allowing simple optical monitoring of the ascending ‘bubble’. The kinetics are analyzed in terms of a very simple model taking into account buoyancy of the ‘bubble’ and the drag due to its velocity in the surrounding ferrofluid. Despite the simplicity of the model, it provides an adequate quantitative description of the experimental observations.

In the second part of chapter 5, we describe an experimental in situ study of magnetophoretically deposited magnetite nanoparticles, using spectroscopic ellipsometry in a total internal reflection configuration. After a description of the set-up, we show that despite the relatively low magnetic flux densities and correspondingly small field gradients, nanoparticles are reversibly accumulated at an interface. Since we do not know the effective dielectric function of the magnetite nanoparticles, it is not possible to quantitatively model the experimentally obtained ellipsometry spectra. However, in a qualitative analysis the relatively broad size distribution of the particles is considered. For low fields only the largest particles are affected by the field gradient, while for higher magnetic fields also smaller particles start to contribute to the optical response. Finally, oscillatory spectral features, which shift with longer deposition times and higher magnetic fields, are discussed in terms of an ordered magnetite layer at the interface, similar to what has been described in literature.

Samenvatting

In dit proefschrift beschrijven we een uitgebreide studie van anisotrope nanogestructureerde media. Hierbij wordt hoofdzakelijk gebruik gemaakt van spectroscopische ellipsometrie. Twee verschillende systemen worden onderzocht in het werk beschreven in dit proefschrift. Poreus aluminiumoxide, gevormd door middel van anodisch oxideren, wordt vaak gebruikt als veelzijdig sjabloon om anisotrope nanostructuren en nanodeeltjes te groeien. Ook wordt het nanoporeuze materiaal gebruikt als filtratiemembraan. De poreuze aluminiumoxide lagen worden bestudeerd met behulp van ellipsometrie, in combinatie met een aantal verschillende relevante karakterisatie technieken. In het tweede deel van het proefschrift richten we de aandacht op het gedrag van magnetische vloeistoffen, bestaande uit gesuspendeerde magnetiet nanodeeltjes, in de aanwezigheid van externe magneetvelden. De bevindingen voortkomend uit dit werk worden beschreven in vijf hoofdstukken.

In hoofdstuk 1 wordt een overzicht gegeven van de fundamentele aspecten die een rol spelen in nanocolloïdale suspensies. De interacties tussen nanodeeltjes in vloeistoffen, en de daarmee nauw samenhangende stabiliteit van de nanocolloïdale suspensie, worden beschreven. De relatieve sterktes van de belangrijkste interacties worden beschouwd in relatie tot de parameters, die ons experimentele systeem karakteriseren. Tevens wordt een overzicht gegeven van verschillende manieren om dunne lagen van nanodeeltjes vanuit oplossing te groeien, al dan niet in de aanwezigheid van externe velden. Hierbij gaat de aandacht in dit hoofdstuk vooral uit naar magnetische vloeistoffen en de self-assembly van systemen op nanometer schaal.

Hoofdstuk 2 beschrijft een uitgebreid onderzoek naar de eigenschappen van anodisch aluminiumoxide dat wordt verkregen door anodiseren van dunne laagjes aluminium. Karakterisatie van de dunne geanodiseerde poreuze aluminiumoxide lagen wordt gedaan met behulp van spectroscopische ellipsometrie en elektronenmicroscopie. Rutherford backscattering and Röntgen diffractie experimenten geven informatie over de samenstelling en

de kristallografische structuur van de lagen. Tevens is gebleken dat de anodisatie van dunne films van aluminium lagen met een goed gedefinieerde geometrie reproduceerbaar is. Elektronenmicroscopie resultaten laten zien dat willekeurig verdeelde, maar nagenoeg parallelle cilindrische poriën worden gevormd waarvan de lange assen loodrecht staan op het grensvlak tussen de film en het substraat. Uit Röntgen diffractie spectra, gemeten zowel voor als na anodisatie, blijkt dat de gehele aluminium lagen nagenoeg volledig geoxideerd zijn tot aluminiumoxide. Om de ellipsometrie spectra te analyseren is er een nieuw model ontwikkeld, deels gebaseerd op het originele werk van Bruggeman. We laten zien dat het model de optische response van de geanodiseerde films goed beschrijft in termen van fysisch relevante parameters, waaronder de film dikte, de fractie cilindervormige poriën in de laag en de nanoporositeit van het aluminiumoxide. Ellipsometrisch bepaalde waarden voor de eerste twee grootheden komen uitstekend overeen met hetgeen waargenomen is met behulp van elektronenmicroscopie. Chemisch etsen in fosforzuur leidt tot vergroting van de cilindervormige poriën, hetgeen ons in staat stelt de geldigheid van het model te verifiëren. De toegenomen fractie van cilindrische poriën met langere etstijden en hogere concentraties, zoals bepaald uit ellipsometrie experimenten, is wederom in uitstekende overeenstemming met elektronenmicroscopie afbeeldingen. Op basis van deze resultaten kan de orde en snelheid van de etsreactie eenvoudig worden afgeleid. In tegenstelling tot de volume fractie van de grote cilindervormige poriën, blijft de nanoporositeit van het aluminium oxide constant tijdens het etsen. Waarschijnlijk is dit gerelateerd aan het feit dat de etsvloeistof niet tot in de hele kleine poriën van het amorfe oxide kan doordringen.

In hoofdstuk 3 wordt met behulp van spectroscopische ellipsometrie in transmissie mode gekeken naar de magneto-optische eigenschappen van magnetische vloeistoffen op basis van magnetiet. Zowel lineaire dubbelbreking als lineair dichroïsme worden als functie van het aangelegde magnetische veld gelijktijdig bepaald uit de gemeten ellipsometrie spectra. Eenvoudige uitdrukking worden afgeleid die de gemeten optische grootheden relateren aan de magneto-optische eigenschappen van de magnetische vloeistoffen. De nauwkeurige bepaling van zowel dubbelbreking als dichroïsme stellen ons in staat om de verkregen data te vergelijken met eerdere metingen door anderen en ook met theoretisch werk aan de magneto-optische eigenschappen van magnetische vloeistoffen. Hoewel de trend in de spectrale karakteristieken lijken op datgene wat eerder is gepubliceerd, zijn er ook duidelijke verschillen die mogelijk gerelateerd zijn aan de verdeling van de deeltjesgroottes, het oplosmiddel waarin de deeltjes zijn gesuspendeerd, de oxidatietoestand van de magnetiet deeltjes en de effectieve diëlectrische functie van de nanodeelt-

jes waaruit de magnetische vloeistoffen bestaan. Het meest uitgesproken in de resultaten is de grote verhouding tussen dubbelbreking en dichroïsme in onze resultaten in vergelijking met eerder werk. De optische respons in relatie tot het aangelegde magnetische veld is in kwalitatieve overeenkomst met eerder beschreven experimenteel werk en theoretische modellen. De kwantitatieve verschillen worden besproken in relatie tot de gewijzigde diëlectrische functie van de gesuspendeerde magnetische nanodeeltjes.

De toepasbaarheid van verschillende (elektro-)magneet configuraties om magnetoforetische depositie van nanodeeltjes vanuit oplossing de bewerkstellingen, wordt bestudeerd in hoofdstuk 4. Met behulp van eindige elementen methodes wordt de ruimtelijke verdeling van de magnetisch fluxdichtheid berekend in de ruimte tussen twee magneetpolen of in de nabijheid van een enkele magneet. Berekeningen met behulp van eindige elementen methodes hebben het voordeel dat nagenoeg iedere configuratie nauwkeurig en relatief snel kan worden geëvalueerd. We laten zien dat met relatief lage stromen en beperkte spanningen, aanzienlijke magneetveld gradiënten kunnen worden verkregen. De nadruk in dit hoofdstuk ligt op het begrijpen en controleren van de magnetische flux dichtheid in de beschikbare ruimte, dat wil zeggen in het volume van onze cel, door alleen de stroom door de elektromagneet te variëren. Verandering van de vorm van de magneetpolen, waardoor een asymmetrische geometrie wordt verkregen, heeft een significant effect op de verdeling van het veld en ook op de grootte van de magnetische gradiënt. Door middel van een afschatting laten we zien dat de instelbare gradiënten van het magnetische veld groot genoeg zijn om de Brownse beweging van de deeltjes in de vloeistof te overwinnen. Daarmee is magnetoforetische depositie van nanocolloïdale deeltjes in principe mogelijk.

In het laatste hoofdstuk 5 wordt het effect van extern aangelegde magneetvelden op de herverdeling van magnetiet nanodeeltjes in een magnetische vloeistof experimenteel bestudeerd. In het eerste deel van dit hoofdstuk laten we zien dat een zeer beperkte gradiënt in het magnetische veld aanleiding geeft tot een scheiding van de vloeistof in twee fases met een hogere, respectievelijk lagere deeltjesdichtheid. Deze fasescheiding blijkt uit een gering verschil in optische transmissie van de vloeistof. Wanneer het magneetveld wordt opgeheven begint het gebied met lage concentratie nanodeeltjes te stijgen in de vloeistof met een hogere deeltjesdichtheid. Door het geringe dichtheidsverschil en dus kleine opwaartse kracht, is de tijdschaal waarop dit plaatsvindt in de orde van minuten. Hierdoor is het goed mogelijk is om met conventionele optische methodes de stijgende ‘bel’ te volgen. De resultaten worden geanalyseerd met behulp van een eenvoudig model, waarin de opwaartse kracht van de ‘bel’ met lagere dichtheid en de wrijvingsweerstand

ten gevolge van de snelheid in de omringende vloeistof worden meegerekend. Ondanks de eenvoud van het model geeft het een zeer redelijke beschrijving van de experimenten.

Tot slot beschrijven we in het tweede deel van hoofdstuk 5 in situ experimenten waarin magnetiet nanodeeltjes door middel van magnetoforetische depositie worden verzameld aan een vast/vloeistof grensvlak. Daarbij wordt gebruik gemaakt van spectroscopische ellipsometrie in een totale interne reflectie geometrie. Na een beschrijving van de experimentele opstelling laten we zien dat magnetische nanodeeltjes reversibel kunnen worden verzameld aan een grensvlak ondanks de relatief lage magnetische velden en daarmee samenhangende kleine gradiënten. Kwantitatieve analyse van de experimentele ellipsometrie spectra is helaas niet mogelijk, aangezien de effectieve diëlektrische functie van de magnetiet nanodeeltjes niet bekend is. Desalniettemin proberen we de resultaten in een kwalitatieve discussie te relateren aan de relatief brede verdeling van deeltjesgroottes. Voor lage veldsterktes ‘voelen’ alleen de grootste deeltjes het extern aangelegde veld, terwijl voor hogere magneetvelden ook de kleinere deeltjes bij zullen gaan dragen aan de optische respons van het systeem. Tot slot zullen kenmerken van de gemeten spectra, die een roodverschuiving vertonen voor langere depositietijden en hogere magneetvelden, worden besproken aan de hand van recente data in de literatuur waarin gesuggereerd wordt dat zich een geordende laag magnetietdeeltjes aan het grensvlak vormt.

Acknowledgements

After four years spent in Solid State Physics group at University of Twente it is a great pleasure now for me to look back and to thank all people who helped me to finish my PhD studies with success.

I would like to thank Bene, my supervisor and promotor, from whom I learned the rigorous academic attitude that I needed to fulfill myself as a researcher. His comments and advice on our research project, but also regarding the rest of my educational life, have proven to be real 'gold' words. I am deeply grateful to Bene for providing the opportunity to work in his group and for his support during my PhD work.

My special thanks go to Stefan for supervising my PhD work, for his attention and patience guiding my work from the very beginning until writing this manuscript. Without his help and support this work would not be completed in a way it is. Because we shared the same office, our relation was more than a professional one. Stefan was my first target when I needed to find answers quickly and concisely. He helped me to integrate in the Dutch society by explaining, translating and fighting at the telephone with the Dutch authorities.

I am grateful to Hans and Gerard for giving me the opportunity to exercise and to learn Dutch. Their patience and time were very important contributions in my Dutch learning process. I would like to thank them and also Herman and Geert for providing me with instant help whenever I came with one of my many requests concerning technical matters.

Herbert and Harold, thanks for your prompt answers, support and encouragement in reply to my questions and ideas regarding my work.

Many thanks go to Raoul and Robert for their help during the writing of my thesis.

I am also grateful to Rianne, for her prompt help at time-sensitive moments and for general administrative support rendered to me during the time I spent in the group.

Many thanks go to Agnes, Arend, Martijn and Ruben for our very nice

and fruitful time spent in the lab. Also, I would like to thank all other PhD students in the Solid State Physics group, who have been real members of VSF family. My first Christmas away from my family back home spent with Oughuzan, the very pleasant car travels with Marko in the rhythms of Radio Vier, the all-time history discussions with Frank, Nuri and Misha made a colorful social and educational interaction between me and the VSF PhD students.

I can't forget my best friend, Omer. During his stay in Twente we became best friends and after his departure we have kept our friendship intact. Our many discussions helped me to understand myself and my neighborhood much better.

I also gratefully acknowledge my Romanian friends from the Netherlands for their support and help and for making the time I spent here so enjoyable and productive. Together, we were able to create a small Romanian community, which made us feel like home.

I want to say thank you to my parents and grand-parents for their belief in me.

Finally, I would like to thank my wife Simona and my daughter Lisa-Maria, for their love, support, patience and understanding.

Aurelian

May, 2006

Buzau, Romania

Curriculum Vitae

Aurelian Cătălin Gâlcă

Born: November 26th, 1977, Buzău, Romania

September 1992 - June 1996

Baccalaureate diploma

B.P. Hașdeu National College, Buzău, Romania

October 1996 - February 2002

B.Sc. and M.Sc.

Solid State Physics Department

Faculty of Physics, Bucharest University, Romania

September 2000 - December 2001

Computer Science teacher

Horia Hulubei High-school, Bucharest, Romania

December 2001 - December 2005

Junior researcher, Ph.D. student

Solid State Physics group

MESA+ Institute for Nanotechnology

University of Twente, Enschede, The Netherlands

May 2006 - present

researcher

Solid State Magnetism laboratory

National Institute of Materials Physics, Bucharest-Magurele, Romania

